

MASTERARBEIT ZUR ERLANGUNG
DES AKADEMISCHEN GRADES
MASTER OF SCIENCE IN PHYSIK

Development of Laser Sources and Diagnostics for Probing Relativistic Laser-Matter Interaction

Martin Beyer

geboren am 22. Juni 1999
in Weimar

Gutachter:

Prof. Dr. Malte C. Kaluza
Dr. Yasmina Azamoum



Jena, Dezember 2022



FRIEDRICH-SCHILLER-
UNIVERSITÄT
JENA Physikalisch-Astronomische Fakultät

Danksagung

Die vorliegende Masterarbeit wäre ohne die Unterstützung und das Engagement vieler Menschen nicht zustande gekommen. Daher danke ich im Folgenden jenen, die mich während meines Studiums und meiner Masterarbeit unterstützt und motiviert haben.

Zuerst gebührt mein Dank Prof. Malte Kaluza, in dessen Arbeitsgruppe der relativistischen Laserphysik ich meine Masterarbeit bestreiten durfte. Erst durch ihn habe ich dieses Thema für mich entdeckt und er war es, der meine Begeisterung für die Laser-Plasmaphysik geweckt hat.

Furthermore, I express my special thanks to Dr. Yasmina Azamoum for her great supervision of my topic. She took much effort to obtain a detailed understanding of my work in order to improve my thesis to an unprecedented degree. From her I learned a great deal about scientific writing and NOPA-based laser pulse generation.

Als nächstes danke ich Dr. Georg A. Becker für die Betreuung des Experimentes am POLARIS. Durch die vielen spannenden Gespräche im Labor habe ich eine Menge über Plasmaphysik und Shadowgraphy gelernt. Außerdem habe ich seine fortlaufende Unterstützung bei der Sortierung und Auswertung der experimentellen Daten sehr geschätzt.

In diesem Zusammenhang darf Dr. Matthew Schwab keinesfalls fehlen. Durch ihn konnte ich eine Verbesserung des Abbildungsaufbaus erreichen, da er mir bei dessen Design half und zusätzlich den Denkanstoß zur Entwicklung des Coronagraphen gab.

Ein funktionstüchtiger Laser bildet das Herzstück eines jeden Laser-Plasma Experiments. Daher richte ich ein großes Dankeschön an Marco Hellwing für seine unablässige Expertise über Laserverstärker. Auch sein ständiger Ansporn zur Suche nach neuen Ideen inspirierte mich. Daraus folgten die Entwicklung des technischen Designs des Coronagraphen und die Inbetriebnahme der Herriott-Zelle.

Auch Frank Schorcht trägt Anteil an dieser Arbeit. Da der Messaufbau niedrige Drücke erforderte, war nur durch seine schnelle Bereitstellung einer Vakuumkammer und der Hilfe beim folgenden Vakuum-Aufbau die Realisierung meines Setups unter Niedrigdruck möglich.

Zur Interpretation meiner Messdaten habe ich Simulationen von Selbstphasenmodulation bei hohen Intensitäten durchgeführt. Für die Bereitstellung seiner Expertise zum theoretischen Teil meiner Arbeit danke ich hierbei Dr. Marco Hornung.

Natürlich gilt mein Dank auch der gesamten Arbeitsgruppe der relativistischen Laserphysik für dieses ausgezeichnete letzte Jahr. Neben vieler wissenschaftlich interessanter Gespräche, hat mich vor allem die gute Atmosphäre motiviert.

Nicht vergessen darf ich hierbei vor allem meine beiden Freunde und Bürokollegen Mathis Nolte und Till Weickhardt. Beide waren immer für mich da, wenn ich Probleme oder ein Motivationstief hatte. Ohne Till und seine Expertise zu Laserverstärkern hätte ich mein Experiment zur spektralen Verbreiterung mittels Selbstphasenmodulation nicht erfolgreich

durchführen können. Und erst durch die Zusammenarbeit mit Mathis am POLARIS Tröpfchenexperiment konnte ich so viel Wissen über Plasmaphysik und die Erzeugung stabiler Tröpfchen erlangen.

Abschließend möchte ich mich bei allen Personen bedanken, die mich täglich anspornen und unterstützen. Ein besonderer Dank gilt meiner Familie, insbesondere meinen Eltern und meiner Schwester Kristin. Ihre bedingungslose Unterstützung hat mich stets aufs Neue motiviert. Auch danke ich meinen Freunden, die mir täglich im Studium beistehen. Sie haben es geschafft mich stets zu beflügeln. Dabei möchte ich explizit Max Bräuer hervorheben, der sich die Zeit nahm um meine Arbeit Korrektur zu lesen.

Contents

1. Introduction	1
2. Fundamentals	3
2.1. Ultrashort Laser Pulses	3
2.1.1. Temporal description	3
2.1.2. Transversal description	4
2.2. Generation and description of laser-induced plasmas	6
2.2.1. Ionization processes	6
2.2.2. Plasma properties	8
2.2.3. Pulse propagation in plasmas	10
2.3. Laser pulse generation based on nonlinear effects	11
2.3.1. Non-collinear Optical Parametric Amplification (NOPA)	12
2.3.2. Self Phase Modulation (SPM)	15
2.3.3. Pulse steepening	18
2.3.4. Kerr-induced self-focusing	19
3. Probing relativistic laser-plasma interactions with NOPA-based pulses	21
3.1. The NOPA-based laser pulse generation	21
3.1.1. NOPA setup	22
3.1.2. NOPA characterization	23
3.1.3. Spectral control	25
3.2. Experimental setup	26
3.3. Plasma emission suppression - the coronagraph	29
3.3.1. Design and implementation	29
3.3.2. Experimental results	31
3.4. Shadowgraphy of the plasma evolution	33
3.4.1. Plasma expansion velocity estimation	34
3.4.2. Halo structure around the central droplet	39
3.5. Summary and discussion	40
4. SPM-based laser pulse generation	41
4.1. Single-pass SPM-based laser pulses	41
4.1.1. Spectral measurement	43
4.1.2. Compression of laser pulses	47
4.2. Multi-pass SPM-based laser pulses	50
4.2.1. Experimental setup	52
4.2.2. Spectral characterization	53
4.3. Impact of pulse steepening	56
4.3.1. Numerical solution of pulse steepening	56
4.3.2. Influence of the transverse intensity profile - focal averaging	58
4.4. Summary and discussion	60

5. Conclusion	62
References	64
List of abbreviations	70
Appendix	72
A. Derivation of the nonlinear wave equation and phase	72
A.1. Case without dispersion	72
A.2. Case with dispersion	74
B. Theoretical description and numerical methods of pulse steepening	75
B.1. Method of Characteristics	76
B.2. Crank-Nicolson scheme	77
C. Characterization of the chirped pulse amplification (CPA) system	78
C.1. CPA setup	78
C.2. Amplifier characterization	79
D. Alignment of the NOPA setup	82
E. Spectral sensitivity of the spectrometer	84
F. Additional experimental data	86

1. Introduction

Experimental access to the physics of high-energy particles opened up in the last century with the development of particle accelerators. The first prototype of a particle accelerator was built by Cockroft and Walton in 1932 [1]. They used a special circuit to generate a high voltage, which was able to accelerate protons up to a kinetic energy of 710 keV and awarded them the Nobel Prize in 1951. Since then, particle accelerators have permanently entered the experimental repertoire of elementary physics research for the study of atoms and their constituents. With the completion of the Large Hadron Collider (LHC) in 2008, a particle accelerator at the CERN nuclear research center in Geneva, new records have been set in the field of particle acceleration with proton energies of up to 6.5 TeV [2]. On different energy scales, accelerators have many applications in science, technology, industry and medicine, such as material science [3], cancer therapy [4] or fusion research [5]. Here, electrons and ions are accelerated to energies in the range of 10–1000 MeV.

However, the accelerating field strengths in radio-frequency driven accelerator cavities are limited to ≈ 100 MV/m [6]. Therefore, in order to yield higher energy gain the length of accelerators has to increase. This issue was tackled by Tajima and Dawson in 1979, who showed that intense laser pulses can excite a wake of plasma oscillation, in which externally injected electrons were accelerated by high electric fields [7] to relativistic energies. These fields are sustained by a relativistic plasma wave, which is driven by the laser. For a plasma density of $10^{18}/\text{cm}^3$, the supported field strength is 10^{11} V/m, which is a thousand times higher than in conventional accelerators [8]. With the development of chirped pulse amplification (CPA) by Strickland and Mourou in 1985 [9], it was possible to generate ultrashort pulses with very high field strengths in the focus. Since then, the development of plasma-based particle accelerators has shown great promise because the large accelerating fields lead to the possibility of compact acceleration schemes [8].

Such a laser system is the Petawatt Optical Laser Amplifier for Radiation Intensive Experiments (POLARIS) in Jena, which was used for the experiments conducted in this thesis. Here, proton energies of up to 20 MeV have already been generated in previous experiments [10] in 2019. The objective of this work is the further development and the experimental use of a setup for the investigation of the laser-generated plasma with an optical probing system. The development of tools to diagnose the generated plasma from a relativistic laser-matter interaction is important to deepen the understanding of the particle acceleration process. Depending on the plasma properties of interest, different means of plasma probing might be suggested such as probes using charged particle pulses to access the sheath structure and the electric and magnetic fields of a plasma [11] or X-ray Thomson scattering to measure directly the electron temperature T_e and deduce the electron density n_e [12]. In this thesis, however, the probing is carried out with an optical laser pulse. Here, optical probing offers the possibility to directly image the evolution of the plasma's density distribution to retrieve the expansion velocity or image the plasma wave in a laser wakefield accelerator. The most commonly applied techniques are shadowgraphy [13], polarimetry [14] and interferometry [15,

Chap. 4]. In previous experiments at POLARIS, a temporally stretched broadband optical probe laser pulse generated by a μJ non-collinear optical parametric amplifier (NOPA) was used to determine the spatio-temporal evolution of the plasma in a single laser shot by using a 1D-spatially resolving spectrometer [16]. In this work, water micro-droplets are used as a target with an off-harmonic optical probe to obtain shadowgraphy images. Off-harmonic means that the central wavelength of the probe pulse does not coincide with the fundamental or second harmonic (SH) wavelength of the main laser, which is important to suppress plasma self-emission effects at these wavelengths with suitable filters. In contrast to foils, where the plasma expansion cannot easily be imaged via shadowgraphy, the imaging of the expansion of the plasma generated in the water micro-droplets is easily achievable. Furthermore, foils have to be replaced by a fresh target after each shot [17], whereas microdroplets are a cost-effective alternative and can be used with high repetition rates. Experiments with water droplets were conducted previously at the Jenaer Titan:Saphir (JETI) laser system with maximum proton energies of 3 MeV [18].

In this work, we have set up a pump-probe experiment consisting of water droplets and imaging and ion detection diagnostics. The NOPA-based probe pulse was used to investigate the temporal evolution of the plasma expansion on picosecond time scales. An introduction to the fundamentals of ultrashort pulses, the generation and properties of laser induced plasmas and the physics of nonlinear effects used for the probe pulse generation is given in chapter 2. For the purpose of the pump-probe experiment at POLARIS, we recommissioned and characterized the NOPA probing system (developed in [19, 20]). This is detailed in chapter 3. In order to improve the visualization of the droplets, we introduced and successfully applied a new technique (using a so-called *coronagraph*) to suppress the strong, unpolarized plasma emission. Then, we recorded a series of shadowgraphy images that probed the plasma expansion process until full transparency of the central plasma was reached. The data was analyzed and the plasma expansion velocity was estimated.

The second part of the thesis deals with the search for an alternative laser pulse generation scheme using self phase modulation (SPM) as the nonlinear process to produce off-harmonic pulses suitable for probing. This is presented in chapter 4. Here, we used thin plastics for SPM-induced broadening of a CPA-amplified, milli Joule-level laser pulse. First, we developed a simple setup, focusing the laser pulse on the plastic in a single pass. As a second approach, we investigated a design based on a multi-pass Herriott cell. Due to the high intensities required ($I \approx 10\text{TW}/\text{cm}^2$), we performed simulations based on the theory of pulse steepening to reproduce the experimentally observed spectra. This can be used to qualitatively predict the spectral properties of SPM-induced pulse broadening at high intensities.

2. Fundamentals

For the experimental investigation of the physical properties of laser-induced plasmas, a suitable probing technique is required. In order to design and realize a probing system, the properties of the generated plasmas must be assessed first. At the POLARIS laser system, plasmas are generated in (solid or liquid) target materials during the laser-matter interaction with high intensity, ultrashort laser pulses. The probe needs to be designed in such a way that the properties of the laser-matter interaction forming the plasma can be accessed. For this purpose, the probe is designed to be an ultrashort pulse with specific requirements for energy, spectrum and pulse duration. Therefore, the temporal and spatial structure of ultrashort laser pulses is introduced in section 2.1. Furthermore, the generation and optical properties of plasmas are detailed in section 2.2. The latter is necessary to describe the propagation of a laser pulse in a plasma. The generation of a probe pulse is achieved using nonlinear processes, which play a crucial role in the generation of new frequencies outside the bandwidth of the original pulse. For this purpose, the fundamentals of second-order and third-order nonlinear processes are introduced in section 2.3.

2.1. Ultrashort Laser Pulses

The description of ultrashort pulses is the basis of understanding the light-matter interaction forming the plasma as well as assessing the required properties of the ultrashort optical pulses. In the regime of femtosecond pulses, the temporal shape of the pulse is fundamentally connected to its spectral content, which is crucial for the application of probe pulses. Furthermore the transversal distribution of intensity of the pulse is important to describe diffraction and spatial nonlinear effects that will be discussed later.

2.1.1. Temporal description

A laser pulse in vacuum is described by an electric field of finite duration that is formed by a coherent superposition of monochromatic plane waves¹ with carrier frequencies ω and wave vectors \mathbf{k} [21]

$$\mathbf{E}(\mathbf{r}, t) = \int_{\mathbb{R}^3} \int_{-\infty}^{\infty} \mathbf{E}_0(\mathbf{k}, \omega) e^{i(\mathbf{k} \cdot \mathbf{r} - \omega t)} d\omega d^3 k. \quad (2.1)$$

In a simplified model of a one-dimensional pulse propagating with the speed of light in z -direction and a central angular frequency $\omega_0 = \frac{2\pi c}{\lambda_0}$, equation (2.1) can be modified to

$$\mathbf{E}(z, t) = \frac{1}{2} \mathbf{E}_0(t) e^{i(k_0 z - \omega_0 t)} + \text{c.c.} \quad (2.2)$$

¹This is valid for the description of a 1D-laser pulse neglecting transversal effects which are discussed in section 2.1.2.

The temporal profile (time t) of the envelope function $E_0(t)$ is commonly modeled as a Gaussian shaped profile with the pulse duration τ given at full width at half maximum (FWHM)

$$E_0(t) = \mathcal{E}_0 e^{-4\ln 2 \left(\frac{t}{\tau}\right)^2}. \quad (2.3)$$

Here, \mathcal{E}_0 is the vector-valued amplitude of the electric field. The distribution of the field in the frequency domain can be calculated via a Fourier Transform of $E_0(t)$

$$\tilde{E}_0(\omega) = \frac{1}{\sqrt{2\pi}} \int_{-\infty}^{\infty} E_0(t) e^{-i\omega t} dt = \mathcal{E}_0 \frac{\tau}{2\sqrt{\ln 2}} e^{-4\ln 2 \left(\frac{\omega}{\Delta\omega}\right)^2}. \quad (2.4)$$

with the FWHM spectral bandwidth $\Delta\omega = 4\ln 2/\tau$, which is equivalent to the time-bandwidth product $\Delta\nu \cdot \tau = 0.441$ of a Fourier transform-limited (FT) Gaussian pulse [22, p. 943]. Then using $\lambda_0 = c/\nu$, the pulse duration and the spectral bandwidth $\Delta\lambda$ are inversely related via

$$\Delta\tau = \frac{0.441}{c} \frac{\lambda^2}{\Delta\lambda} = 1468 \text{ fs} \frac{\lambda^2 [\mu\text{m}^2]}{\Delta\lambda [\text{nm}]}. \quad (2.5)$$

2.1.2. Transversal description

To describe diffraction effects on a laser pulse, the one-dimensional model must be extended by a two-dimensional transverse structure. Neglecting the temporal behavior, let the electric field amplitude in the focus be given by a Gaussian distribution in the transverse direction that, for small angles to the optical axis, satisfies the paraxial Helmholtz equation [21]

$$\left[i \frac{\partial}{\partial z} + \frac{1}{2k} \left(\frac{\partial^2}{\partial x^2} + \frac{\partial^2}{\partial y^2} \right) \right] E_0(\mathbf{r}) = 0, \quad \text{where} \quad E_0(x, y, z=0) = \mathcal{E}_0 \exp\left(-\frac{x^2 + y^2}{w_0^2}\right). \quad (2.6)$$

Here, w_0 is the radius of the beam waist located at $z = 0$. The paraxial Helmholtz equation assumes that $E_0(\mathbf{r})$ is a slowly varying function in relation to the oscillation of the optical field with frequency ω . Furthermore second order derivatives along the propagation direction z can be neglected. The classical solution of this differential equation is known as the Gaussian beam, which is expressed as a function of z and the transversal coordinate $\rho = \sqrt{x^2 + y^2}$

$$E_0(\rho, z) = \mathcal{E}_0 e^{ikz} e^{i\varphi} \frac{w_0}{w(z)} \exp\left(-\frac{\rho^2}{w(z)^2}\right) \exp\left(i \frac{z}{z_R} \frac{\rho^2}{w(z)^2}\right). \quad (2.7)$$

Here a z -dependent beam radius $w(z)$ was introduced that describes the radial distance, at which the field strength has dropped to $1/e$ of its maximum on-axis value. It describes the radius of the beam along the propagation direction and is given as

$$w(z) = w_0 \sqrt{1 + \left(\frac{z}{z_R}\right)^2} \quad \text{with} \quad z_R = \frac{\pi w_0^2}{\lambda}. \quad (2.8)$$

The quantity z_R is called *Rayleigh* length and describes the distance in propagation direction from the z -position of smallest focus at which the beam area has doubled. Both temporal structure and transverse beam profile are depicted in figure 2.1.

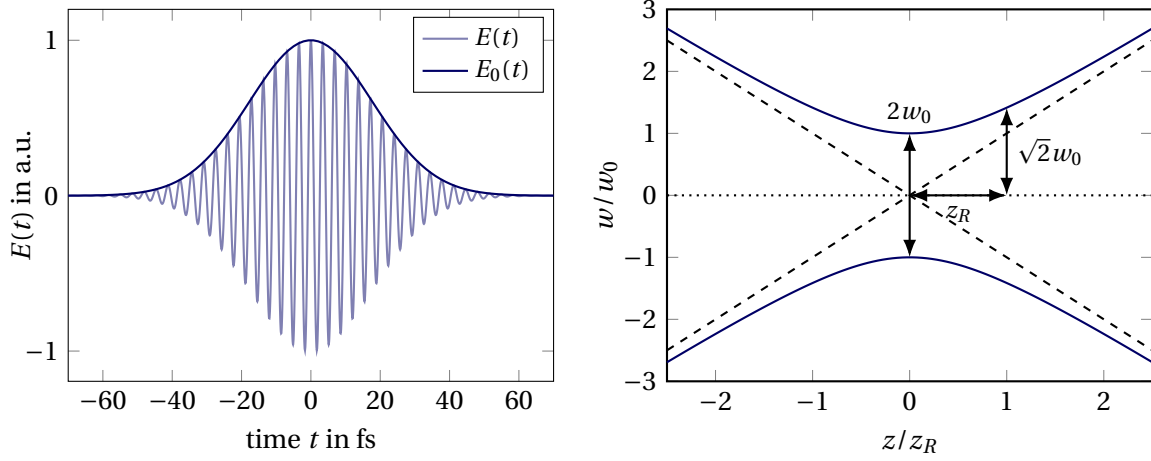


Fig. 2.1: Left: Temporal structure of the electric field and its enveloping Gaussian amplitude for a pulse duration of $\tau = 25$ fs centered at $\lambda_0 = 1030$ nm. Right: Beam width $w(z)$ of a Gaussian shaped transverse beam profile as a function of the propagation length z along the optical axis.

The electric field amplitude $E_0(\mathbf{r}, t)$ is correlated to the intensity I of the pulse as the magnitude of the time-averaged Poynting vector \mathbf{S} (cross product of electric \mathbf{E} and magnetic \mathbf{H} field) over one optical cycle. For dielectric media this is given by

$$I := |\langle \mathbf{S} \rangle| = |\langle \mathbf{E} \times \mathbf{H} \rangle| = \frac{\epsilon_0 c n}{2} |E_0(z, t)|^2, \quad (2.9)$$

with ϵ_0 being the vacuum permittivity, n the refractive index of the surrounding medium and c the vacuum speed of light.

The experimentally important quantity is the intensity of the Gaussian beam in the interaction plane with the target material. The three measurands for determining the intensity are the focal spot size, pulse duration and pulse energy. The pulse duration can be precisely measured by an autocorrelator and the pulse energy with a suitable pyroelectric energy measuring head. The focal size in the interaction plane can either be measured experimentally using an imaging system or be approximated using Gaussian optics if the beam of well known size is focused by a lens or parabolic mirror. If the beam radius w of the collimated beam (large Rayleigh length z_R) in front of the lens has been well characterized, the diffraction-limited width w_0 in the focus of the lens with focal length f in the intensity profile is given by [23]

$$w_0 = \frac{2\lambda}{\pi w} \frac{1}{\sqrt{\frac{\lambda^2}{\pi^2 w^4} + \frac{1}{f^2}}} \approx \frac{2\lambda f}{\pi w} \quad \text{for } z_R \gg f \quad \text{and } w \text{ given at } (1/e^2). \quad (2.10)$$

Note that this value is hardly achievable for high power laser pulses like POLARIS but it is a good approximation for low power probe pulses. The total energy E of the laser pulse is given by the radial integral over the transverse directions and a time integral along the temporal profile. For a Gaussian shaped beam of width w_0 ($1/e^2$) and pulse length τ (FWHM) the total energy can be calculated as

$$E = \iint_{-\infty}^{\infty} dx dy \int_{-\infty}^{\infty} dt I_0 \exp\left(-2\frac{x^2 + y^2}{w_0^2}\right) e^{-4\ln 2\left(\frac{t}{\tau}\right)^2} = \frac{\pi w_0^2}{2} \sqrt{\frac{\pi}{4\ln 2}} \tau I_0. \quad (2.11)$$

Then the peak intensity I_0 and fluence F_0 in the laser focus is given by

$$I_0 = E \frac{2}{\tau \pi w_0^2} \sqrt{\frac{4\ln 2}{\pi}} \quad \text{or} \quad F_0 = \frac{2E}{\pi w_0^2}. \quad (2.12)$$

2.2. Generation and description of laser-induced plasmas

A laser pulse can be used to generate a plasma from an initially non-ionized material. For the purpose of this thesis a plasma is defined as “a quasineutral gas of charged and neutral particles which exhibits collective behavior” [24, p. 2]. This means that a plasma is macroscopically electrically neutral and only on small length scales local charge densities occur.

2.2.1. Ionization processes

First, it should be clarified how the electromagnetic field is able to ionize the atoms or molecules of a material. The ionization process requires energy that is supplied by the laser field in form of the absorption of one or more photons. The process of photo-ionization can, depending on the intensity of the laser field and photon energy, be divided into different categories:

Due to the conservation of energy, the absorbed photon transfers all of its energy $E = \hbar\omega$ to the electron, where \hbar is the reduced Planck constant. If the photon energy exceeds the ionization energy E_{ion} of the bound electron in the atom, the electron can leave the atom, which turns into an ionized state. This ionization process is called *photoelectric effect*, which was first described by Einstein in 1906 [25]. The excess energy is carried away by the electron as kinetic energy $E_{\text{kin}} = \hbar\omega - E_{\text{ion}}$. In the experiments of this thesis, water droplets are used as targets to study the plasma expansion and laser-driven ion acceleration. The adiabatic ionization energy of liquid water is $E_{\text{ion}} = 10.1$ eV [26], which exceeds the photon energy of the POLARIS laser at $E_{\text{ph}} = 1.2$ eV. For higher intensities, the probability of two (or more) photons simultaneously interacting with the bound electron increases. This multi-photon ionization (MPI) process is relevant for laser intensities above 10^{10} W/cm² [27, p. 18] and is shown in figure 2.2 (a). According to perturbation theory, the rate Γ_N of this process is given by [27, p. 18] $\Gamma_N = \sigma_N I_L^N$ with σ_N being the cross section of the N -photon interaction. For

2.2 Generation and description of laser-induced plasmas

even higher intensities, the atomic potential V_C of the nucleus is disturbed by the external laser field E_L (potential V_L) resulting in a modified potential $V(x)$ written as

$$V(x) = -\underbrace{\frac{Ze^2}{4\pi\epsilon_0}}_{V_C} \frac{1}{|x|} - \underbrace{eE_L \cdot x}_{V_L}, \quad (2.13)$$

where Z is the charge state of the ion after the ionization process and e the elementary charge. The coordinate system was chosen in such a way that x is along the polarization of the laser field. This description assumes that the electric field is stationary and homogeneous during the interaction. This approximation is valid, because typical ionization processes take place on attosecond scales $t_{\text{ion}} > 30\text{as}$ (according to time-energy uncertainty principle $t_{\text{ion}}E_{\text{ion}} > \hbar/2$ for $E_{\text{ion}} = 10\text{eV}$). Furthermore the atomic scale is in the order of Ångström, whereas the electric field changes on scales of the wavelength (here, $\lambda = 1.03\mu\text{m}$). As it can be seen in figure 2.2 (b), it is now possible that the electron tunnels through the bent Coulomb barrier. Therefore this mechanism is called tunnel ionization (TI). For a specific laser-matter interaction with an intensity I , wavelength λ and ionization energy E_{ion} , the relevant ionization process is determined by the *Keldysh parameter* γ_K [27, p. 20]

$$\gamma_K = \frac{\tau_T}{T_{\text{opt}}} = \frac{\omega}{e} \sqrt{\frac{E_{\text{ion}} m_e c \epsilon_0}{I_L}} \Rightarrow \gamma_K \begin{cases} \lesssim 1 & \text{tunnel ionization (TI)} \\ > 1 & \text{multi-photon ionization (MPI),} \end{cases} \quad (2.14)$$

where m_e is the rest mass of the electron. The Keldysh parameter corresponds to the ratio of the tunneling time τ_T i. e. the classical time of flight of an electron through the potential barrier and the period T_{opt} of the optical field oscillation. Thus the concept of TI will only be relevant for $\gamma_K < 1$.

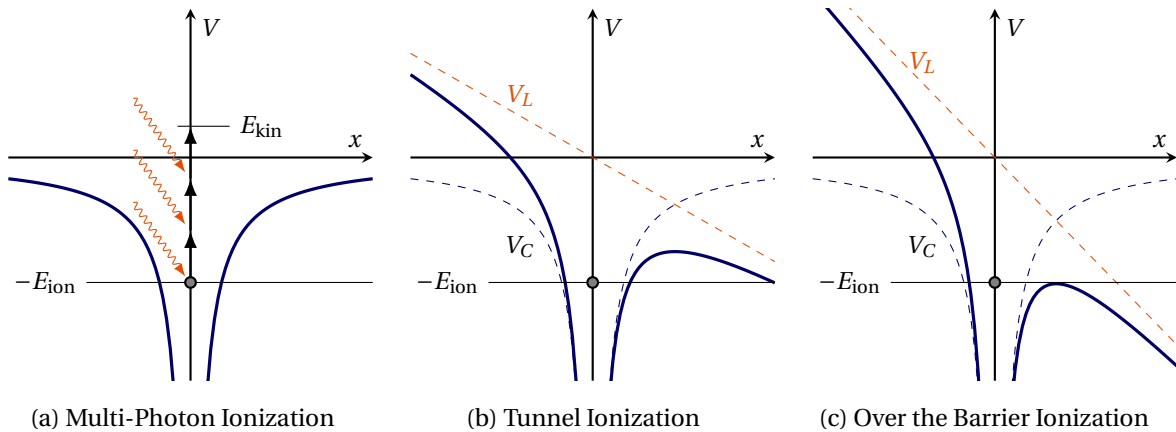


Fig. 2.2: Depiction of the atomic potentials with a bound electron with an ionization energy E_{ion} . The three pictures show different ionization mechanisms. In case of tunnel ionization (TI) and over the barrier ionization (OTBI), the atomic potential is deformed by the laser field potential V_L indicated in orange.

In the WKB approximation², the probability of an electron with energy $E = -E_{\text{ion}}$ tunneling through the barrier is given by [28, p. 112]

$$T = \frac{|\Psi(x_{\text{end}})|^2}{|\Psi(0)|^2} = \exp\left(-\frac{2}{\hbar} \int_0^{x_{\text{end}}} p(x) dx\right) \quad \text{with} \quad p(x) = \sqrt{2m_e(V(x) - E)}. \quad (2.15)$$

Here, $\Psi(x)$ is the electron wave function and x_{end} the tunnel exit position. For low field strengths the Coulomb part $V_C(x)$ can be approximated as a Dirac delta potential and the equation becomes analytically solvable. The tunnel exit position is then given by $x_{\text{end}} = E_{\text{ion}}/(eE_L)$ and the tunnel rate is

$$T = \exp\left(-\frac{2}{\hbar} \int_0^{E_{\text{ion}}/(eE_L)} \sqrt{2m_e(E_{\text{ion}} - eE_L x)} dx\right) = \exp\left(-\frac{4}{3} \frac{\sqrt{2m_e}}{\hbar eE_L} E_{\text{ion}}^{3/2}\right). \quad (2.16)$$

In case the barrier is suppressed down to the electron's ionization level, the electron can be released into vacuum without the need of a tunneling process. This regime is called OTBI and displayed in figure 2.2 (c). The intensity threshold can be derived by equating the maximum of $V(x)$ with the ionization energy E_{ion} of the electron, which results in [27, p. 21]

$$I = \frac{\varepsilon_0 c}{2} |E|^2 = \frac{c\varepsilon_0}{32} \frac{(4\pi\varepsilon_0)^2}{e^6 Z^2} (E_{\text{ion}})^4 = 4 \cdot 10^9 \text{ W/cm}^2 \left(\frac{E_{\text{ion}}}{1 \text{ eV}}\right)^4. \quad (2.17)$$

2.2.2. Plasma properties

Debye shielding The macroscopic charge neutrality of a plasma results from the electrical and thermal conductivity due to the mobility of the charge carriers. This results in a shielding behavior against static electric fields, such as fields from positive ions (charge Q) within the plasma. In a steady-state condition the conservative E field leads to a spherical symmetric distribution of the density of electrons $n_e(r)$ and charged ions $n_i(r)$ as [29, p. 274]

$$n_e(r) = n_0 \exp\left(\frac{e\Phi(r)}{k_B T}\right) \quad \text{and} \quad n_i(r) = n_0 \exp\left(-\frac{q\Phi(r)}{k_B T}\right), \quad (2.18)$$

where k_B is the Boltzmann constant, n_0 the density of the undisturbed plasma and T the temperature of electrons and ions. The latter is directly linked to the averaged kinetic energy and assumed to be the same for both types of particles. For a small electrostatic potential $e\Phi(r) \ll k_B T$, equation (2.18) can be linearly expanded and Poisson's equation $\varepsilon_0 \Delta\Phi(r) = -\rho(r)$ can be solved in spherical coordinates in the following way [29, p. 276]

$$\Phi(r) = \frac{1}{4\pi\varepsilon_0} \frac{Q}{r} \exp\left(-\sqrt{2} \frac{r}{\lambda_D}\right) \quad \text{with} \quad \lambda_D = \frac{\varepsilon_0 k_B T}{n_0 e^2}. \quad (2.19)$$

²The Wentzel Kramers Brillouin (WKB) approximation assumes that the wavelength $\lambda = 2\pi\hbar/p$ of the electron wavefunction is much shorter than the typical distance over which $V(x)$ varies.

The characteristic length scale λ_D is called *Debye length*. For distances larger than λ_D the charge Q is effectively shielded.

Plasma frequency Another collective effect is the oscillation of electrons caused by restoring electric forces towards charge neutrality. Here, the corresponding characteristic frequency is known as the *plasma frequency*. The massive ions do not have time to respond to these fast oscillations and are therefore assumed to be fixed. Assuming no magnetic fields and neglecting thermal motion of the electrons, the plasma frequency ω_p of an infinitely extended, one-dimensional plasma can be derived as [24, p. 81]

$$\omega_p = \sqrt{\frac{n_0 e^2}{\epsilon_0 m_e}}. \quad (2.20)$$

The plasma frequency is only dependent on the electron density n_0 and does not depend on the wavenumber k of the oscillation. Therefore, the plasma oscillation is a standing wave and does not propagate ($v_g = \frac{\partial \omega}{\partial k} = 0$).

Plasma expansion The expansion of a finitely extended plasma into vacuum is driven by thermal motion of the electrons and ions. For a planar plasma with a single ion species with density n_{i0} , the electron density on length scales larger than the Debye length is given by $n_{e0} = Z n_{i0}$, where Z is the ion charge state. In an isothermal and one-dimensional model, where the ions are treated as a non-stationary fluid, the density profile of the plasma as a function of space x and time t is given by an exponential function [30, p. 117]

$$n_e(x, t) = n_{e0} \exp\left(-\frac{x}{c_s t}\right) \quad \text{with} \quad c_s = \sqrt{\frac{k_B T_e Z}{m_i}} \approx 3.1 \cdot 10^5 \frac{\text{m}}{\text{s}} \sqrt{\frac{k_B T_e Z}{\text{keV } A}}. \quad (2.21)$$

Here, c_s is the ion sound speed, m_i the ion mass and A the atomic mass number. The product $L = c_s t$ defines a characteristic length called *plasma scale length*. The time-averaged kinetic energy $k_B T_e$ of *hot* electrons in a relativistic-intensity laser-plasma interaction was estimated by Wilks et al. [31] to be

$$k_B T_e = m_e c^2 (\bar{\gamma} - 1) \quad \text{with} \quad \bar{\gamma} = \sqrt{1 + \frac{I_L \lambda_L^2}{1.37 \cdot 10^{18} \text{ W } \mu\text{m}^2}}. \quad (2.22)$$

$\bar{\gamma}$ is the cycle-averaged relativistic Lorentz factor, which depends on the laser intensity I_L and wavelength λ_L . For a high-intensity laser pulse with $I_L = 4 \cdot 10^{19} \text{ W/cm}^2$ and a wavelength $\lambda_L = 1030 \text{ nm}$, the kinetic energy of the electrons is $k_B T_e \approx 2.4 \text{ MeV}$. For a hydrogen plasma ($Z/A = 1$), the ion sound speed is then determined to be $c_s \approx 15 \mu\text{m/ps}$. This value will be compared to experimental results (c. f. chapter 3.4.1).

2.2.3. Pulse propagation in plasmas

The propagation of transverse electromagnetic waves in a plasma can be described by modifying the Helmholtz equation with a source term accounting for currents, due to the motion of charged particles

$$\left(\Delta + \frac{\omega^2}{c^2}\right)\mathbf{E}(\mathbf{r}, t) = \frac{1}{c^2\epsilon_0} \frac{\partial \mathbf{j}}{\partial t}. \quad (2.23)$$

The current \mathbf{j} is entirely caused by electron motion, since the ions have much higher inertia due to their larger mass ($m_p/m_e = 1836$). The current is then $\mathbf{j} = -n_0 e \mathbf{v}_e$ where \mathbf{v}_e is the electron velocity. Assuming a plane wave dependence, the time derivative can be written as $\frac{\partial \mathbf{j}}{\partial t} = -i\omega \mathbf{j}$. In a linearized and classical equation of motion the current is linearly dependent on the electric field [32, sec. 2.5]

$$m_e \frac{\partial \mathbf{v}_e}{\partial t} = -e\mathbf{E} \Rightarrow \mathbf{j} = i \frac{n_0 e^2}{m_e \omega} \mathbf{E}. \quad (2.24)$$

Then equation (2.23) can be rewritten to

$$(\Delta c^2 + \omega^2)\mathbf{E}(\mathbf{r}, t) = \omega_p^2 \mathbf{E} \quad \text{with} \quad \omega_p^2 = \frac{n_0 e^2}{\epsilon_0 m_e}, \quad (2.25)$$

with the previously introduced *plasma frequency* ω_p . Now using $\Delta \rightarrow -k^2$ the dispersion relation of a plasma follows $\omega^2 = k^2 c^2 + \omega_p^2$. The propagation of electromagnetic waves can now be described by the phase velocity of light [29, p. 406]

$$v_{\text{ph}} = \frac{\omega}{k} = \frac{c}{\sqrt{1 - \frac{\omega_p^2}{\omega^2}}} =: \frac{c}{\eta} > c. \quad (2.26)$$

This allows the definition of a refractive index η of the plasma similar to its definition in linear optics given as

$$\eta = \sqrt{1 - \frac{\omega_p^2}{\omega^2}} = \sqrt{1 - \frac{n_0}{n_{\text{cr}}}} \quad \text{where} \quad n_{\text{cr}} = \frac{\omega^2 \epsilon_0 m_e}{e^2}. \quad (2.27)$$

Its can be seen that the refractive index is smaller than one, thus the phase velocity is larger than the speed of light. However, the transport of energy is carried out by the envelope of the electromagnetic wave (such as the pulse envelope). The corresponding velocity is the *group velocity* $v_g = \frac{\partial \omega}{\partial k} = c\eta$, which is smaller than the speed of light. As seen in equation (2.27), the refractive index can be also written in terms of a critical density n_{cr} . For $n_0 > n_{\text{cr}}$ the refractive index becomes imaginary and the electromagnetic waves can no longer propagate inside the plasma, they are exponentially damped.

2.3. Laser pulse generation based on nonlinear effects

The field of nonlinear optics is mainly concerned with describing the generation of new frequencies from high intensity laser pulses in materials. For the generation of laser pulses suitable for probing, a central wavelength far away from the fundamental and second harmonic (SH) frequency of the main laser pulse is required, such that self-emission of the laser-induced plasma can be suppressed with suitable filters. Therefore a proper description of basic nonlinear phenomena is necessary to understand this technique of probe pulse generation.

For high intensity ($I > 10^9 \text{ W/cm}^2$) ultrashort pulses, the response of a material to the applied field depends nonlinearly on the optical field strength $\mathbf{E}(t)$ of the applied laser pulse. In general this response of a material system is called polarization $\mathbf{P}(t)$.

In linear optics the induced polarization is described via response theory where (excluding nonlocal effects) the polarization $\mathbf{P}^{(1)}(t)$ may depend on fields in the past $\mathbf{E}(t')$ with $t' < t$, which can be described by [33, p. 5]

$$P_i^{(1)}(t) = \varepsilon_0 \sum_{j=1}^3 \int_0^{\infty} d\tau \chi_{ij}^{(1)}(\tau) E_j(t - \tau), \quad (2.28)$$

where $\chi_{ij}^{(1)}(\tau)$ is the linear response function and ε_0 is the vacuum permittivity. The former is a time dependent second rank tensor, which is rapidly decaying in time. The indices i, j represent the spatial cartesian coordinates. For the following discussion several assumptions are made. The medium is assumed to react instantaneously to the field strength that, according to Kramers-Kronig relation, means the medium is lossless (no absorption) and exhibits no dispersion. Furthermore only isotropic materials are considered, where the response function is only a scalar quantity. Then equation (2.28) is simplified to [34, p. 2]

$$\mathbf{P}^{(1)}(t) = \varepsilon_0 \chi^{(1)} \mathbf{E}(t). \quad (2.29)$$

In non-resonant nonlinear optics (which is valid for most materials in the visible and near infrared regime where quantum mechanical resonances are negligible), this simplified equation is typically generalized by expressing the polarization $\mathbf{P}(t)$ as a power series in the field strength [34, p. 2]

$$\mathbf{P}(t) = \varepsilon_0 [\chi^{(1)} \mathbf{E}(t) + \chi^{(2)} \mathbf{E}^2(t) + \chi^{(3)} \mathbf{E}^3(t) + \dots], \quad (2.30)$$

where the quantities $\chi^{(2)}$ and $\chi^{(3)}$ are called second- and third-order nonlinear susceptibilities, respectively. For inversion symmetric materials³ as gases or amorphous materials like glass, $\chi^{(2)}$ vanishes and no second (or even) order nonlinear effects occur [34, p. 3]. Then

³For inversion symmetric materials the properties of the material remain unchanged when all particle positions \mathbf{r}_j are set to their inverse position $-\mathbf{r}_j$.

third-order nonlinear effects begin to appear. The following sections will consider both second order (sec. 2.3.1) and third order nonlinearities (sec. 2.3.2).

2.3.1. Non-collinear Optical Parametric Amplification (NOPA)

In this section, nonlinear effects involving second order nonlinearities are considered. An ultrashort pulse typically consists of a range of frequency components due to the time-bandwidth limitation (c. f. equation (2.5)). In a simple model consider a plane wave field of two distinct frequency components represented in the form

$$\mathbf{E}(t) = \frac{1}{2}(\mathcal{E}_1 e^{-i\omega_1 t} + \mathcal{E}_2 e^{-i\omega_2 t}) + \text{c.c.} \quad \text{and} \quad \mathbf{P}^{(2)}(t) = \varepsilon_0 \chi^{(2)} \mathbf{E}^2(t). \quad (2.31)$$

Then the second order nonlinear polarization $\mathbf{P}^{(2)}(t)$ can be calculated by squaring $\mathbf{E}(t)$ and is given by [34, p. 7]

$$\begin{aligned} \mathbf{P}^{(2)}(t) = & \frac{\varepsilon_0 \chi^{(2)}}{4} \left[\underbrace{\mathcal{E}_1^2 e^{-2i\omega_1 t} + \mathcal{E}_2^2 e^{-2i\omega_2 t}}_{\text{SHG}} + \underbrace{2\mathcal{E}_1 \mathcal{E}_2 e^{-i(\omega_1 + \omega_2)t}}_{\text{SFG}} + \underbrace{2\mathcal{E}_1 \mathcal{E}_2^* e^{-i(\omega_1 - \omega_2)t}}_{\text{DFG}} + \text{c.c.} \right] \\ & + \frac{\varepsilon_0 \chi^{(2)}}{2} \left[\underbrace{|\mathcal{E}_1|^2 + |\mathcal{E}_2|^2}_{\text{OR}} \right], \end{aligned} \quad (2.32)$$

where the various terms correspond to different nonlinear processes such as second harmonic generation (SHG), sum frequency generation (SFG), difference frequency generation (DFG) and optical rectification (OR). Even though four different frequency components are present in the nonlinear polarization, in reality only one component will be dominant since for the generation of appreciable signal intensity, a phase-matching condition must be satisfied [34, p. 8].

For the following discussion, only DFG is described. Here, the generated frequency is the difference of the applied fields. In a photon energy-level description the atom of the material absorbs a photon of the so called *pump* frequency ω_p and jumps to a virtual energy level, which decays via a two-photon emission process. The emission is stimulated by the presence of the *signal* field ω_s (also called seed) creating another photon of frequency ω_s and due to energy conservation an *idler* photon of frequency $\omega_i = \omega_p - \omega_s$. The process of amplification using DFG is illustrated in figure 2.3.

These kind of processes are called *parametric*. According to Boyd [34, p. 14] “the word parametric has come to denote a process in which the initial and final quantum-mechanical states of the system are identical.” Thus, only virtual quantum levels are involved.

In order to construct an optical parametric amplifier (OPA), a strong pump field at ω_p and a weaker signal field at ω_s are adjusted for temporal and spatial overlap and directed onto a nonlinear crystal, which is phase-matched to allow parametric amplification. The signal

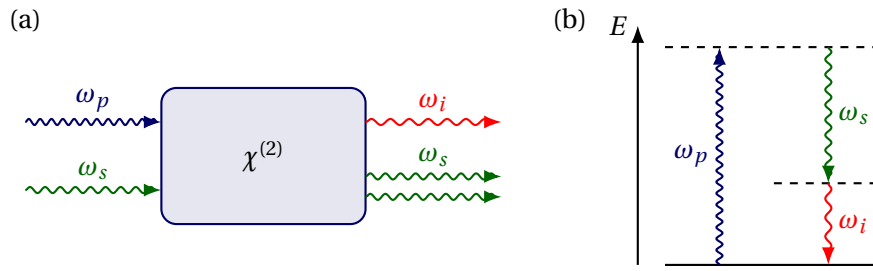


Fig. 2.3: Process of difference frequency generation (DFG). (a) Geometry. The pump photon is converted to two photons ω_s and $\omega_i = \omega_p - \omega_s$. (b) Energy-level description. The pump photon rises the atom to a virtual level, which decays stimulated via the photon ω_s . Adapted from [34, Fig. 1.2.3].

field is amplified at the output and a new idler wave at ω_i is generated. Most commonly the seed is a weak (possibly sub- μJ), but tunable pulse in the visible/infrared regime [35, p. 247]. This results in a strong and tunable output pulse together with a longer-wavelength idler beam. Some crystals allow phase-matching over a broad bandwidth, which allows the generation of ultrashort signal pulses of durations below 5 fs [35, p. 247]. In order to achieve a broad phase-matching bandwidth, the phase mismatch Δk given by

$$\Delta k = k_p - k_s - k_i = \frac{1}{c}(\omega_p n_p - \omega_s n_s - \omega_i n_i) \quad (2.33)$$

is expanded in a Taylor series around the signal frequency. Then higher order terms can be compensated by introducing angles between the three waves [19, p. 19], which leads to the setup of a non-collinear optical parametric amplifier (NOPA). The phase-matching diagram corresponding to this geometry is displayed in figure 2.4.

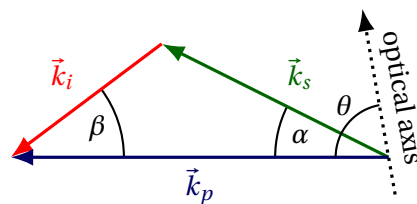


Fig. 2.4: Phase-matching diagram of the nonlinear parametric amplification with a pump-signal cross angle α and phase-matching angle θ for the signal k_s , idler k_i and pump k_p wave vectors. The nonlinear crystal is usually cut in a way that the pump signal is normal incident on the crystal. In case of perfect phase-matching, the three vectors form a closed triangle. Adapted from [19, Fig. 7].

Typical materials used for parametric amplification are birefringent crystals like β -barium borate (BBO), which possesses high nonlinearity, resistance to laser damage and a large negative birefringence ($n_e < n_o$) [34, p. 115]. In case of BBO a type-1 phase-matching process (o-o-e) is used, where the pump is polarized along the extraordinary axis (e), whereas the signal and idler are polarized along the ordinary axis (o). In the non-collinear geometry the

2.3 Laser pulse generation based on nonlinear effects

parallel Δk_{\parallel} and perpendicular Δk_{\perp} mismatch relative to the signal's \mathbf{k} -vector must vanish:

$$\begin{aligned}\Delta k_{\parallel} &= k_p \cos \alpha - k_i \cos(\alpha + \beta) - k_s = 0 \\ \Delta k_{\perp} &= k_p \sin \alpha - k_i \sin(\alpha + \beta) = 0.\end{aligned}\tag{2.34}$$

For a given angle α , this system of equations can be solved by angle-tuning of the pump vector k_p (varying the phase-matching angle θ) [36]

$$k_p(\omega_p, \theta) = \frac{\omega_p}{c} \frac{n_o(\omega_p) n_e(\omega_p)}{\sqrt{n_o^2(\omega_p) \sin^2 \theta + n_e^2(\omega_p) \cos^2 \theta}}.\tag{2.35}$$

This can be used to calculate the phase-matching angle θ as a function of the signal frequency for a given value of α as shown in figure 2.5 (left). Broadband phase-matching is achieved when the phase-matching angle θ does not change in a large wavelength range. For the type-1 phase-matching in BBO and a pump wavelength at 515 nm, the *magic* pump-signal angle $\alpha = 2.6^\circ$ with a signal wavelength $\lambda_s = 800$ nm offers ultra-broadband phase matching for $\theta = 24.6^\circ$ [36]. For the BBO crystal used at POLARIS, the gain spectrum was simulated in [19, p. 22] for different pump-signal angles α using the coupled wave equations. This is depicted in figure 2.5 (right).

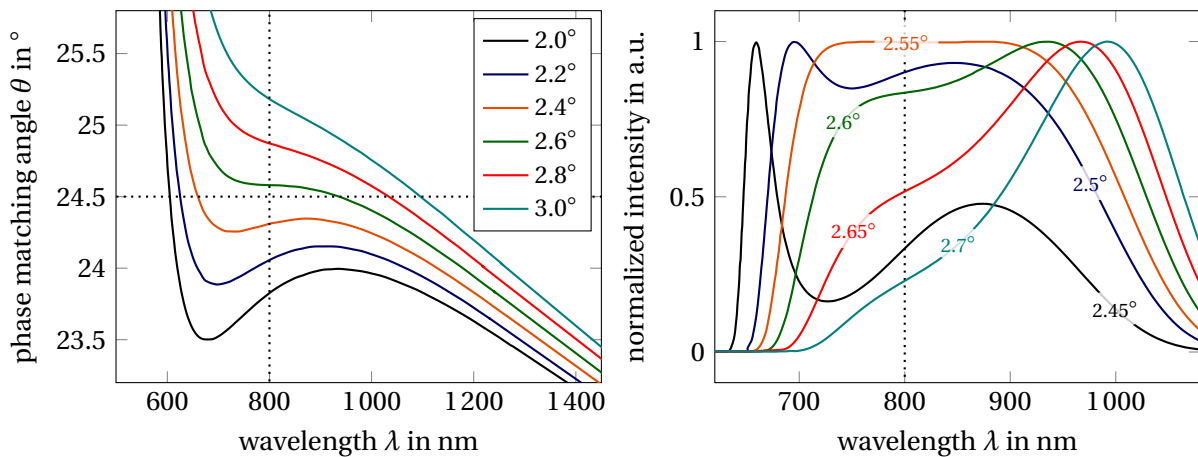


Fig. 2.5: Left: Type-1 phase-matching angle θ as a function of the signal wavelength λ_s for different pump-signal angles α with a pump wavelength at 515 nm. Figure adapted from [36, Fig. 3]. Right: Calculated gain spectra for a phase matching angle of $\theta = 24.5^\circ$ as a function of signal wavelength λ_s for different pump-signal angles α . Figure adapted from [19, Fig. 60].

2.3.2. Self Phase Modulation (SPM)

Self phase modulation (SPM) is a nonlinear optical effect, which occurs when short optical pulses with high intensities propagate through isotropic, nonlinear optical media with high 3rd-order nonlinearity $\chi^{(3)}$. The propagation along the z -axis can be examined by studying the wave equation of a plane wave in a nonlinear, inversion symmetric medium derived in appendix A.1

$$\left(\frac{\partial^2}{\partial z^2} - \frac{n_0^2}{c^2} \frac{\partial^2}{\partial t^2} \right) \mathbf{E} = \frac{1}{c^2 \epsilon_0} \frac{\partial^2}{\partial t^2} \mathbf{P}^{(3)} \quad \text{with} \quad \mathbf{P}^{(3)} = \frac{3}{4} \epsilon_0 \chi^{(3)} |\mathbf{E}|^2 \mathbf{E}, \quad (2.36)$$

where n_0 is the refractive index of the medium. Note that this equation assumes that the nonlinear medium is non-dispersive $n \neq n(\lambda)$. Therefore, this theory excludes group velocity dispersion (GVD) effects. For the purpose of this thesis this approximation is valid, since the interaction length in the thin materials used for SPM is small. A full description including these effects, which leads to the nonlinear Schrödinger equation (NLS), can be found in appendix A.2. With the plane wave ansatz $\mathbf{E}(t) = \mathcal{E} e^{i(kz - \omega t)}$ with envelope \mathcal{E} , a slowly varying envelope approximation (SVEA) can be introduced where the second order derivatives $\frac{\partial^2 \mathcal{E}}{\partial t^2}$ and $\frac{\partial^2 \mathcal{E}}{\partial z^2}$ can be neglected. This is justified for Gaussian pulses with pulse durations ranging over several tens of optical cycles. Then the wave equation simplifies to (for derivation see equations (A.5) to (A.9))

$$\left(\frac{\partial}{\partial z} + \frac{n_0}{c} \frac{\partial}{\partial t} \right) \mathcal{E} = -\frac{3}{4} \frac{k_0}{2in_0} \chi^{(3)} |\mathcal{E}|^2 \mathcal{E}. \quad (2.37)$$

Splitting the slowly varying field into phase and amplitude $\mathcal{E} = |\mathcal{E}| e^{i\Phi}$ yields as a solution for the phase

$$\Phi(z, t) = \Phi_0 + \frac{3}{4} \frac{k_0}{2n_0} \chi^{(3)} |\mathcal{E}|^2 z. \quad (2.38)$$

Φ_0 is the time dependent phase $\Phi_0 = \omega_0 t$ of the laser pulse. This means the high intensity of the pulse induces a change in the refractive index, which is commonly called the *optical Kerr effect* [34, p. 375]

$$n(t) = n_0 + n_2 I(t), \quad \text{where} \quad n_2 = \frac{3\chi^{(3)}}{4\epsilon_0 n_0^2 c} \quad \text{and} \quad I(t) = \frac{n_0 \epsilon_0 c}{2} |E(z, t)|^2. \quad (2.39)$$

For a medium with instantaneous response and sufficiently small length, the only effect of the medium is to change the phase of the transmitted pulse by

$$\Phi_{\text{NL}}(t) = -n_2 I(t) k_0 L, \quad (2.40)$$

where $z = L$ is the length of the nonlinear medium. The time varying phase will modify the spectrum of the pulse. The output beam will show a self-induced spectral broadening.

2.3 Laser pulse generation based on nonlinear effects

The spectral intensity can be calculated via a Fourier transform (FT) as [34, p. 376]

$$S(\omega) = \left| \int_{-\infty}^{\infty} E(t) e^{-i(\omega_0 t + \Phi_{\text{NL}}(t))} e^{i\omega t} dt \right|^2. \quad (2.41)$$

A promising material for generating strong SPM is poly allyl diglycol carbonate (CR-39), a plastic ($n_0 = 1.495$) with a nonlinear refractive index of $n_2 = 6.24 \cdot 10^{-7} \text{ cm}^2/\text{GW}$ [37]. A simulation based on equation (2.41) and considering CR-39 foil is performed in figure 2.6.

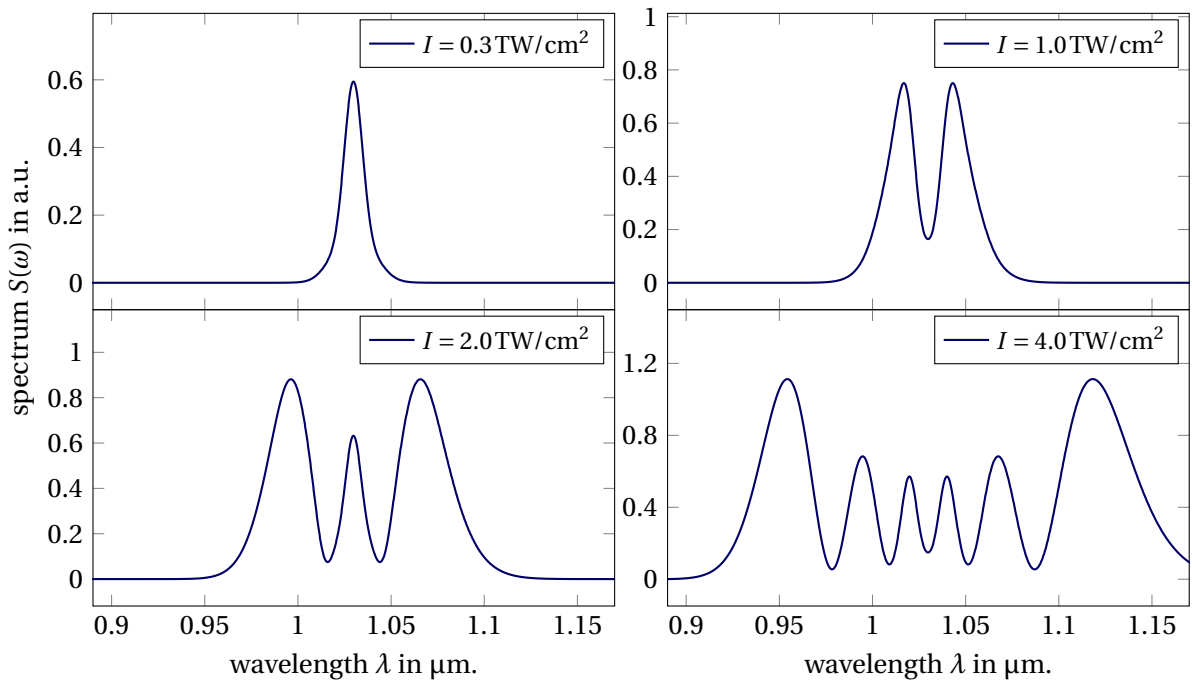


Fig. 2.6: Simulated spectra of a laser pulse with $\tau = 130 \text{ fs}$ (FWHM) propagating through a 1 mm thick foil of CR-39 at different intensities. Nonlinear effects are observed for intensities $I > 0.3 \text{ TW}/\text{cm}^2$ as new frequencies are generated via SPM in the medium. The effect is a symmetric periodic change in spectral intensity. Note the different scalings of the amplitude. For higher intensities the observed SPM signal is larger.

The observed spectrum is symmetric with respect to the frequency of the incoming laser pulse, because the nonlinear phase $\Phi_{\text{NL}}(t)$ is proportional to the intensity and thus also symmetric. The structure of the resulting spectrum can be explained as follows [38, p. 10]: For each point on the Gaussian shaped curve $\Phi_{\text{NL}}(t)$ there exists another point with the same slope $\frac{\partial \Phi}{\partial t} = -\Delta\omega$, which corresponds to the variation of the instantaneous frequency ω_0 . Both points describe waves radiated with the same frequency, hence they will interfere with each other according to their phase difference as illustrated in figure 2.7. This leads to interference that gives rise to peaks/valleys in the spectrum when the phase differences reaches values of even/odd multiples of π .

For the determination of the total spectral broadening induced by SPM, the position of the

2.3 Laser pulse generation based on nonlinear effects

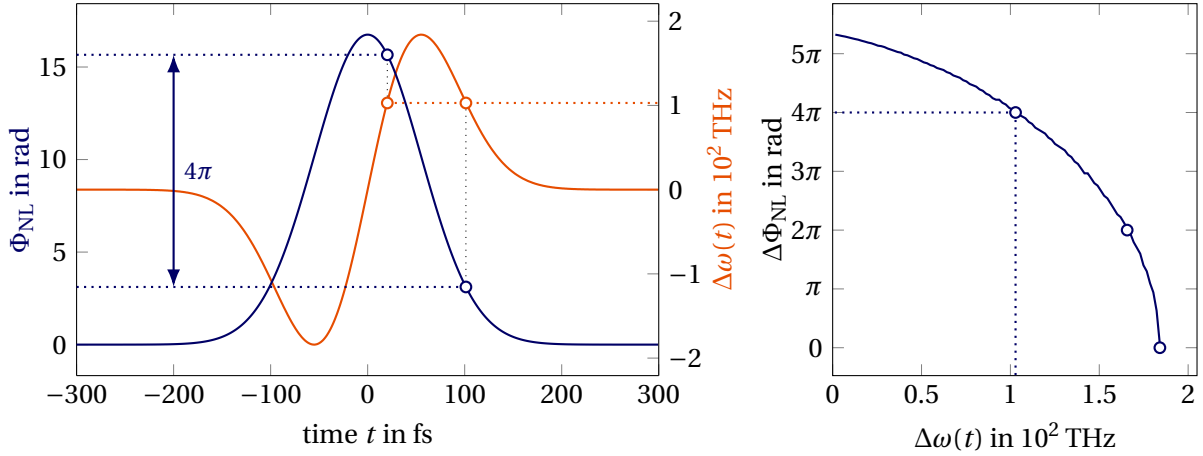


Fig. 2.7: Left: Nonlinear phase (blue) for a pulse with $\tau = 130$ fs (FWHM) of peak intensity $I_0 = 4$ TW/cm² for 1 mm of CR-39. The instantaneous frequency change $\Delta\omega = -\frac{\partial\Phi_{NL}}{\partial t}$ is shown in orange. For each point along $\Phi_{NL}(t)$ exists another point with the same slope (orange points), which corresponds to two generated waves of the same frequency. If the phase difference between both points is a multiple of 2π , the generated waves will constructively interfere. Right: Calculated phase difference as a function of instantaneous frequency change. At three points the phase change will lead to perfect constructive interference. Thus the spectrum (c. f. figure 2.6 bottom right) will exhibit three peaks for the anti-Stokes (high frequency) part of the spectrum.

maximum frequency shift is important. This shift is of the order of [34, p. 376]

$$\delta\omega_{\max} \approx \frac{\Phi_{NL}^{\max}}{\tau_{FWHM}}, \quad \text{where } \Phi_{NL}^{\max} = n_2 I_0 k_0 L. \quad (2.42)$$

Here, τ_{FWHM} describes the pulse duration at FWHM. According to the description in figure 2.7, the number N of frequency peaks in the whole spectral domain is given by

$$N = 2 + 2 \left\lfloor \frac{\Phi_{NL}^{\max}}{2\pi} \right\rfloor. \quad (2.43)$$

The constant number two takes into account the two outer-most peaks of the spectrum, which will merge together in the limit of vanishing nonlinear phase. The second factor of two includes the generation of spectral peaks on both the anti-Stokes (high frequency) and Stokes (low frequency) side of the spectrum.

2.3.3. Pulse steepening

The simple theory of SPM neglects second order derivatives in the electric field and yields a symmetric, broadened spectrum as already seen in figure 2.6. However, for short pulses an asymmetric spectrum emphasizing the *blue* part of the spectrum is observed, which cannot be explained with the slowly varying envelope approximation (SVEA) ansatz. Since the refractive index is intensity dependent (c. f. equation (2.39)), the parts in the peak of the pulse will travel slower than the rising and trailing parts. This leads to a deformation of the pulse shape and is called *pulse steepening*. This effect is intrinsic to the SPM process and even occurs in non-dispersive media [39, p.1684]. In the temporal description (c. f. figure 2.8), the instantaneous frequency change in the trailing part of the pulse is higher than at the front and leads to an asymmetric spectral broadening.

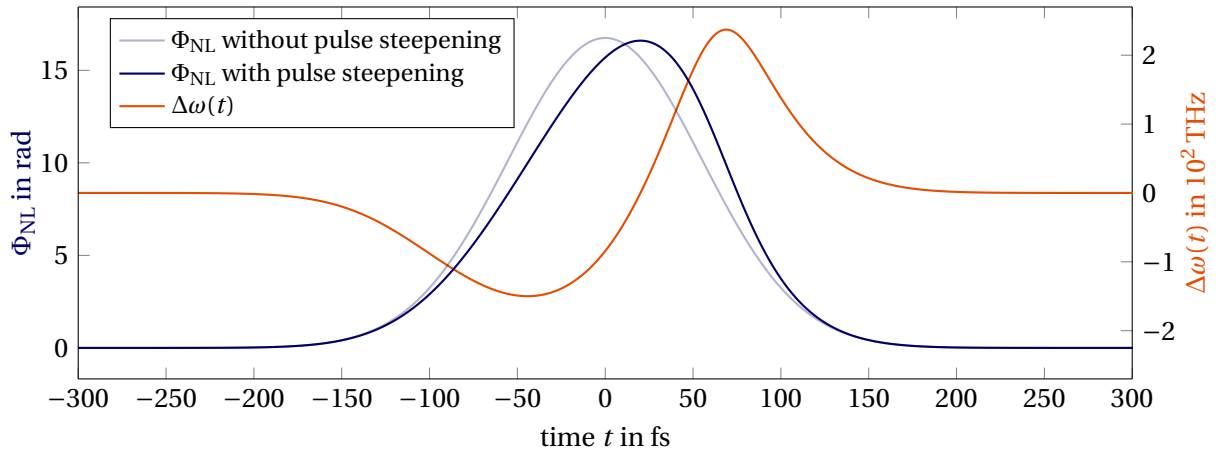


Fig. 2.8: Nonlinear phase (blue) for a pulse with $\tau = 130$ fs (FWHM) of peak intensity $I_0 = 4$ TW/cm² for a 1 mm foil of CR-39 with pulse steepening considered. The instantaneous frequency change $\Delta\omega = -\frac{\partial\Phi_{\text{NL}}}{\partial t}$ is shown in orange. It shows an asymmetric behaviour, as the magnitude of $\Delta\omega$ is larger on the trailing edge of the pulse, which leads to larger frequency oscillations in the Anti-Stokes part of the spectrum.

In order to describe pulse steepening, equation (2.37) is written without the considered approximations (c. f. (A.6a), (A.6b) and (A.8))

$$\left(\frac{\partial}{\partial z} + \frac{n_0}{c} \frac{\partial}{\partial t}\right)\mathcal{E} + \frac{1}{2ik} \left(\frac{\partial^2}{\partial z^2} - \frac{n_0^2}{c^2} \frac{\partial^2}{\partial t^2}\right)\mathcal{E} = \frac{1}{2ik} \frac{3\omega_0^2}{4c^2} \left(\frac{1}{\omega_0^2} \frac{\partial^2}{\partial t^2} - \frac{2i}{\omega_0} \frac{\partial}{\partial t} - 1\right) \chi^{(3)} |\mathcal{E}|^2 \mathcal{E}. \quad (2.44)$$

Here, the approximation of a slowly varying envelope no longer holds for very short and intense laser pulses and second order derivatives of the envelope \mathcal{E} can no longer be neglected. A solution to this equation was suggested by Yang and Shen in 1984 [40]. A detailed derivation of the resulting differential equations is shown in appendix B. The final differen-

tial equation can be written as

$$\frac{\partial \mathcal{E}}{\partial z} + \frac{1}{c} \frac{\partial}{\partial t} (n_0 + \tilde{n}_2 |\mathcal{E}|^2) \mathcal{E} = i \frac{\tilde{n}_2 \omega_0}{c} |\mathcal{E}|^2 \mathcal{E} \quad \text{with} \quad \tilde{n}_2 \stackrel{(2.39)}{=} \frac{\epsilon_0 n_0 c}{2} n_2. \quad (2.45)$$

The new introduced constant \tilde{n}_2 is the nonlinear refractive index defined with regards to squared electric field amplitude rather than intensity. Now, the complex valued envelope is split into amplitude and phase $\mathcal{E} = |\mathcal{E}| e^{i\Phi}$. This ansatz is inserted into (2.45) and the equation is split into real and imaginary part, which leads to the following system of differential equations for amplitude and phase:

$$\left[\frac{\partial}{\partial z} + \frac{n_0}{c} \left(1 + \frac{3\tilde{n}_2}{n_0} |\mathcal{E}|^2 \right) \frac{\partial}{\partial t} \right] |\mathcal{E}| = 0, \quad (2.46)$$

$$\left[\frac{\partial}{\partial z} + \frac{n_0}{c} \left(1 + \frac{\tilde{n}_2}{n_0} |\mathcal{E}|^2 \right) \frac{\partial}{\partial t} \right] \Phi = \frac{\tilde{n}_2 \omega_0}{c} |\mathcal{E}|^2. \quad (2.47)$$

A solution to this system of nonlinear, partial differential equations for a Gaussian shaped input pulse is presented in section 4.3.

2.3.4. Kerr-induced self-focusing

In addition to the temporal shape, the transverse structure of the pulse is relevant for the study of SPM. The accumulated nonlinear phase varies as a function of the transverse coordinates, since it is proportional to the intensity according to equation (2.40). To describe the phase accumulation, the so-called *B*-integral is introduced, which is defined as

$$B(x, y) = \frac{2\pi}{\lambda} \int_0^L n_2 I(x, y, z) dz. \quad (2.48)$$

For the case of a Gaussian-like transversal profile, the value of the B-Integral is larger in the center of the beam than on the edges. This results in phase fronts formed in a lens-like shape, which leads to a nonlinear effect called Kerr *self-focusing*. This is counteracted by the natural diffraction of the Gaussian beam as previously described in section 2.1.2. At the critical power P_{crit} [34, p. 583]

$$P_{\text{crit}} \approx \frac{\lambda_0^2}{8n_0 n_2} \stackrel{\text{CR-39}}{=} 1.42 \text{ MW} \quad \text{at } \lambda_0 = 1030 \text{ nm}, \quad (2.49)$$

the tendency of self-focusing is precisely balanced by diffraction, which results in an effect known as the *self-trapping* of light [34, p. 329]. In this case, the beam travels with a constant diameter. For typical probe pulse energies $E \approx 1 \text{ mJ}$ and pulse lengths $\tau = 130 \text{ fs}$ (FWHM) that are required to induce SPM with sufficient spectral broadening (c. f. the high intensities used in the simulation in figure 2.6), the pulse power is $P = 7.2 \text{ GW}$, which is three orders of magnitude above the critical power of self-focusing. For example, if the beam is guided

in an optical waveguide, the nonlinear phase can become very large, but the input power is limited to the critical power of self-focusing, otherwise the long medium length would lead to strong self-focusing [41].

For pulse broadening with SPM to be successfully performed in the experiment, self-focusing should be negligible, which can be achieved by sufficiently thin nonlinear media. The distance at which the beam of initial size w_0 is focused is given by the *self-focusing distance* z_{sf} [34, p. 332]

$$z_{\text{sf}} = \frac{2n_0 w_0^2}{\lambda_0} \frac{1}{\sqrt{P/P_{\text{cr}} - 1}}. \quad (2.50)$$

So as long as the medium length L is shorter than the self-focusing distance z_{sf} , self-focusing may be neglected in the description of pulse propagation. Since self-focusing is not a function of intensity that bears on the question what pulse properties should be used to minimize the effect of self-focusing. For a target peak intensity of $I = 10 \text{ TW/cm}^2$ the self-focusing distance and necessary pulse radius are summarized in table 2.1 for different pulse energies.

Table 2.1: Self focusing distance z_{sf} and pulse width w_0 for different pulse energies ($\tau = 130 \text{ fs}$) calculated by using (2.12) and (2.50) at a constant peak intensity $I = 10 \text{ TW/cm}^2$.

Energy [mJ]	0.1	0.5	1	2	5
pulse radius w_0 [μm]	48	107	152	214	339
self-focusing distance z_{sf} [mm]	0.30	0.66	0.94	1.32	2.09

The table shows that higher pulse energies are better suited for SPM because the same intensity can be reached for larger pulse radii in the interaction region, which contributes quadratically to the self-focusing distance. For SPM a large self-focusing distance is needed, therefore larger pulse energies for a constant peak intensity are desirable.

3. Probing relativistic laser-plasma interactions with NOPA-based pulses

In this part of the thesis we present the results of the application of an off-harmonic, optical probe pulse for an experiment at the POLARIS laser system with water micro-droplets to investigate the laser-plasma interaction and proton acceleration. In contrast to previous experiments with thin foils, the water droplets have a limited extension in all spatial directions, which facilitates a direct imaging of the plasma expansion using shadowgraphy. The strong emission of the laser-induced plasma at the fundamental and SH frequency of the main pulse requires an off-harmonic probe to realize the imaging. Therefore, first, the description of the NOPA setup (used for probe pulse generation) and its characterization are detailed. Then, we introduce the setup of the laser-matter interaction and elucidate the experimental means of imaging the droplets onto a camera to study the plasma expansion process in a detailed way. We also present a new method that was implemented to reduce the undesirable plasma emission. Finally, a pump-probe experiment was carried out. A detailed analysis of the shadowgraphy images allows us to estimate the plasma expansion velocity.

3.1. The NOPA-based laser pulse generation

To shed light on the different relativistic laser-plasma processes, a high spatio-temporal resolution of the interaction region is needed. Optical probing is a promising tool to extract the information of the interaction via direct imaging. This can be combined with methods like shadowgraphy (c. f. section 3.4) or interferometry [15, Chapt. 4]. The design of the ultrashort optical probe pulse is based on several criteria. First, the way of probe pulse generation is important. For this work, the probe pulse is generated by picking a part of the seed pulse from the oscillator of the main pulse. Here, a complex synchronization of two independent laser systems, as used in similar probing experiments [42], is not necessary. Secondly, the pulse properties should be well controlled. The spatial profile of the beam must be homogeneous and large enough to illuminate the whole interaction region. Then the temporal resolution achieved in the recorded images is primarily given by the probe pulse duration, which should be shorter than the pump pulse in order to be able to resolve processes during the time of interaction. Plasma emissions at the fundamental wavelength and SH of the pump pulse may obscure the measurement, therefore the central wavelength of the probe pulse should be chosen far away from both spectral regimes. A different technique that could be possibly employed in the future, is e. g. *chirped-pulsed probing* [43], where a broad bandwidth ($\Delta\lambda > 100\text{ nm}$) of the probe pulse is needed. Here, a strongly chirped pulse is used to probe the laser-plasma interaction at different times in a single laser shot, as the temporally separated wavelengths interact with the target at different times. For shadowgraphy experiments, the probe pulse could possibly be imaged onto several cameras with different bandpass filters to observe the plasma evolution at different times.

3.1 The NOPA-based laser pulse generation

In case of the POLARIS laser system, which works at a fundamental frequency of 1030 nm and pulse durations of 130 fs, the spectrum of the probe should be in the range between 600–950 nm to avoid overlap with the fundamental wavelength and its SH. Finally, in order to achieve sufficient illumination of the interaction region with the spatial and temporal properties mentioned above, the probe-pulse energy should be above 10 μ J but still in the μ J regime to avoid ionization of the target caused by the probe pulse [19, p. 78].

3.1.1. NOPA setup

This approach of ultrashort optical pulse generation was implemented by Issa Tamer in his PhD thesis [19] at POLARIS in 2020. It utilizes a single pass non-collinear optical parametric amplifier (NOPA) with a μ J-level probe energy and a broad bandwidth between 750–950 nm. In this work, a nonlinear phase-matching mechanism in a birefringent BBO crystal was used to amplify a low energy broadband laser pulse with a single-pass gain on the order of 10^4 [19, p. 79]. The required second harmonic (SH) pump beam to realize the ultra-broadened gain is achieved via SHG of a mJ level pulse in a potassium dideuterium phosphate (KDP) crystal. The pulse is supplied via a chirped pulse amplification (CPA) system with a Ytterbium doped fluoride phosphate (Yb:FP15) regenerative amplifier seeded with a nJ level seed pulse from the POLARIS main oscillator. A detailed description and characterization of the CPA system is performed in appendix C. The system delivers 1.5 mJ pulses with a pulse duration $\tau = 120$ fs (FWHM). Since both the main POLARIS pulse and probe pulse originate from the same oscillator, they can be easily synchronized with each other. Furthermore the probing system can be run independently from the whole five stage amplifier system of the main laser pulse.

The schematic of the white light generation and amplification with the SH of the amplified 1.5 mJ pulse is depicted in figure 3.1. Since the alignment and generation of the white-light continuum (WLC) and SH are crucial for the generation of the NOPA signal, a detailed description of the aligning procedure for the setup is given in appendix D. In general, the spatial and temporal overlap of the SH and white-light pulse needs to be maximized using a motorized delay stage. Furthermore, the non-collinear angle α between pump and signal needs to be optimized using two references in front of and behind the BBO crystal (c. f. figure 3.1). This can be done using the position of the parametric fluorescence ring generated by the strong SH pulse in the directions of phase matching (c. f. appendix D). The synchronization of the generated probe pulse with the main POLARIS laser pulse is realized by placing a photo diode at the target position. The diode is connected to a high resolution oscilloscope, which can resolve single nanosecond time delays. In a first step, the nearest probe seed pulse can be selected with the pulse picker before the stretcher (13 ns). Then a delay stage in front of the amplifier (depicted in figure C.2) is used to temporally overlap both pulses in the sub-nanosecond range.

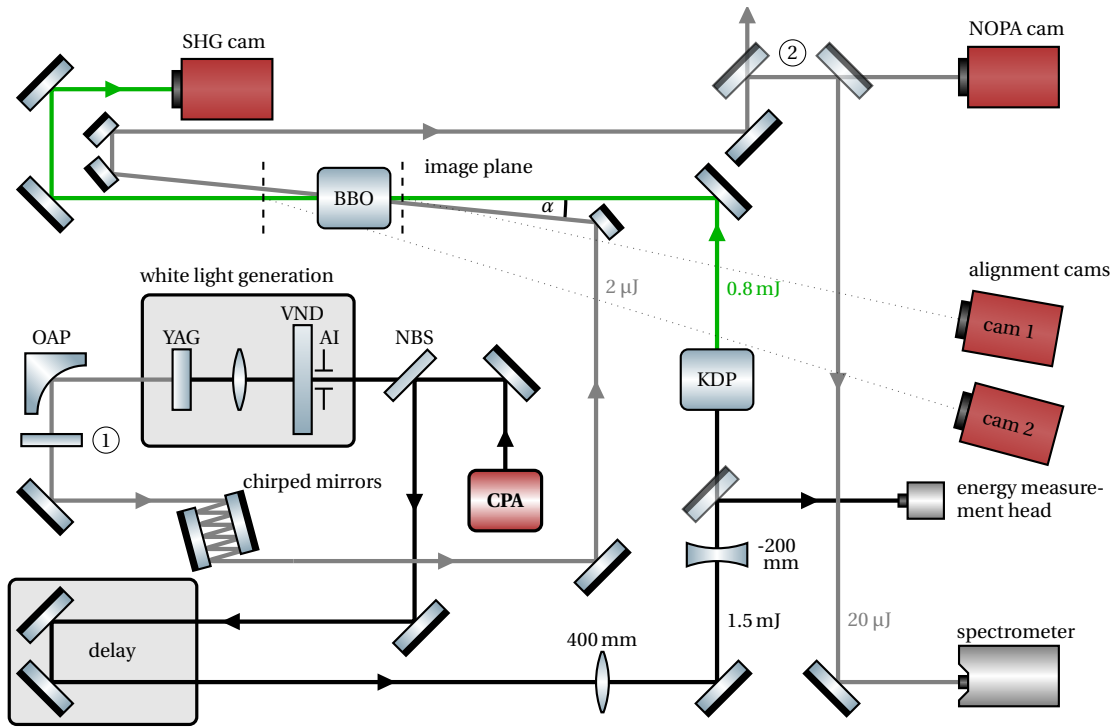


Fig. 3.1: Schematic of the NOPA. An amplified pulse originating from the CPA setup C.2 (marked in red) is split into two beams of different energy by a neutral beam splitter (NBS). The first beam (0.1 % of total energy [19, p. 84]) is used for white light super-continuum generation. The white light generation setup consists of an adjustable iris (AI), variable neutral density filter (VND), a lens (50 mm focal length) and a 5 mm Yttrium aluminium garnet (YAG) crystal positioned at the focus of the lens. The white light is collimated using an off-axis parabola (OAP) (focal length 25.4 mm), filtered with a short-pass filter (1) with a cut-off wavelength of 950 nm and pre-compressed with a chirped mirror pair (seven bounces on each side). The second beam (2 mJ) is reduced in size via a 2:1 telescope and enters a 3 mm thick KDP crystal that generates the second harmonic (SH) at 515 nm to pump the NOPA. The white-light continuum (WLC) and SH pulse are temporally synchronized via a motorized delay stage and sent to a BBO crystal at a specific cross angle $\alpha = 2.65^\circ$ designed for broadband amplification [19, p. 90]. The beam can be sent to the diagnostics or the experiment by using two motorized, removable mirrors (2).

3.1.2. NOPA characterization

The shape, the energy and spectral profile of the NOPA are very sensitive to the stability of the amplified pulse after the CPA-setup. In order to get a stable NOPA signal, the shot to shot variation of the amplifier energy must be less than 10 %. In order to validate that the setup is able to produce a stable NOPA signal, a stability measurement of the amplifier energy was conducted for a time period of several minutes. The measurement is displayed in figure 3.2 (left). Furthermore a stability measurement of the NOPA signal was also conducted in figure 3.2 (right). It can be seen that for an average energy variation of $\pm 5\%$ for the amplifier energy, the NOPA energy exhibits large fluctuations with $\pm 30\%$. The energy fluctuations can

3.1 The NOPA-based laser pulse generation

be tackled by optimizing the input coupling into the amplifier and proper alignment of white light and SH, which generates the NOPA signal. Another issue seems to be thermalisation of the active medium in the CPA-setup, because when the NOPA is operated for several hours, the energy fluctuations become smaller without changing any parameters.

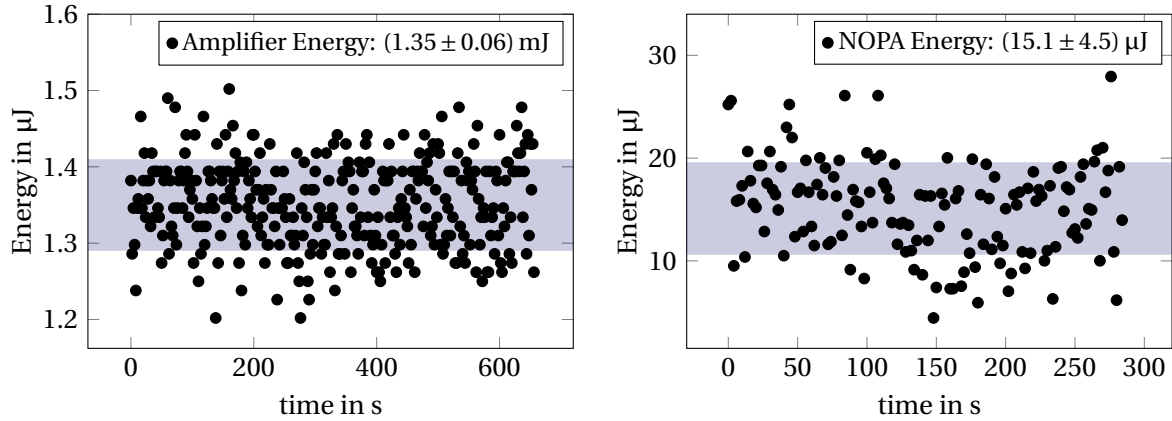


Fig. 3.2: Stability measurement of the amplifier and NOPA energy over a duration of several minutes. The measurement was conducted using two pyroelectric energy measurement heads with calibration factors of 83.2 mV/mJ (Amplifier measurement) and 809 mV/mJ (NOPA measurement). The standard deviation σ of the measured values is indicated with the blue shaded area. The amplifier energy is stable with $\Delta E = \pm 5\%$, however, the NOPA energy fluctuates heavily with $\Delta E = \pm 30\%$.

Finally, the spectrum was analyzed by a spectral sensitivity calibrated *Flame S Ocean Optics* spectrometer (650–950 nm) and is depicted in figure 3.3. The spectral sensitivity curve was calculated using a well characterized tungsten lamp spectrum (c. f. appendix E). It can be seen that for an optimized delay between SH and WLC, a super-broadened spectrum in

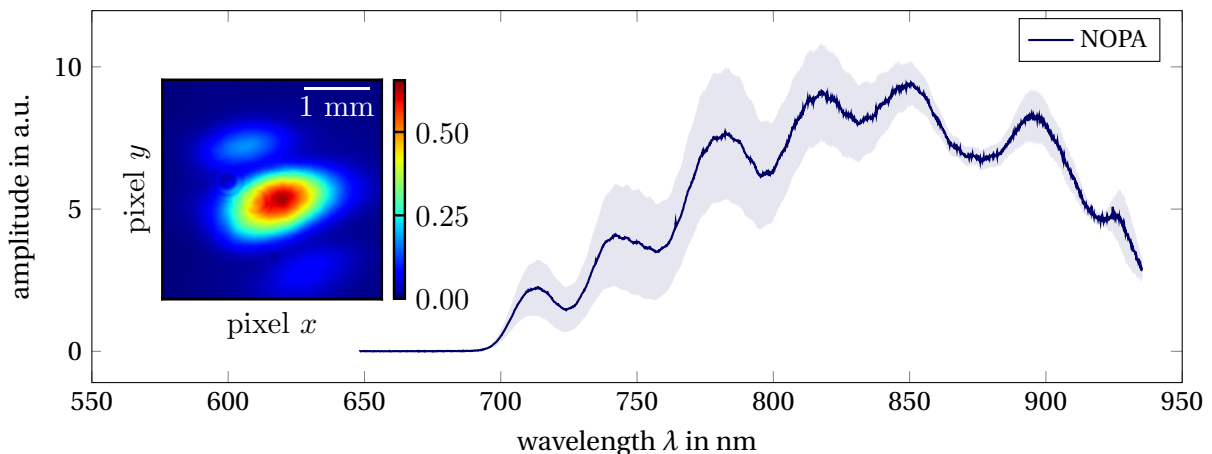


Fig. 3.3: Measured spectrum of the NOPA. The graph shows the averaged spectrum for 60 consecutive shots. The standard deviation is indicated with the shaded area. The inset figure shows the spatial profile of the NOPA recorded by the *NOPA cam* (c. f. figure 3.1). The beam radius was measured along short and long axis of the elliptic shape of the beam profile, which was $w = (0.61 \pm 0.02)$ mm ($1/e^2$) and $w = (0.94 \pm 0.01)$ mm ($1/e^2$) respectively. The values were obtained by using a Gaussian fit.

3.1 The NOPA-based laser pulse generation

the wavelength range 750–950 nm is generated. The spectrum exhibits periodic amplitude modulations. This effect was simulated and experimentally verified in [19, p. 92]. As can be seen from the standard deviation for a measurement of 60 consecutive shots, the spectral amplitude fluctuates by $\pm 20\%$, which was already expected from the energy measurement in figure 3.2. Furthermore the spatial profile is given in the figure. The stability of the energy and shape of the NOPA is mainly influenced by the stability of the white light generation, which can be improved following step 3 of the alignment procedure on page 83. The beam radius of the NOPA profile was also measured. The radius of the long axis of the elliptic shape yields a value of $w = (0.94 \pm 0.01) \text{ mm}$ ($1/e^2$), which corresponds well to previously measured values [19, p. 94]. This beam diameter is sufficient to illuminate the whole interaction region in a pump-probe experiment. Unfortunately, some energy is lost in the periphery of the beam profile (c.f. figure 3.3). The shape of the beam was adjusted in such a way that the energy stability was maximized.

3.1.3. Spectral control

As previously described, the alignment of the white-light continuum (WLC) and SH is crucial for the amplification in the BBO crystal. The phase matching angle θ_{PM} was chosen in such a way (as described on page 14) that the gain is approximately homogeneous in a broad wavelength range. The optimized pump-signal angle is then determined to be $\alpha = 2.6^\circ$ for a central wavelength of 800 nm. The geometry of the beams inside the crystal with their respective polarizations is described in figure 3.4.

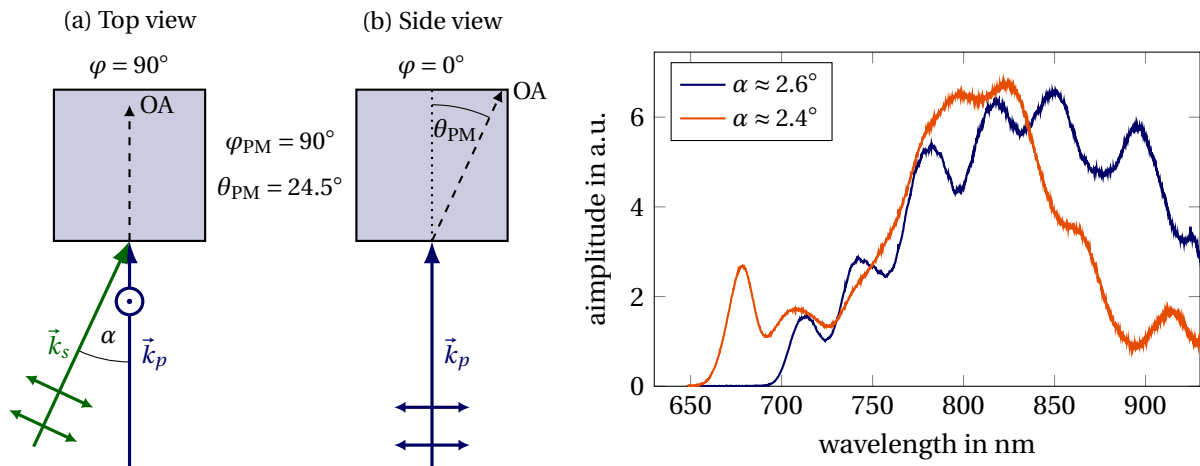


Fig. 3.4: Left: Geometry of the WLC (signal) and SH (pump) beams in the NOPA crystal. (a) shows that the WLC is p-polarized along the ordinary axis and perpendicular to the s-polarized SH. (b) shows that the pump is polarized along the extraordinary crystal axis, which enables the Type I o-o-e phase matching process. Right: NOPA spectra for different non-collinear angles α . The orange curve indicates that the spectral bandwidth can be reduced by an adjustment of the non-collinear angle and subsequent optimization of the temporal delay τ .

For several applications, the spectral profile of the probe pulse needs to be shaped. For example, in the experiment conducted in section 3.4, a higher energy in a small wavelength

range between 780–820 nm was required. This can be achieved by changing the non-collinear angle between pump and WLC slightly towards lower values. The spectrum displayed by the orange curve in figure 3.4 presumably corresponds to $\alpha = 2.4^\circ$ as shown in figure 2.5 (right). The strong gain in the part below 700 nm can be reduced by optimizing the WLC and SH delay τ .

3.2. Experimental setup

The generated probe pulses are used for a pump-probe experiment at the POLARIS laser system. In this experimental setup, a jet of water is generated by a commercial nozzle (Micro Jet Components) driven by a piezo motor. The latter breaks up the jet, forming droplets at a high repetition with a diameter of 20 μm . The experiment is conducted in a large vacuum chamber with the POLARIS main laser beam (100 TW) focused onto the water droplets. The experimental setup with the main components is shown in figure 3.5. The laser pulses are

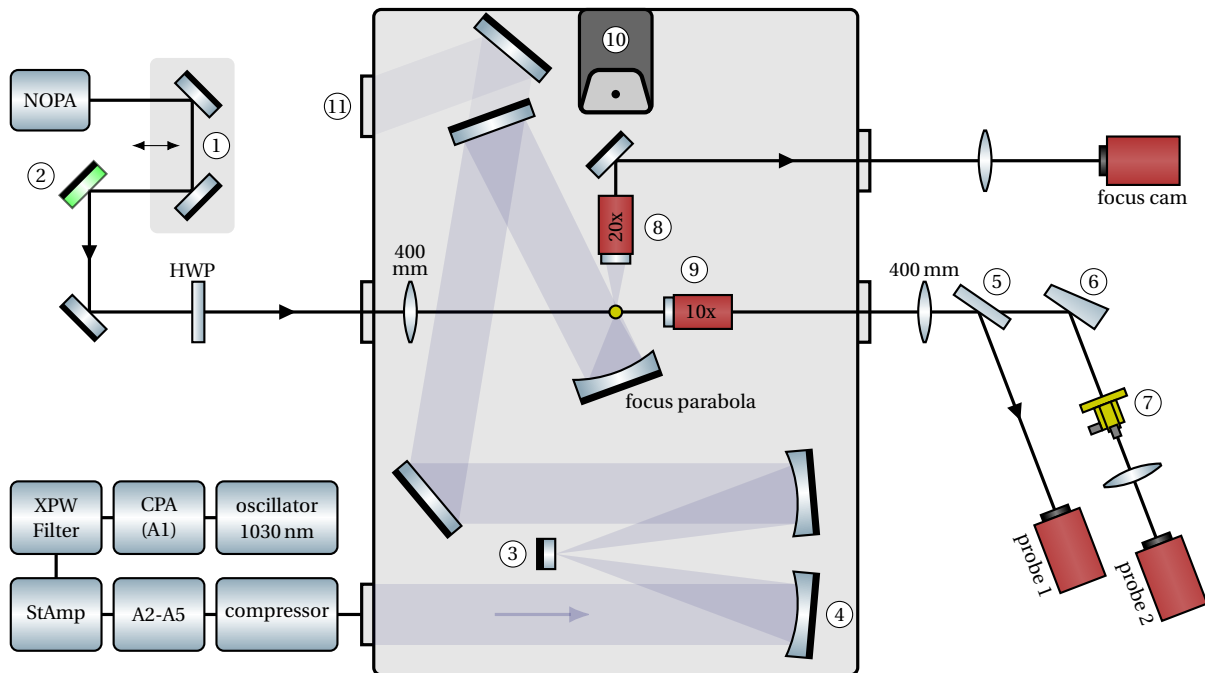


Fig. 3.5: Experimental setup of the laser-matter interaction and the imaging system of the probe. (1) delay stage for pump-probe synchronization and delay measurements, (2) motorized mirror for online probe adjustment, (3) plasma mirror placed 1 cm behind the focus of the first OAP (4), (5) thin glass plate used for splitting the beam, (6) wedged glass plate, (7) corona-graph (c.f. section 3.3), (8) focus objective, (9) probe objective with bandpass filter 800 nm (40 nm FWHM), (10) scintillator with subsequent ion detection setups (Thomson parabola spectrometer, gateable CCD camera), (11) beam towards plasma mirror diagnostics. Note that the setup is not to scale. Bottom left: Simplified schematics of the POLARIS laser beam line adapted from [44].

created in a Yb-doped oscillator (Flint, Light Conversion) with pulse length of $\tau < 90$ fs at 1030 nm central wavelength. Next, the pulses are amplified in a CPA system with a regenerative amplifier stage (A1) to 2 mJ pulses with 1 Hz repetition rate. A non-linear filter based on the generation of a crossed-polarized wave (XPW filter) is used for increasing the temporal intensity contrast [44]. Then the pulses are amplified and stretched in a StAmp setup [45] to 4.5 ns. After that, the pulses are successively amplified in four amplifier stages A2-A5 and finally compressed and sent to the target chamber with a maximum of 10^{21} W/cm² focused on the target [44].

In the target chamber, the main laser pulse is focused onto a plasma mirror (3) using an off-axis parabola ($f = 90$ cm) and re-collimated with a second parabola. The plasma mirror has a low-reflectivity dielectric surface, which transmits most of the pre-pulse energy and the rising-edge of the main pulse. When the intensity increases, electrons are ionized by an absorption mechanism (e. g. multi-photon ionization), which increases the reflectivity due to the formation of an over-dense plasma. The so-called plasma mirror *ignites* and the rest of the laser beam is reflected, which improves the intensity contrast of the rising edge of the pulse [46]. The 30 cm-focal length off-axis parabola (OAP) focuses the 140 mm-diameter beam onto the water micro-droplets. An imaging system consisting of a microscope objective (7), a tube-lens and a camera, is used to monitor the focal spatial profile and position. During the experiment, the focus diagnostic is moved out so the measurement of proton energies using the Thomson parabola spectrometer can take place.

The probe pulses from the NOPA (c.f. figure 3.1) are first sent through a delay stage (1), which is used to adjust the temporal delay between the main pulse and the probe pulse in a sub-picosecond range. Then, the initially horizontal polarization of the probe light is rotated using a half wave plate (HWP) and focused by a 400 mm lens. The focus position was chosen about 10 cm in front of the droplets in order to sufficiently illuminate the whole region of interest homogeneously. Furthermore, the lens is important to ensure a high enough intensity of the probe to outshine the unpolarized self-emission of the plasma in the imaging setup. The imaging was realized with a magnifying microscope objective (8) Mitutoyo Plan Apo NIR 10x, which collimates the light from the droplet position, and a 400 mm tube lens that finally images the interaction region onto the cameras *probe 1* and *probe 2*.

The imaging setup consists of two parts. The probe beam was split with a thin glass plate (4), one part was directly imaged onto a camera (*probe 1*) after the tube lens, whereas the other part was first imaged into a *coronagraph* (4). This setup allows to directly compare the images with and without the coronagraph whose functionality will be described in detail in the next section. A 1:1 imaging system with a lens of $f = 125$ mm is installed in the second beam path to image the droplets onto a second camera (*probe 2*) as shown in figure 3.6.

In the experiment, parts of the strong POLARIS main laser beam at the fundamental wavelength were scattered into the beam path of the probe. Since the main pulse laser energy surpasses the probe pulse energy by six orders of magnitude, even small parts of the scattered light can over-saturate the images. This problem was remedied by placing the glass plate

3.2 Experimental setup

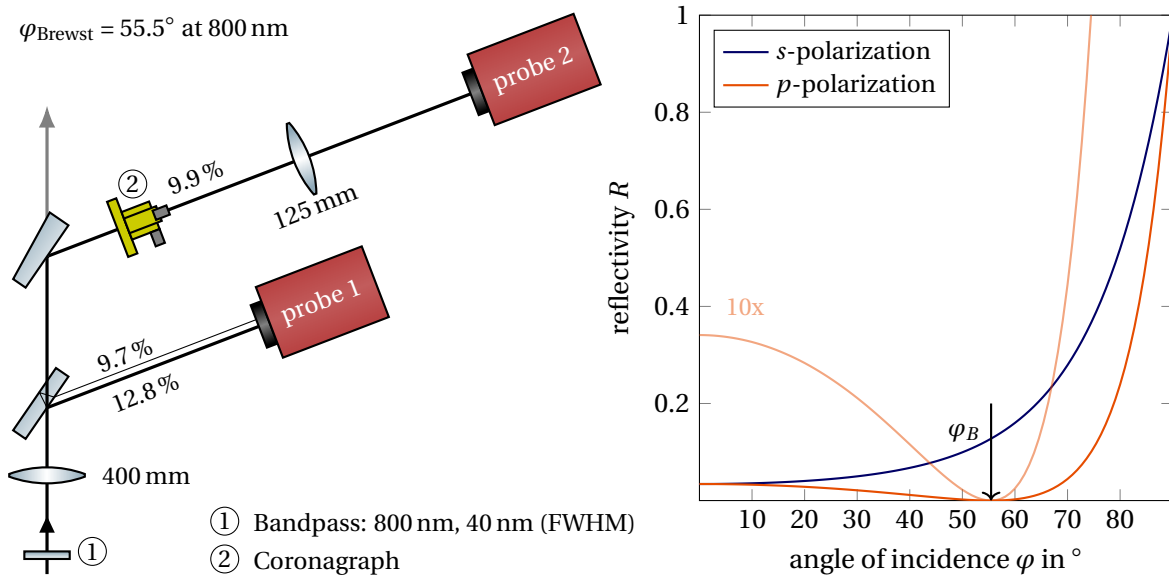


Fig. 3.6: Left: Experimental setup for imaging the droplets with the probe beam. In order to minimize the reflection of the p-polarized pump stray light, the glass plates were inserted in the Brewster angle $\varphi_B = 55.5^\circ$. The reflectivity for s-polarized light was calculated using Fresnel's equations of reflection [47, p.109]. Right: Reflectivity curves of fused silica with $n = 1.453$ at 800 nm [48] for p- and s-polarized light. The light orange curve shows the reflectivity curve magnified by a factor of 10 for p-polarization. At $\varphi = 45^\circ$ the ratio between both polarizations is ten.

used to split up the beam in its Brewster angle $\varphi_B = 55.5^\circ$ (at 800 nm) where the reflection of the p-polarized main laser beam is further suppressed (c. f. figure 3.6 right). In fact, within a tolerance range of $\pm 1^\circ$, the suppression factor of p-polarized light compared to s-polarized light is more than 1000, which is one hundred times larger than in a 45° reflectivity setup. In addition, the reflectivity of the s-polarized probe beam is enhanced compared to 45° reflection. This method successfully avoids the reflection of pump stray light and partially filters the unpolarized plasma emission, while the probe light experiences higher reflectivity. The second beam is again split via a wedged glass plate (5) in order to utilize the zero reflection properties of the Brewster angle for *probe 2*. The wedged geometry is used to prevent the back reflection of the glass plate to enter the imaging setup.

However, the unpolarized part of the plasma emission in the center of the droplet can only be partly reduced by this method. Additionally, the broadband emission of the plasma cannot be completely filtered with a bandpass filter. Nevertheless such a filter was placed in the beam path. This leads to a reasonable intensity contrast between the illuminating probe and the emission of the plasma. Unfortunately, for higher laser energies $E > 10\text{ J}$ on the target, the plasma emission is too strong and may over-saturate the cameras in this setup.

3.3. Plasma emission suppression - the coronagraph

For a successful shadowgraphy probing experiment, the probe pulse should not be outshone by other light sources (e. g. scattered pump light) that mask the information in the shadowgram produced by the probe. However, the interaction of the main pulse with the droplets will lead to a strong emission of electromagnetic radiation from the plasma. One particularly important process in the plasma emission is resonance absorption that leads to the generation of the SH of the main laser pulse [49]. When the plasma reaches its critical density, the frequencies of both electromagnetic wave and plasma oscillation coincide $\omega_0 = \omega_p$. Then the mixing of both waves produces the SH, thus making an off-harmonic probe necessary. Many more processes are involved in the generation of the plasma emission [49, 50], which lead to an unpolarized, broadband emission of the plasma. Therefore, the plasma emission cannot entirely be filtered by a bandpass filter or with polarizers. However, the emission is restricted to the size of the droplet. That bears on the question whether a masking of the central droplet region can be used to suppress or block the observed plasma emission.

3.3.1. Design and implementation

The following setup is based on an idea that was proposed nearly 90 years ago by the French astronomer Bernard Lyot for the observation of the sun's corona without the need of a solar eclipse [51]. He introduced a telescopic attachment, which was designed to block out the direct light from a star with the purpose to resolve nearby objects that would be hidden in the star's bright glare. The design was called a *coronagraph*, which is now adapted to the observation of plasma expansion. When a water droplet is hit by the POLARIS main pulse, the generated plasma will emit intense radiation, which may over-saturate the camera. This renders observations of the plasma expansion around the original position of the water droplet difficult or even impossible. Therefore a setup has been constructed where the center of the droplet will be concealed with a small mask that blocks the intense emission from the plasma. The imaging setup for the coronagraph is shown in figure 3.7.

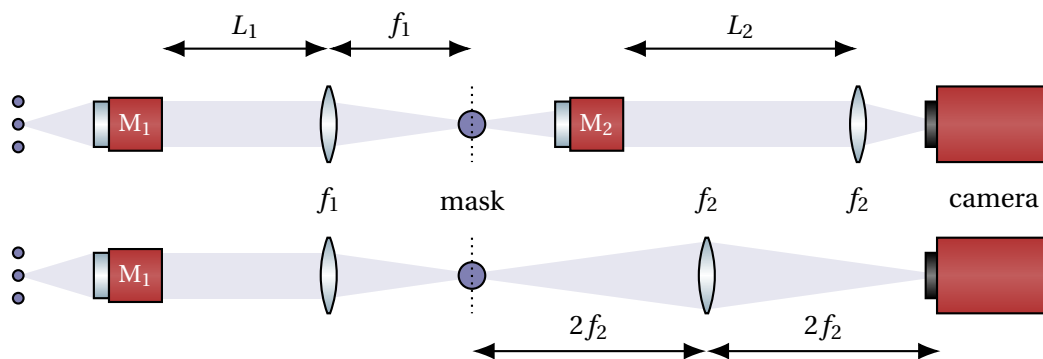


Fig. 3.7: Two different designs for a coronagraph imaging setup. Top: The laser illuminated droplets are magnified and imaged to the position of the coronagraph mask using an aberration corrected microscope objective M_1 and a tube lens with focal length f_1 placed in a distance L_1 to the objective. The droplet with the blocked center is then re-imaged into a camera with another combination of objective and lens f_2 placed in a distance L_2 . Bottom: The second imaging of the droplet into the camera is done by a single lens with a magnification of 1.

3.3 Plasma emission suppression - the coronagraph

Although the light between the objectives M_1 and M_2 is collimated, the lengths L_1 and L_2 cannot be chosen arbitrarily. As sketched in figure 3.8, for a finitely extended object not all light rays leaving the objective will be parallel to the optical axis on their path towards the tube lens. Then the maximum distance of the tube lens is limited by the effective diameter of the microscope objective d_M , the diameter of the tube lens d_1 , the desired size of the image field D (product of the field of view and the magnification factor) and the focal length of the tube lens f_1 as follows [52]

$$L = \frac{d_1 - d_M}{D} f_1 \quad \text{with} \quad d_M = 2N_A f_M. \quad (3.1)$$

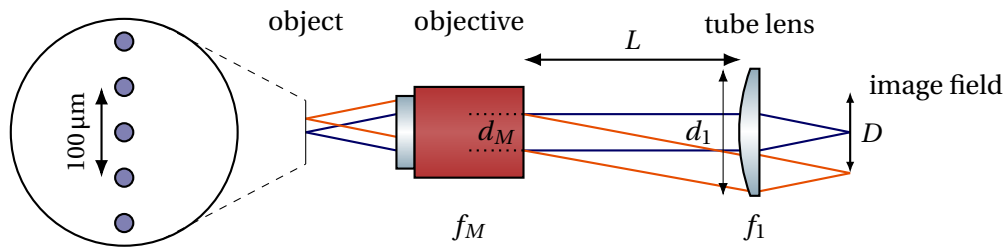


Fig. 3.8: Supplemental drawing for the placement of objective and tube lens. The maximum distance L for a desired image field D can be derived geometrically from the tube lens diameter d_1 and objective aperture d_M . Adapted from [52]. The required field of view with a size of $300\mu\text{m}$ is shown on the left.

For the experiment the desired image field D should cover a field of view that contains at least five droplets ($300\mu\text{m}$), because the expanding droplets may need to be compared to the undisturbed droplets for data evaluation. For a droplet distance of $50\mu\text{m}$ the magnification $M = f_1/f_M$ can be calculated for each objective. With a 3"-diameter tube lens with a focal length $f_1 = 400\text{mm}$, the maximum distance L can be calculated as performed in table 3.1. For the experiment the higher magnification objective *M Plan Apo NIR 10x* was used. The distance between tube lens and objective was $L \approx 2.5\text{m}$, which is within the allowed range. Since the allowed distances between objective and tube lens can be large, this offers the possibility for future experiments to use the first imaging setup shown in figure 3.7 and insert a Mach-Zehnder shearing interferometer into the beam path L_2 to further investigate the density of the plasma [15, p.40]. For the experiments in this thesis, the second imaging setup was used, as it was already indicated in the setup previously described in figure 3.7.

Table 3.1: Maximum distance L (calculated with equation (3.1)) between objective and tube lens for different kinds of objectives used for imaging. The focal length of the tube lens ($d_1 = 7.6\text{cm}$) is $f_1 = 400\text{mm}$. Values taken from [52]. As already shown in figure 3.8, the desired field of view is $300\mu\text{m}$.

Objective	f_M	N_A	M	D	L
M Plan Apo NIR 5x	40 mm	0.14	10	3 mm	< 8.6 m
M Plan Apo NIR 10x	20 mm	0.26	20	6 mm	< 4.3 m

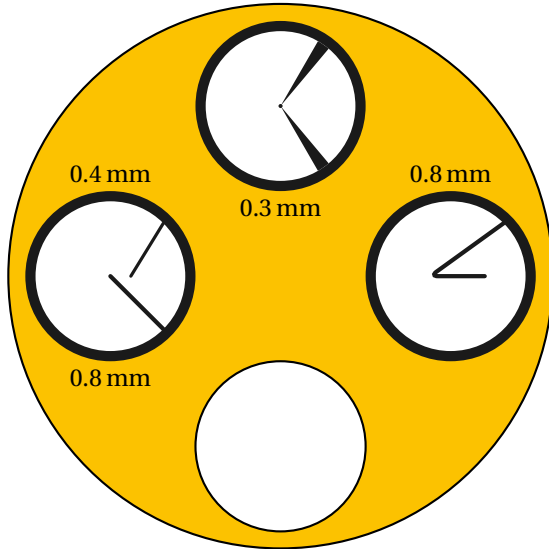


Fig. 3.9: Rotatable brass disc with four holes into each of which Thorlabs filter holders (1" diameter) can be screwed. The holder can then be moved in three directions: along the beam path, vertically and rotationally. The drawing also shows different types of masks that were used in the experiments. The numbers indicate the diameter of the masks.

The design of the coronagraph was inspired by pinholes used in spatial filters (German: Raumfilterblenden) used in [53], where pinholes of different sizes were cut into a rotatable disc that can be inserted into the beam path during the experiment. The current design expands this idea with a disc into which filter holders with appropriate masks (inverse pinholes) can be screwed as displayed in figure 3.9. With the help of a step motor, the filter wheel can be positioned along the beam path. Two additional motors allow the wheel to rotate and move vertically. The coronagraph takes advantage of the fact that the plasma emission as a quasi-point source is also imaged back to a small area by the setup. If an opaque mask is now placed there, the plasma illumination is efficiently suppressed.

3.3.2. Experimental results

In order to verify the utility provided by the coronagraph, a series of images was taken with and without a mask in place to suppress the plasma emission as previously described in figure 3.6. A series of shadowgraphy images were taken in a preliminary experiment on August 19th, 2022 and during the delay scan measurement taken on August 30th, 2022 described in section 3.4. Some exemplary images were chosen to show the difference between the image with and without the mask of the coronagraph in place. They are shown in figure 3.10. It can be seen that the plasma emission was strong enough to cause pixel errors in the picture of *probe 1*, whereas the coronagraph in *probe 2* was able to reduce these effects. For most images taken during the delay scan the performance of the POLARIS main pulses was lower and did not cause significant plasma emission (c. f. figure F2).

Furthermore, in cases where the main laser light was scattered into the probe objective (c. f. figure 3.10 right), a mask with a diameter larger than the droplets was able to diminish the scattered laser light successfully. It should be noted that the last pictures were recorded before the setup with the Brewster angle was introduced. With the Brewster angle setup no over-saturation due to scattered light of the main laser was observed anymore. Therefore

3.3 Plasma emission suppression - the coronagraph

it can be concluded that the Brewster angle setup helps to effectively suppress scattered light from the pump, whereas the coronagraph is able to block the unpolarized, broadband plasma emission.

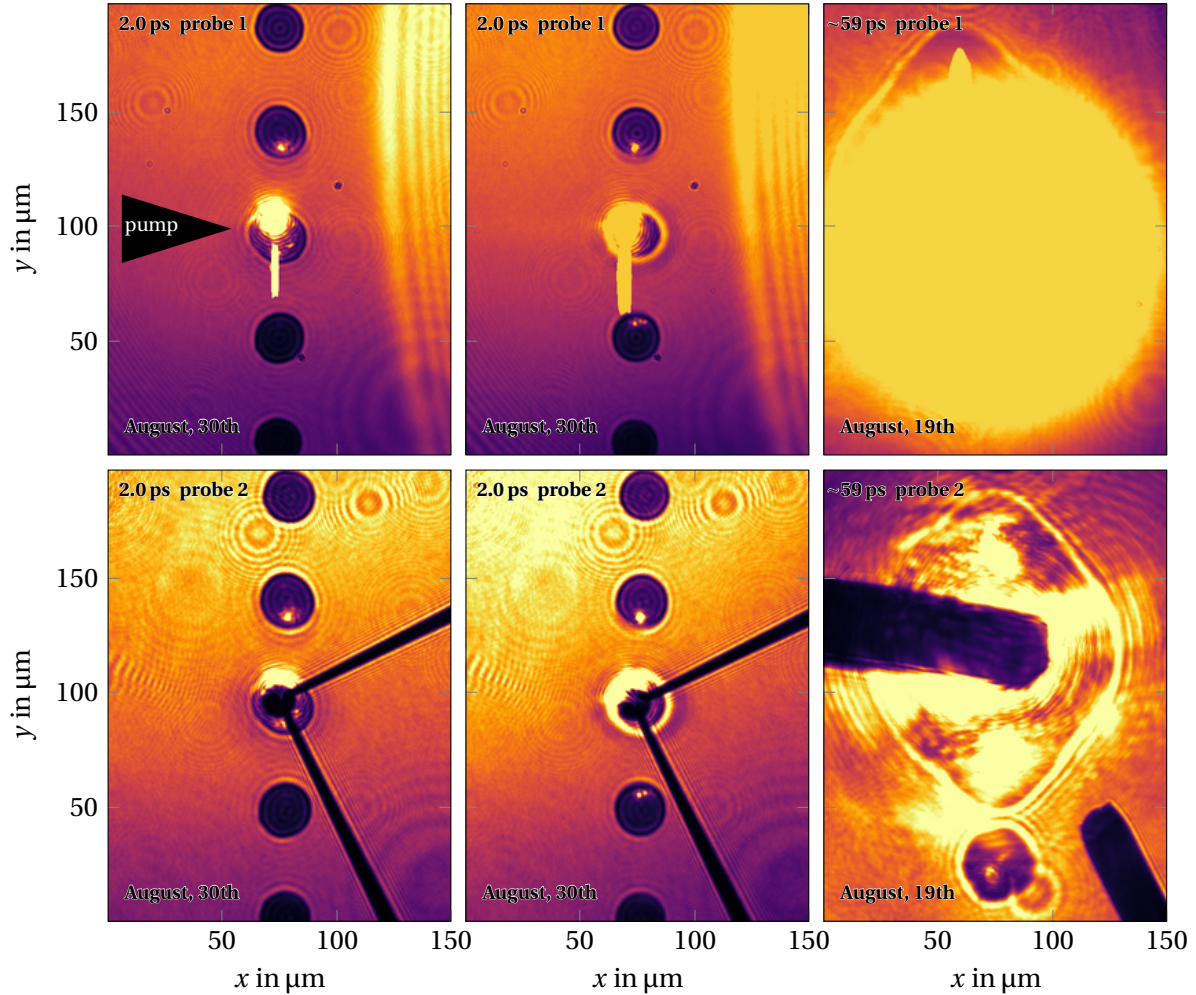


Fig. 3.10: Comparison of the *probe 1* (top) and *probe 2* (bottom) images for different delays between pump and probe pulse. August 30th, 2022: It can be seen that the strong plasma emission over-saturates the *probe 1* camera, which creates pixel errors in the image. In the *probe 2* image, however, the coronagraph could successfully block the plasma and no pixel errors are observed. August 19th, 2022: The plasma emission over-saturates the whole plasma expansion region in *probe 1*. For *probe 2*, a mask of 0.8 mm thickness was used to successfully reduce the strong plasma emission. However, this setup used a polarizing beam splitter cube in front of the camera, which reduced the picture quality.

3.4. Shadowgraphy of the plasma evolution

In this section, we present the experimental results of the laser-matter interaction experiments at POLARIS. The energy of the laser pulses was on average $E = (6.1 \pm 0.9)$ J (on target) with a FWHM pulse duration of $\tau \approx 150$ fs and a focal spot area of about $A \approx 20 \mu\text{m}^2$. This spot contains an energy fraction of $q \approx 0.19$ and is defined as the area, where the laser intensity is larger than the half peak intensity of the beam. For an ideal Gaussian distribution this energy fraction would be $q = 0.5$. These measurements result in an average intensity in the focal region of

$$I_{\text{focal}} = q \frac{E}{\tau A} \approx 4 \cdot 10^{19} \text{ W/cm}^2. \quad (3.2)$$

The temporal evolution of the plasma expansion was observed by changing the delay between pump and probe pulse by moving the delay stage (1) of figure 3.5. The probe pulses generated by the NOPA setup described in section 3.1.1 are used as an off-harmonic illumination under an angle of 90° to the pump laser. The imaging was done using the setup shown in figure 3.7 (bottom) with a single collimating objective and a tube lens. The spatial resolution is limited by the pixel size of the camera chip (Manta MG-032B with pixel size $7.4 \mu\text{m} \times 7.4 \mu\text{m}$) and the resolution of the imaging microscope objective. Here, one pixel corresponds to $0.3 \mu\text{m}$ (magnification factor $M \approx 20$). The resolution of the *M Plan Apo NIR 10x* can be estimated with the Abbe limit as $d = \lambda / (2N_A) = 1.5 \mu\text{m}$ for the probe spectrum centered at 800 nm. The delay between pump and probe pulses can be adjusted in time steps of less than 100 fs, however, the temporal jitter between the probe pulse (which is picked before the first amplifier stage) and the main pulse is estimated to be at least 400 fs [54]. The reduction of the self-emission of the plasma was realized by sufficient spectral filtering with a bandpass filter centered at 800 nm with a spectral bandwidth of 40 nm FWHM. The probe spectrum was adjusted to have the most intense spectral content in this region by varying the non-collinear angle α and by optimizing the temporal delay between WLC and SH (c. f. the method shown in figure 3.4). Typically, spectral bandpass filters have a low damage threshold and should be protected against high fluences [42]. However, the energy of the probe was barely sufficient, such that no additional neutral density filters were placed in front of the bandpass filter. Since the spectral filters narrow the bandwidth of the probe pulse and add additional GVD, the pulse duration will necessarily increase. However, the temporal resolution of the probing method is independent from spectral filtering performed after the interaction [55]. It should be pointed out that the temporal evolution of the plasma expansion can only be reliably recorded under the assumption that the laser-plasma interactions in the different shots are the same or at least sufficiently comparable. If this is no longer the case, the temporal evolution must be recorded in a single shot using appropriate methods such as chirped pulse probing.

Furthermore it is important to note that the probe pulse alone is unable to ionize the water droplets in this setup. Assuming the ideal case of a $20 \mu\text{J}$ probe with $\tau_{\text{FWHM}} = 11$ fs [20] and a collimated beam radius $w = 0.61$ mm ($1/e^2$) as measured in figure 3.3, the maximum

3.4 Shadowgraphy of the plasma evolution

intensity at $\lambda = 800$ nm in the focus of the $f = 400$ mm lens is approximately

$$I_0 \stackrel{(2.12)}{=} E \frac{2}{\tau \pi w_0^2} \sqrt{\frac{4 \ln 2}{\pi}} \approx 1 \cdot 10^{12} \text{ W/cm}^2 \quad \text{with} \quad w_0 \stackrel{(2.10)}{=} \frac{2 \lambda f}{\pi w} = 334 \mu\text{m}. \quad (3.3)$$

For ionization energies of oxygen and hydrogen at $E_{\text{ion}} = 13.6$ eV [56], the OTBI threshold intensity according to equation (2.17) is $I = 137 \cdot 10^{12} \text{ W/cm}^2$, which is way above the maximum achievable intensity with the probe beam. The beam radius w_0 was chosen in such a way that the whole field of view was illuminated. The appropriate choice of w_0 is important to find a good compromise between the plasma self-emission contrast and a large field of view.

3.4.1. Plasma expansion velocity estimation

The whole plasma expansion process was probed in a time interval of $\tau = -4.7$ –258 ps, where τ denotes the temporal delay between pump and probe pulse. For $\tau \geq -1$ ps the coronagraph was inserted to mitigate the plasma self emission. This is shown via a collection of shadowgrams recorded by *probe 2* as depicted in figure 3.11. The corresponding images without coronagraph were recorded by *probe 1*, and are displayed in figure F.2. The individual pump-probe delays for each shadowgram are denoted in the upper left corner of the figure with an uncertainty of ± 1 ps. This is due to an uncertainty in determining the zero delay point and the temporal jitter between pump and probe pulse. Furthermore, over a time period of several hours, the zero delay point between pump and probe pulse drifts up to 2 ps. The main pulse laser energy on target ranged between 3.2–8 J with a mean value of $E = (6.1 \pm 0.9)$ J (standard variation). Since the measurement took place over a time period of three hours, the energy of the NOPA was not stable and its central position moved downwards, which was due to a drift of the amplifier output position. This was compensated for successive experiments with a motorized mirror (c. f. figure 3.5 (2) in front of the target chamber), which can be remotely controlled.

For the absolute time delay of the shots with respect to the peak of the main laser pulse, the ionization of the droplet targets is utilized. For this search, the mask of the coronagraph was removed in order to observe the center of the droplet. Before the main pulse arrives, the droplets are transparent throughout the entire field of view. However, the droplets act like a spherical lens and rays close to the periphery of the droplet get refracted outside of the objective's acceptance aperture (c. f. simulations performed in [57]). The resulting shadow corresponds to the size of the droplet. Probe light close to the center of the droplet is focused and produces a bright spot in the image, which can be seen in figure 3.11 for negative values of the delay τ . In some cases, e. g. at $\tau = -3.9$ ps, a bright spot left to the middle of the target droplet appears, which is not visible in its neighbours. This is due to self emission of the plasma formed in the front of the droplet⁴. The self emission occurs on time

⁴Note that the pump pulse arrives from the left, therefore the front side of the target is left.

3.4 Shadowgraphy of the plasma evolution

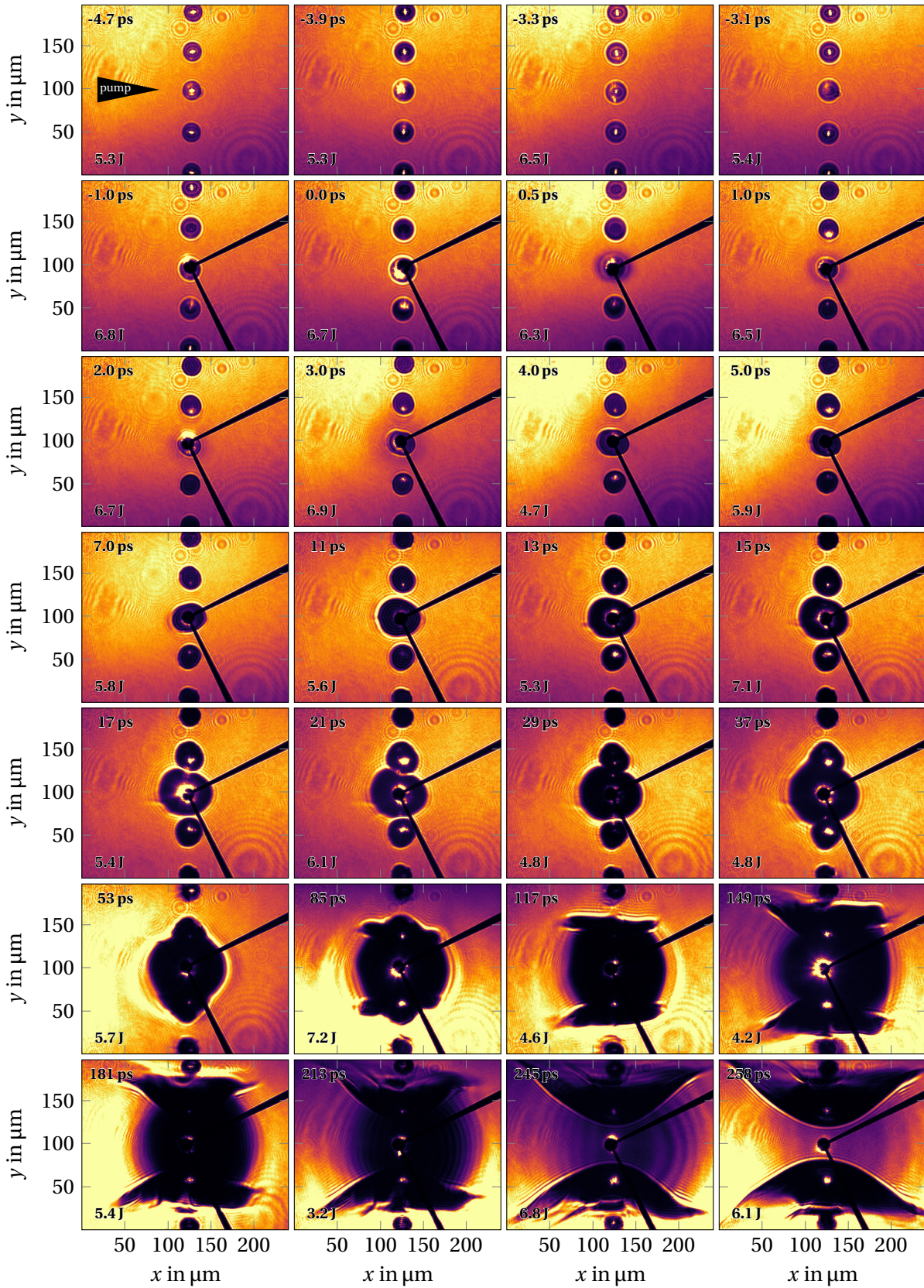


Fig. 3.11: Images of the water droplets recorded with camera *probe 2* and for $\tau \geq -1$ ps with the coronagraph in place. Note that the contrast of the images with shots of lower probe energy was enhanced for better comparison by normalizing the mean pixel value and thus the color scale for all images.

scales orders of magnitude shorter than the integration time (μs scale) of the camera. It is therefore always recorded by the CCD independent on the actual delay between pump and probe pulses. When the rising edge of the main pulse arrives, a blackening of the central droplet can be observed, because the pulse ionizes the droplets and generates a plasma with an electron density, which is higher than the critical density $n_c = 1.74 \cdot 10^{21} / \text{cm}^3$ according to equation (2.27) at 800 nm. Therefore the light is no longer transmitted. At later times, the first and second neighbours of the central droplet start blackening. This point is identified as the *zero delay* point, where the probe pulse and the peak of the main laser pulse coincide. At this point the periphery of the main pulse is still able to ionize the droplets. The outer areas of the focus are much less intense at the periphery than in the centre of the focus, i. e. an ionization process in the neighbouring droplets is triggered only at the time of the peak of the main pulse. Note that this interpretation of the zero delay point is not unambiguous, as the rising edge of the pulse also causes the droplets to become opaque. However, for a *bad* time-intensity contrast of the laser pulse, the ionization of the droplets may occur several hundred femtoseconds or even picoseconds before the arrival of the peak of the laser. Therefore, the determination of the *zero delay* point a few picoseconds after the ionization of the central droplet is justified.

For increased delays between probe and pump pulse (i. e. that the probe arrives later), the spatial extent of the dark volume of overcritical plasma is growing. The created plasma will either lead to absorption of the probe light in the dark region or to reflection or refraction of the probe light out of the aperture of the microscope objective. From the shadowgraphy images alone, the density and extension of the plasma cannot be analyzed thoroughly. However, the expansion of the plasmas critical density can be estimated by measuring the size of the shadow in the pictures shown in figure 3.11. As sketched in figure 3.12, the extension of the front- and rear-side shadow can be measured for each picture.

The error-bars are a result of the limited spatial resolution and faint transition of the shadow into a signal level⁵. The transition is less sharp for higher delays $\tau > 150 \text{ ps}$, which results in larger error-bars. Until $\tau \approx 3 \text{ ps}$ there is barely any expansion visible. Then a rapid growth of the shadow can be observed, where the front expansion distance increases to higher values than the rear radius. For later times the expansion velocity decreases. The respective expansions were linearly fitted, which resulted in a linear expansion velocity for two different ranges of delays:

$$\tau = 3-20 \text{ ps} \quad v_{\text{front}} = (1.27 \pm 0.06) \mu\text{m}/\text{ps}, \quad v_{\text{rear}} = (0.77 \pm 0.05) \mu\text{m}/\text{ps} \quad (3.4)$$

$$\tau = 80-190 \text{ ps} \quad v_{\text{front}} = (0.09 \pm 0.03) \mu\text{m}/\text{ps}, \quad v_{\text{rear}} = (0.22 \pm 0.05) \mu\text{m}/\text{ps}. \quad (3.5)$$

For larger time delays, the relative uncertainty of the expansion velocity is large due to the large error bars of the individual measurements and a small number of data points. Note

⁵The edge of the shadow is determined using the white lineouts as shown in figure 3.12 (top). For small delays the edge between shadow and signal is sharp, whereas for larger delays the shadow border was estimated to be in the center of the slope.

3.4 Shadowgraphy of the plasma evolution

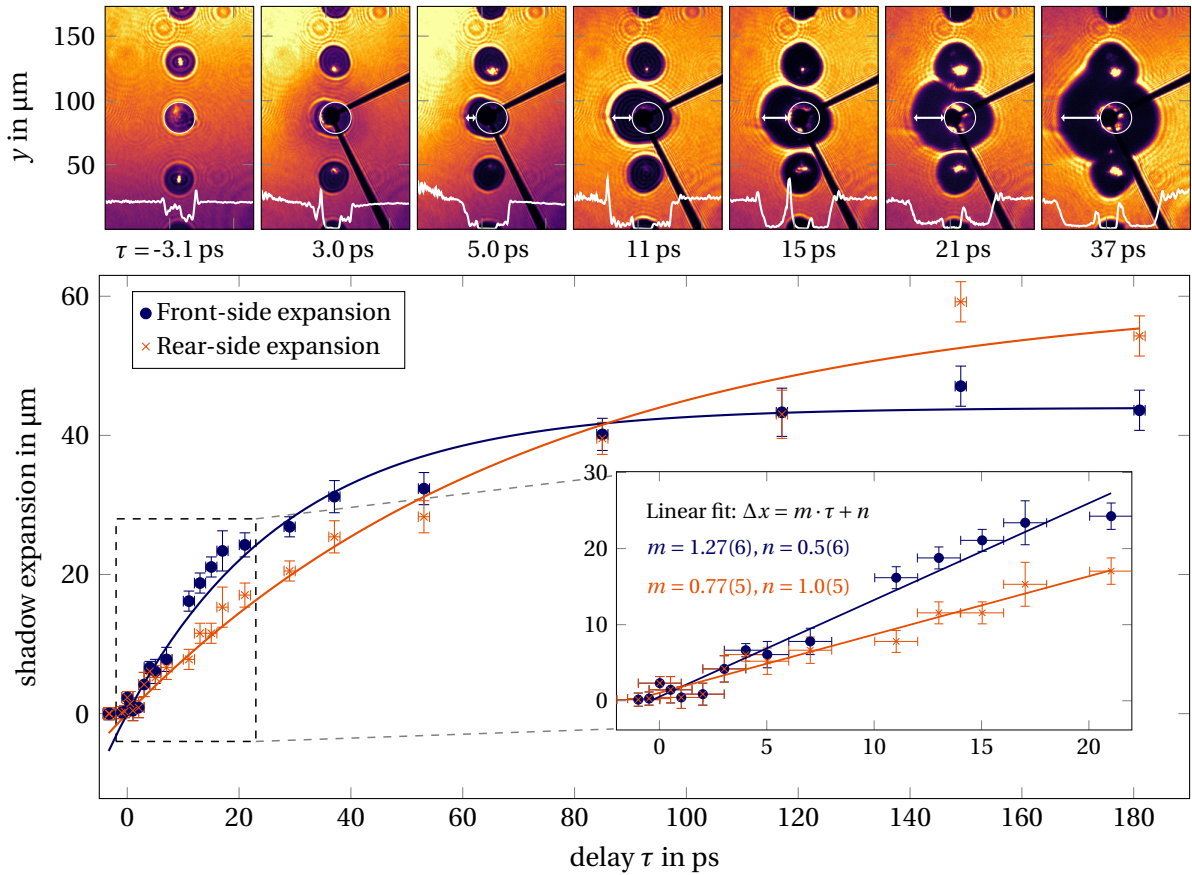


Fig. 3.12: Top: Exemplary images of the plasma expansion for different delays τ . The white circles indicate the original position and size of the central droplet, which was estimated by a comparison to the position of the undisturbed second neighbouring droplets. Furthermore, the coronagraph position can be used as a reference for images between shots to estimate the undisturbed droplet position. For the whole experiment, the droplet chain appeared to be straight and stable. The white arrows denote the measured plasma expansion which was obtained from horizontal lineouts. Bottom: Expansion of the front (blue) and rear (orange) of the plasma parallel to the laser propagation axis plotted as a function of temporal delay $\tau = t - t_0$ of the probe with respect to the main laser pulse at t_0 . The y-axis shows the estimated expansion of the plasma critical density n_c compared to the initial droplet size with a diameter $(23.1 \pm 0.4) \mu\text{m}$. The solid curves are exponential fits to the front and rear-side expansion. Inset: Same image emphasizing the short time scales of $\tau < 20$ ps (dashed rectangle). Here the plasma expansion behaviour is close to linear. Two linear fits were used to determine the plasma expansion velocity of front and rear side.

that for small delays the plasma expansion mainly takes place along the laser axis and is linear. Then the expansion velocity can be compared to the ion sound speed of the plasma. For larger delays the plasma starts to expand spherically outward, which geometrically results in a smaller expansion velocity. Then, the expansion is no longer linear in time. Furthermore, the heating source of the plasma is already gone which further decreases the electron temperature and thus the expansion velocity. For small delays, however, the experimental results are comparable to similar shadowgraphy experiments with liquid targets as shown in table 3.2.

3.4 Shadowgraphy of the plasma evolution

Table 3.2: Comparison of shadowgraphy plasma expansion experiments with targets for different peak intensities. Due to equations (2.21) and (2.22), the relevant parameters determining the plasma expansion are the laser peak intensity and wavelength λ .

experiment	target	intensity	λ	v_{front}
Becker [58, p. 77]	water droplets	10^{16} W/cm ²	800 nm	0.38 $\mu\text{m}/\text{ps}$
This thesis	water droplets	$4 \cdot 10^{19}$ W/cm ²	1030 nm	1.3 $\mu\text{m}/\text{ps}$
Bernert et al. [42]	hydrogen jet	$5.4 \cdot 10^{21}$ W/cm ²	800 nm	23 $\mu\text{m}/\text{ps}$

From the expansion velocity, the ion sound speed can be estimated. Assuming, that eight electrons per water molecule are freed⁶, the maximum electron density is

$$n_{e,0} = 8 \frac{\rho}{M} N_A = 2.7 \cdot 10^{23} \frac{1}{\text{cm}^3} \stackrel{(2.27)}{=} 153 n_{\text{cr}} \quad (\lambda = 0.8 \mu\text{m}), \quad (3.6)$$

where $M = 18.02$ g/mol is the molar mass of water, ρ its density and N_A Avogadro's constant. The front of the expansion x_{front} is assumed to have a density of n_{cr} . Then, using equation (2.21), the ion sound speed of the front can be estimated as

$$n_e(x_{\text{front}}, t) = n_{e0} \exp\left(-\frac{x_{\text{front}}}{c_s t}\right) \Rightarrow c_s = \underbrace{\frac{x_{\text{front}}}{t}}_{v_{\text{front}}} \frac{1}{\ln(153)} = 0.25 \frac{\mu\text{m}}{\text{ps}}. \quad (3.7)$$

This value is much lower than the calculated ion sound speed of protons $c_s \approx 15 \mu\text{m}/\text{ps}$ calculated on page 9 using equation (2.22). For O_6^+ , the ion sound speed is reduced to $c_s \approx 9 \mu\text{m}/\text{ps}$. However, in the estimation the electron thermal energy was calculated for *hot* electrons using the ponderomotive scaling for a relativistic interaction with $k_B T_e \approx 2.4$ MeV. Furthermore, the model of plasma expansion is based an isothermal model of a planar plasma in which the plasma density in the central region stays constant. However, for large time delays $\tau \approx 240$ ps, it can be observed that the target center becomes fully transparent. The transparency indicates that the plasma density n_e has dropped below the critical density n_c due to the plasma expansion into the vacuum [42]. Therefore, during the plasma expansion the electron density $n_{e,0}$ in the droplet center reduces. Then the ion sound speed approaches the value of the expansion velocity and is larger than the initial estimation in equation (3.7). Additionally, with the formation of a pre-plasma by the rising edge of the pulse, the absorption mechanism might be different and thus the electron temperature scaling may change. Moreover, measurements of the hot electron energy distributions in solid targets revealed a resonance absorption scaling of $k_B T \propto (I\lambda^2)^{1/3}$ in a range of $10^{18} - 10^{21}$ W/cm² μm^2 [59, 60]. Then, the calculated ion sound speed would be further reduced.

⁶The OTBI ionization threshold of the last two charge states of oxygen is above 10^{19} W/cm² (c.f. [56] and equation (2.17)) and therefore these two electrons are omitted.

3.4.2. Halo structure around the central droplet

Another effect that has been observed is the formation of a ring-shaped halo around the droplet for time delays between 0.5–3 ps as can be seen in figure 3.11. For larger delays the halo around the droplet vanishes. The effect may be caused by the presence of a low density expanding plasma surrounding the droplet, which absorbs part of the probe light. In comparison with the reference figures E2, it can be seen that the halo appears also on those pictures. To further investigate, whether the halo can be reproduced, an additional measurement was conducted with another target material (c. f. figure 3.13).

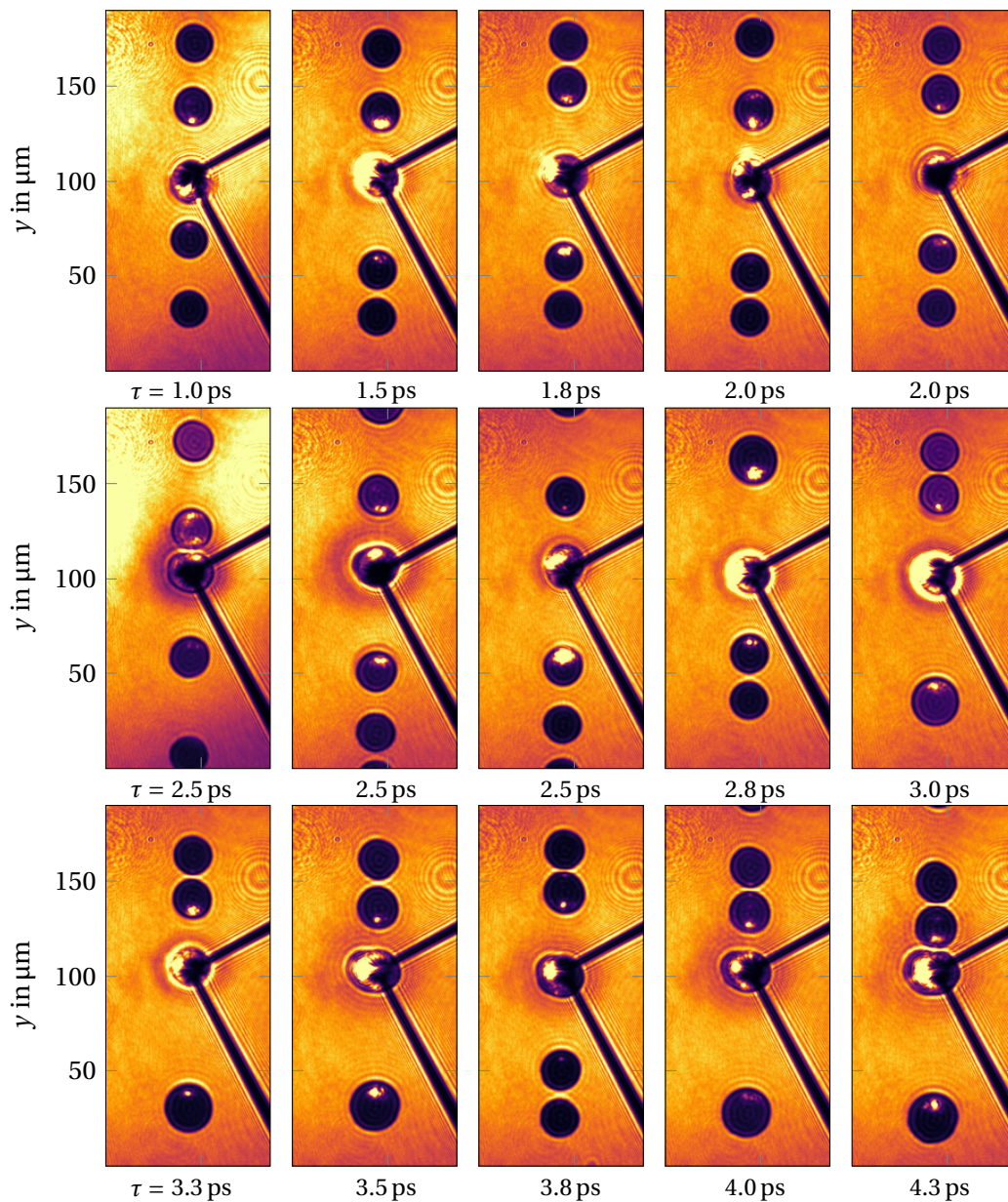


Fig. 3.13: Pump-probe delay measurement with ethylene glycol as a new target material between 1–4.3 ps. The mean pulse energy was $E = (6.8 \pm 1.1)$ J with a pulse duration of $\tau \approx 150$ fs. The delay scan revealed that the shadow around the droplets appears at $\tau = 2$ ps and starts to fade out after $\tau > 4$ ps.

The water was substituted with ethylene glycol, which has a higher viscosity and a much lower vapor pressure $p_{\text{vapor}} = 0.119 \text{ hPa}$ (three orders of magnitude lower than for water) [61]. As a consequence, the droplets will evaporate slower in the high vacuum of the target chamber. Another delay scan was performed in a small range between 1–4.3 ps. The results are shown in figure 3.13.

The figure shows that the effect is not limited to water droplet targets but can be observed in ethylene glycol as well. The fade out of the halo is presumably caused by the expansion of the low density plasma into the vacuum, which further reduces the plasma density and thus absorption and scattering effects. The appearance of the halo might also indicate the arrival of the peak of the main laser pulse, as the estimation of the zero delay considers a blackening of the droplets. This blackening of the central droplet and its first and second neighbours might also be caused by the rising edge of the pulse, which would imply that the main pulse arrives later. The onset of this effect at $\tau = 2 \text{ ps}$, however, offers potential for further investigation.

3.5. Summary and discussion

In this chapter we investigated the laser-matter interaction of the high intensity POLARIS main pulse with peak intensities of $4 \cdot 10^{19} \text{ W/cm}^2$ with water and ethylene glycol microdroplets. The supplied probe pulse was generated by a NOPA system, which produces broad, off-harmonic pulses in the regime of $20 \mu\text{J}$. The optical probe was used to record shadowgraphic images of the droplets to characterize the temporal evolution of the plasma. The probing setup was adjusted to minimize scattering effects and plasma emission on the shadowgraphic images. This was done by first utilizing the Brewster angle to minimize the reflected light from the p-polarized main pulse. Secondly, a coronagraph was employed to suppress the unpolarized plasma expansion originating from the central region of the droplet by blocking the corresponding part in an intermediate image. Then we recorded the plasma expansion in a time interval of up to $\approx 250 \text{ ps}$ after the arrival of the main pulse. The data was analyzed and the front/rear expansion velocities were calculated. Moreover, an interesting effect of a low density plasma surrounding the droplet was observed in a range of delays τ between 2–5.3 ps.

4. SPM-based laser pulse generation

The current method of laser probe pulse generation presented in the previous section uses three nonlinear processes in a complex setup to generate broadband, off-harmonic spectra with pulse energies up to $20\ \mu\text{J}$. In this chapter we investigate other means of generating laser pulses and present a compact, low-cost setup which is less sensitive to precise alignment. Here, self phase modulation (SPM) is successfully employed to generate off-harmonic, optical probe pulses with a broad spectrum of $\Delta\lambda \approx 100\ \text{nm}$ and μJ -level energies.

4.1. Single-pass SPM-based laser pulses

The effect of self phase modulation (SPM) is widely used as a mean of probe pulse generation. For example, the JETI laser system induces SPM-broadened spectra in a gas filled hollow core fiber to generate the probe laser pulse [55]. In this section, a simple low-cost method using femtosecond pulses to generate a broadband probe laser pulse with sufficient energy and suitable wavelength range is sought, which is in contrast to the current NOPA-based setup. The SPM process is induced within thin plastics of thickness $\approx 1.1\ \text{mm}$ with a large nonlinear refractive index. The thickness was chosen in order to mitigate the effects of self-focusing as already discussed in section 2.3.2. Thereby the limitation of the pulse power to values lower than the critical power P_{crit} of self-focusing is overcome in contrast to traditional spectral super broadening typically performed in waveguides [41]. In order to avoid pulse elongation due to GVD of the material, the thickness must be low. Even though the spectral broadening should be proportional to the medium length, it quickly reaches a maximum, since the GVD of the medium for SPM-broadened pulses is large and reduces the pulse peak power, thus reducing the effect of SPM [38]. The most promising material is poly allyl diglycol carbonate (CR-39) with a nonlinear refractive index of $n_2 = 6.24 \cdot 10^{-7}\ \text{cm}^2/\text{GW}$ [37]. Its large nonlinear refractive index and low absorption (0.04 % at 1 mm) [37] across the laser pulse's spectrum are optimal for efficient spectral broadening. The laser pulses used for spectral broadening were generated from a CPA system [62] with a maximum output energy of 4 mJ at a central wavelength of 1030 nm, a bandwidth of $\Delta\lambda = 19\ \text{nm}$ (FWHM) and a pulse length of 130 fs. The experimental setup for SPM generation and characterization is depicted in figure 4.1.

The setup comprises of a Keplerian 3:1 telescope with a focal length of the first lens of $f = 300\ \text{mm}$. Then a 10 % beam splitter sends a part of the pulse to a VIS-NIR spectrometer while the remaining part is transmitted to a chirped mirror pair for pulse compression to the sub-100 fs regime. The pulse duration is then measured in a TOPAG ASF-15 single shot autocorrelator. The pulse compression is important to generate few-cycle optical laser pulses, which can be used to probe the laser-plasma interactions within the time frame of the interaction [55]. Even at low energies $< 0.5\ \text{mJ}$ the laser pulse is sufficient to produce SPM in air without inserting the nonlinear plastic. Therefore a neutral density filter was placed directly after the sample to reduce this effect.

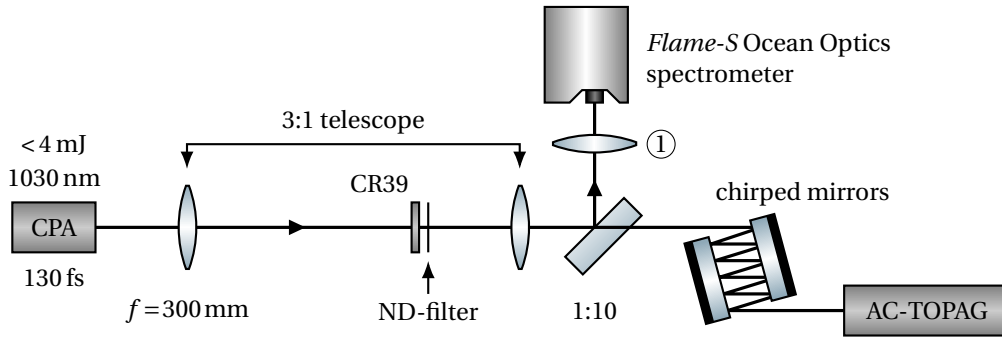


Fig. 4.1: Schematics of the experimental setup with the subsequent pulse compression using a pair of chirped mirrors. First, the pulse passes a lens and the nonlinear CR-39, which is placed near the focus of the lens. Then the intensity of the beam is reduced using a neutral density (ND) filter. The beam is then re-collimated using a second lens of different focal length. Then the beam is split into two parts using a neutral beam splitter. The first part is sent to another weakly focusing lens (1), which is used to collect all light into the spectrometer. The second part is compressed by means of a chirped mirror pair below the original FT pulse length measured by a TOPAG ASF-15 single shot autocorrelator.

Another effect may be the ionization of the air in the laser focus creating a plasma. With a Gaussian intensity profile the plasma will exhibit a higher electron density n_e near the optical axis than on the periphery. According to equation (2.27) this would lead to a refractive index distribution, which acts as a defocusing lens, resulting in the so-called *ionization defocusing* effect. To assess whether ionization effects play a role, first, tunnel ionization (TI) is considered. The tunneling probability according to equation (2.16) at $I = 20 \text{ TW/cm}^2$ is $T \approx 10^{-14}$. Furthermore, the threshold intensity of OTBI can be estimated using equation (2.17) with an ionization energy of nitrogen $E_{\text{ion}} = 14.5 \text{ eV}$ [56]

$$I = 4 \cdot 10^9 \text{ W/cm}^2 \left(\frac{E_{\text{ion}}}{1 \text{ eV}} \right)^4 = 177 \text{ TW/cm}^2. \quad (4.1)$$

This value is much higher than the investigated peak intensity range ($I_0 < 20 \text{ TW/cm}^2$) in this section. Thus, ionization (defocusing) effects in the air can be neglected.

Even though the air is not ionized in the focus, it still acts as a nonlinear medium, which may cause SPM-induced broadening effects at high intensities. For this, an analysis is performed whether SPM of air plays a significant role in the broadening of the spectrum. In fact, a spectral broadening was observed in this setup without a nonlinear plastic placed in the vicinity of the focus in the telescope. The nonlinear index of air is $n_2 = 4 \cdot 10^{-10} \text{ cm}^2/\text{GW}$ [63], which is three orders of magnitude smaller than that for CR-39. The interaction length in air is assumed to be twice the Rayleigh length of the Gaussian beam. The collimated beam radius before the lens was measured to be $w = (1.7 \pm 0.1) \text{ mm}$ (1/e) corresponding to an ideal focal spot size of $w_0 = (57.9 \pm 0.9) \mu\text{m}$ (1/e) according to equation (2.10). Then the Rayleigh length is $z_R = \pi w^2 / \lambda = (1.0 \pm 0.1) \text{ cm}$. The regime at which SPM effects start to play a significant role, is assumed to be at the intensity when the spectrum (FWHM) is broadened by a factor of 1.5. In air this is reached at focal intensities of $I = 38 \text{ TW/cm}^2$. For higher intensities

4.1 Single-pass SPM-based laser pulses

$I = 46 \text{ TW/cm}^2$ the broadening increases to a factor of two. However, spectral modulation already happens at lower intensities.

The choice of suitable lenses for the telescope setup is an important step for recording the spectra successfully. Using shorter focal lengths, the focal spot size is smaller and thus the Rayleigh length z_R shorter (c.f. equation (2.10)). Assuming that unwanted SPM effects in air occur only within the distance of the Rayleigh length to the focus, the interaction length for these effects is reduced. However, the peak intensity is larger in the focus. This means only lower pulse energies can be used in order to prevent ionization of the air in the laser focus. For longer focal lengths, the Rayleigh length is longer but higher pulse energies can be used. After testing several lens setups with focal lengths of the first lens of 100, 300, 450, and 700 mm, it was found that $f = 300 \text{ mm}$ achieves a good compromise between small focal spot size and short Rayleigh length for undesirable SPM effects in air. A detailed discussion of residual nonlinear effects in air is done in the next section.

4.1.1. Spectral measurement

There are two different ways of varying the intensity at the sample's position. In the first approach, the energy is held constant and the distance of the nonlinear plastic sample to the laser focus is changed (c.f. figure 4.2), whereas in the second method the distance of the sample to the laser focus is held constant while the energy of the laser is tuned by inserting different neutral density filters (c.f. figure 4.3).

All recorded spectra were measured by a *Flame-S* Ocean Optics spectrometer and recorded as an average of 30 consecutive shots. Furthermore, the standard deviation was marked us-

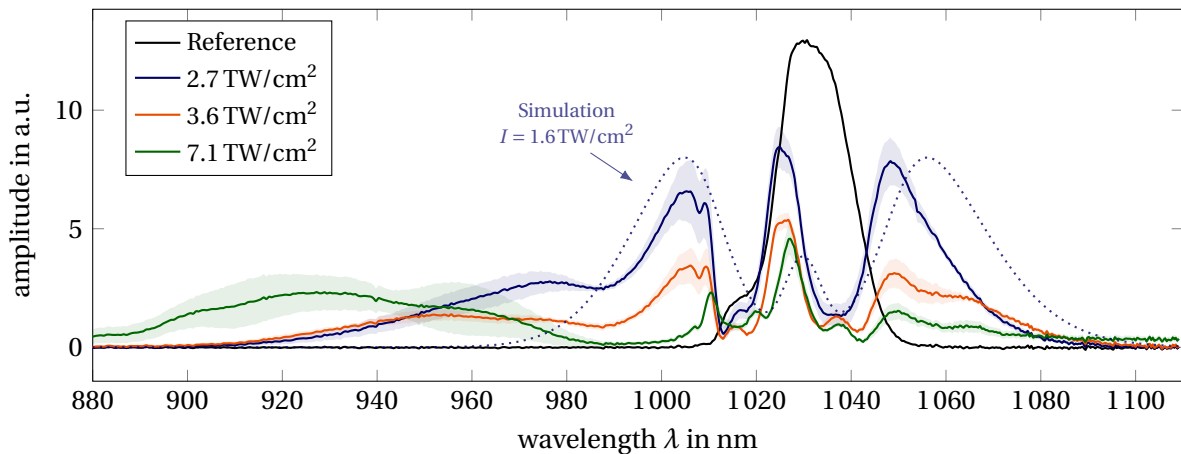


Fig. 4.2: Measurement of SPM-induced spectra in CR-39 for a pulse energy of 0.5 mJ at different intensities by varying the sample distance to the focus position. A reference spectrum in air was taken at a lower pulse energy of 0.1 mJ. The curves show the average spectrum after 30 laser shots. The standard deviation is indicated with the shaded area. The spectrum recorded at 2.7 TW/cm^2 was compared to a simulated spectrum for 1.6 TW/cm^2 calculated using equation (2.41).

4.1 Single-pass SPM-based laser pulses

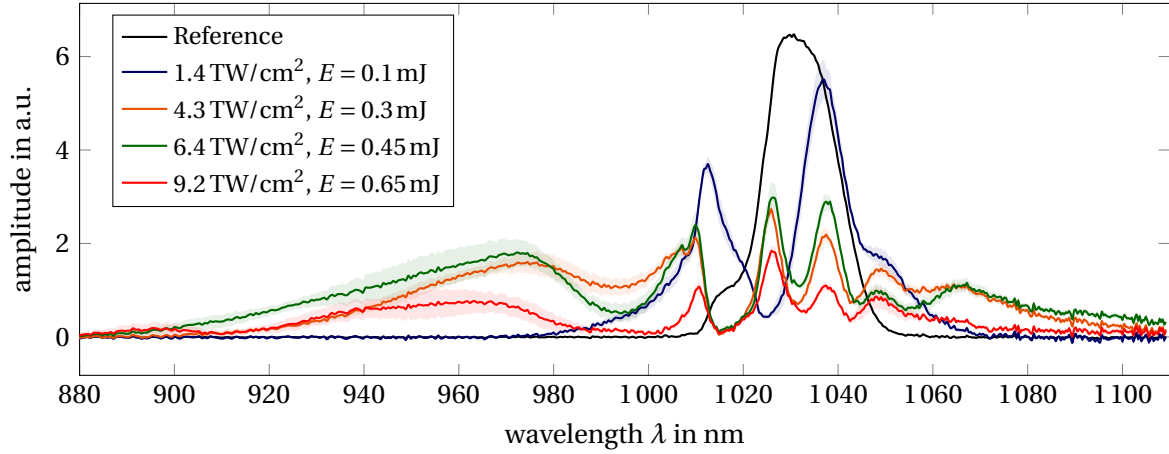


Fig. 4.3: Measurement of SPM-induced spectra in CR-39. Different pulse energies were used at a constant distance (2 cm) to the laser focus. A reference spectrum in air was taken at a lower pulse energy of 0.1 mJ. The height of the spectrum was adjusted for better visualization. The curves show the average spectrum after 30 laser shots. The standard deviation is indicated with the shaded area.

ing a shaded area to check the reproducibility of the generated spectra. The data was calibrated to account for the wavelength dependent spectral sensitivity of the CCD sensor (c. f. appendix E). The shot-to-shot variations of the signal are due to the fluctuation of the CPA-amplified pulse whose shot-to-shot energy changes are limited to $\pm 10\%$ and an average of $\pm 5\%$ as described in [62]. Compared to the CPA setup used in section 3.1.1, the fluctuations are larger. The energy was measured using the *QE12HR-S-MB* pyroelectric energy detector from Gentec-EO with a calibration uncertainty of 3%. The intensities stated were calculated using equation (2.12) and (2.8) with the focal spot size w_0 calculated previously and a measured pulse duration of $\tau = (130 \pm 2)$ fs. The largest uncertainty in determining the laser peak intensity is the measurement of the distance to the laser focus with $\Delta z = \pm 2$ mm in order to estimate the beam radius in the interaction plane using equation (2.8). The relative error of the beam radius measurement is

$$\frac{\Delta w}{w} = \frac{\Delta z}{w} \left| \frac{\partial w}{\partial z} \right| + \frac{\Delta z_R}{w} \left| \frac{\partial w}{\partial z_R} \right| \stackrel{(2.8)}{=} \left(\frac{\Delta z}{z} + \frac{\Delta z_R}{z_R} \right) \frac{1}{1 + \left(\frac{z_R}{z} \right)^2} \stackrel{z=2\text{cm}}{=} 16\%. \quad (4.2)$$

Combining all errors results in a large uncertainty for the intensity estimation

$$\frac{\Delta I_0}{I_0} = \frac{\Delta E}{E} + \frac{\Delta \tau}{\tau} + 2 \frac{\Delta w}{w} = 47\%. \quad (4.3)$$

The factor of two for the beam radius uncertainty arises due to a quadratic dependence in the calculation of the intensity. It can be expected, that the calculation overestimates the intensity, as the estimation of the beam radius assumes a diffraction-limited beam diameter of an ideal Gaussian beam. This can be seen by comparing the measured spectra with a simulation as indicated in figure 4.2. Here, the simulated pulse broadening appears to be larger than in the experiment. Two reasons may explain this behavior: First, the effect of dispersion

was neglected in the simple description of SPM, because the nonlinear interaction length is small. However, group velocity dispersion (GVD) of the medium still temporally broadens the pulse, which reduces the peak intensity. This leads to a weaker spectral broadening. Secondly it has been shown, that an initial positive chirp of the pulse also decreases the spectral broadening [39, p. 1685]. Later, characterization of the CPA-amplified pulses showed, that the pulse length of $\tau = 130$ fs used in this experiment could be reduced to 120 fs by decreasing the distance of the compressor gratings in the preceding CPA-system. This indicates an initial positive chirp, which may then inevitably reduce the SPM-induced broadening.

It can be seen in the figures (4.2 and 4.3) that the simple model of SPM (c.f. figure 2.6) does not successfully represent the observations made in the experiment. At low intensities ($I = 2.7 \text{ TW/cm}^2$) the form of the spectrum is still comparable to the theoretical calculations made in figure 2.6. However, for larger intensities the observed spectra become asymmetric and a super-broadening is observed as can be seen for the green curve in figure 4.2. The super-broadening shifts to lower wavelengths for higher peak intensities of the laser pulse in the nonlinear plastic. This asymmetric broadening was first observed by Fork et al. [64] in 1983. They used an 80 fs pulse at 627 nm focused to an intensity of 10^{13} W/cm^2 on a 0.5 mm film of ethylene glycol. They suggested that the asymmetry of the spectral broadening can be explained with the change of the temporal pulse shape as the pulse travels through the medium. This effect will be investigated in section 4.3. Furthermore, they assumed that the extremely large broadening is caused by additional mechanisms such as four-photon parametric mixing.

As discussed in section 2.3.2, the self-focusing distance increases for larger pulse energies at constant intensities (c.f. table 2.1). Therefore, the second method is preferable and used exclusively in more sophisticated measurements in this section. In addition, the uncertainty in the determination of the intensity is smaller, as the beam radius in the plastic is held constant. Figure 4.3 indicates that stronger absorption occurs at higher energies because the spectral amplitude decreases for higher energies. However, with this setup it is not feasible to determine if absorption is caused by ionization of air in the focus, by intensity-dependent absorption of the CR-39 or by intensity-dependent absorption of the “*neutral*” density filter.

Spectral measurement at low pressure

To rule out the possible effects that may have been caused by the ND-filter and the focus in air, a vacuum chamber was installed in the measurement setup in which the CR-39 sample is placed. The schematic setup is shown in figure 4.4. Due to the geometry of the vacuum chamber, a different combination of lenses was used. The vacuum chamber allows a reduction of the pressure to 5 mbar. First, a reference measurement was performed at a high peak intensity of 33 TW/cm^2 (c.f. figure 4.4 right). The spectrum was measured without sample in air and at low pressure. Indeed, the SPM in the laser focus can be reduced in this configuration. However, the spectrum still shows a deformation at low pressures.

4.1 Single-pass SPM-based laser pulses

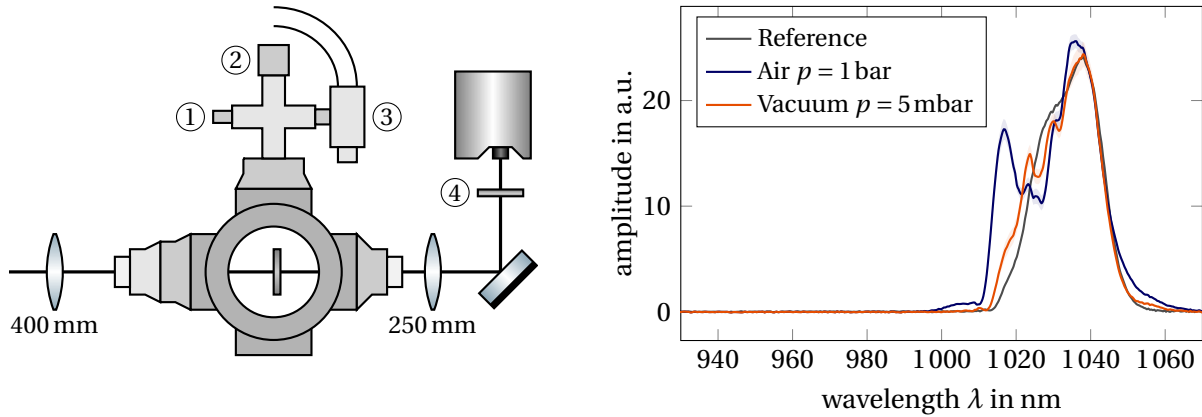


Fig. 4.4: Left: Geometry of the setup for repeating the measurements in vacuum. (1) Balancing valve, (2) pressure gauge, (3) valve to vacuum pump, (4) spectral short-pass filter used for the measurement in figure 4.6. Right: Comparison of the laser spectrum (without nonlinear material) for a peak intensity $I = 32.9 \text{ TW/cm}^2$ at a pulse energy of $E = 0.85 \text{ mJ}$ in air and at $p = 5 \text{ mbar}$ compared to a reference measurement (black) without focusing the pulse.

The spectral broadening measurements in CR-39 were repeated for the new setup. This is shown in figure 4.5. For this, the pulse energy was increased in analogy to figure 4.3 at constant distance (2 cm) to the laser focus. In contrast to the previous measurement (c. f. figure 4.3), less absorption is observed at higher energies. The typical spectral broadening with the formation of a spectral dip at the central wavelength (which was also observed in [37] for lower pulse energies) also remains at higher intensities. This effect is also not included in the simple SPM model, because there, the spectral maximum shifts symmetrically away from the central wavelength (c. f. figure 2.6). A possible explanation for this effect is the transverse Gaussian profile of the beam. Not only the part on the beam axis contributes to the total

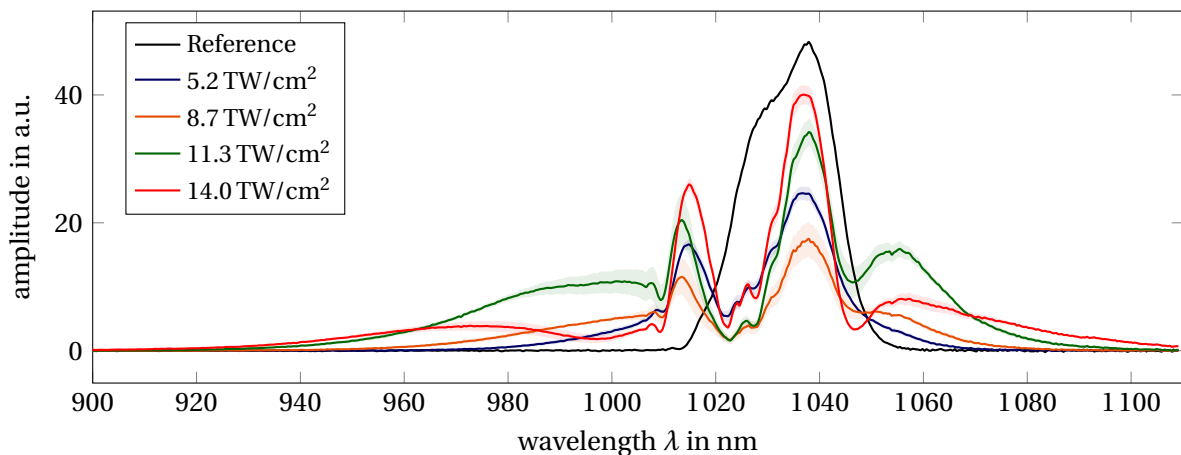


Fig. 4.5: Measurement of SPM in CR-39 performed at low pressure (5 mbar). Different pulse energies were used at a constant distance (2 cm) to the laser focus (focusing lens $f = 400 \text{ mm}$). A reference spectrum was taken at a lower pulse energy of 0.1 mJ. The amplitude of the spectrum was adjusted for better visualization. The curves show the average spectrum after 30 laser shots and the standard deviation within the shaded area.

4.1 Single-pass SPM-based laser pulses

spectrum, but also the outer areas of lower intensity. This leads to a superposition of spectral components generated by lower intensity parts of the laser pulse. This consideration is investigated in detail in section 4.3.

To determine the fraction of the super-broadened spectrum, another measurement was performed with a spectral short-pass filter with a cut-off wavelength of 1010 nm placed in front of the spectrometer (see figure 4.6). Then, the SPM-induced spectra and the corresponding pulse energies of the filtered pulses were measured by a pyroelectric energy detector. As expected, the spectrum shows a blue shift for higher peak intensities. In addition, the remaining pulse energy also increases. However, the generated spectra are unstable, as can be seen from the large shaded areas visualizing the standard deviation. For the measurement with an input energy of 1.45 mJ, the spectrum collapsed after less than sixty consecutive shots. In this case, the sample of CR-39 was permanently damaged and had to be moved to a different position for further measurements. This means that for intensities greater than 20 TW/cm^2 , appreciable multi-photon absorption or optical breakdown occurs. Therefore, the highest stable energy of the super-broadened pulse is about $45 \mu\text{J}$.

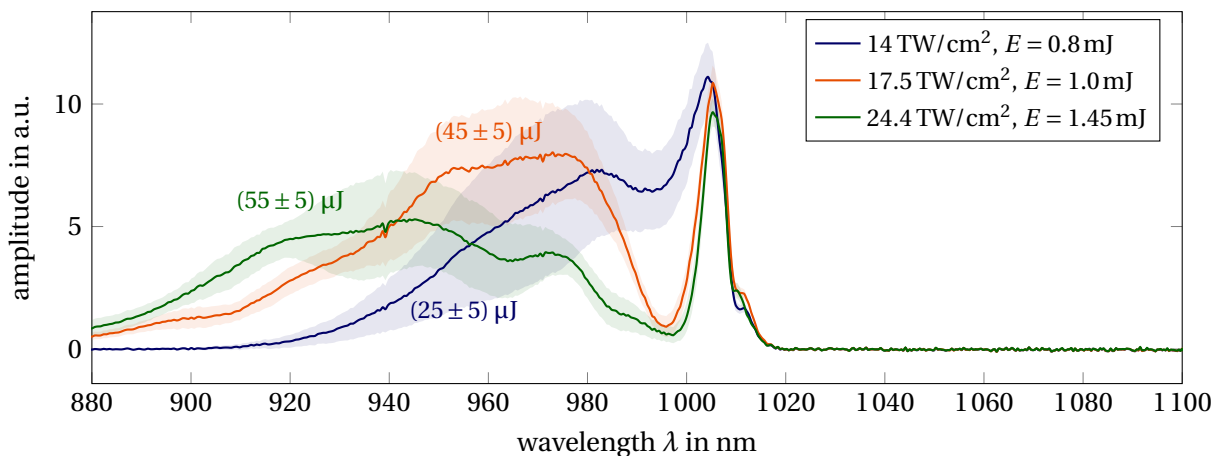


Fig. 4.6: Measurement of SPM in CR-39 performed at low pressure (5 mbar) with a short-pass filter cutting at 1010 nm. Different input pulse energies were used with a constant distance of the sample (2 cm) to the laser focus (focusing lens $f = 400 \text{ mm}$). Furthermore the energies of the filtered pulses were measured by a *QE12HR-S-MB* energy detector. The curves show the average spectrum after 30 laser shots and the standard deviation within the shaded area.

4.1.2. Compression of laser pulses

For most probing experiments, it is not only important that the probe pulse has been spectrally broadened in order to have spectral intensity far from the fundamental wavelength of the main laser system (1030 nm) and its second harmonic (SH). For experiments where a high temporal resolution is required, it is also important to control the temporal profile of the probe pulse. Furthermore, the development of few-cycle optical probe pulses is particularly interesting to increase the spatio-temporal resolution of pump-probe experiments,

which investigate the evolution of the plasma density distribution on very short time scales. So far this has been successfully achieved by using SPM in a hollow core fiber (HCF) filled with rare gases at the JETI laser system [55]. Therefore, we will investigate the possibility to generate ultrashort SPM-induced pulses in thin solid material with subsequent dispersion control using chirped mirrors.

For this purpose the spectral measurement and an autocorrelation measurement were recorded simultaneously with the pulses being reflected several times off a pair of chirped mirrors for pulse compression (c.f. figure 4.1). The pulse compression is realized by the design of the chirped mirrors, where lower wavelengths are reflected at deeper positions inside the coating of the chirped mirrors. This introduces a negative group delay dispersion (GDD), which compensates the positive chirp of frequencies induced by SPM. The chirped mirrors were mounted onto a rotation and translation stage. This allowed for an online adjustment of the amount of negative GDD added to the pulse by changing the number of bounces between both mirrors. A measurement of spectral broadening (see figure 4.7 top) and an autocorrelation trace after six bounces on the chirped mirrors is shown in figure 4.7 (bottom).

For the SPM signal the pulse shape is not Gaussian anymore but has a more complex shape. The corresponding autocorrelation signal exhibits side lobes with a narrow central peak. Due to the complex shape of the autocorrelation signal, the pulse duration cannot be determined via a Gaussian fit. The broad autocorrelation trace indicates that the pulse length is in the range of 100–200 fs. A more sophisticated measurement of τ would require more advanced correlation methods like frequency resolved optical gating (FROG), which is suited to measure complex ultrashort pulses and has reliable checks on the measurement itself [65].

For adequately short propagation distances in the non-linear medium, it was already shown in section 2.3.2 that strong self-focusing in the medium can be avoided. However, the Kerr lens effect causes an inhomogeneous spectral broadening over the beam profile, which results in poor compressibility [41]. Furthermore, the Kerr lens varies corresponding to the temporal pulse envelope and thus the spectral broadening changes accordingly. These may induce the poor autocorrelation trace obtained in figure 4.7. This could be partly recovered by spatial filtering of a small beam section, which involves considerable losses [66].

4.1 Single-pass SPM-based laser pulses

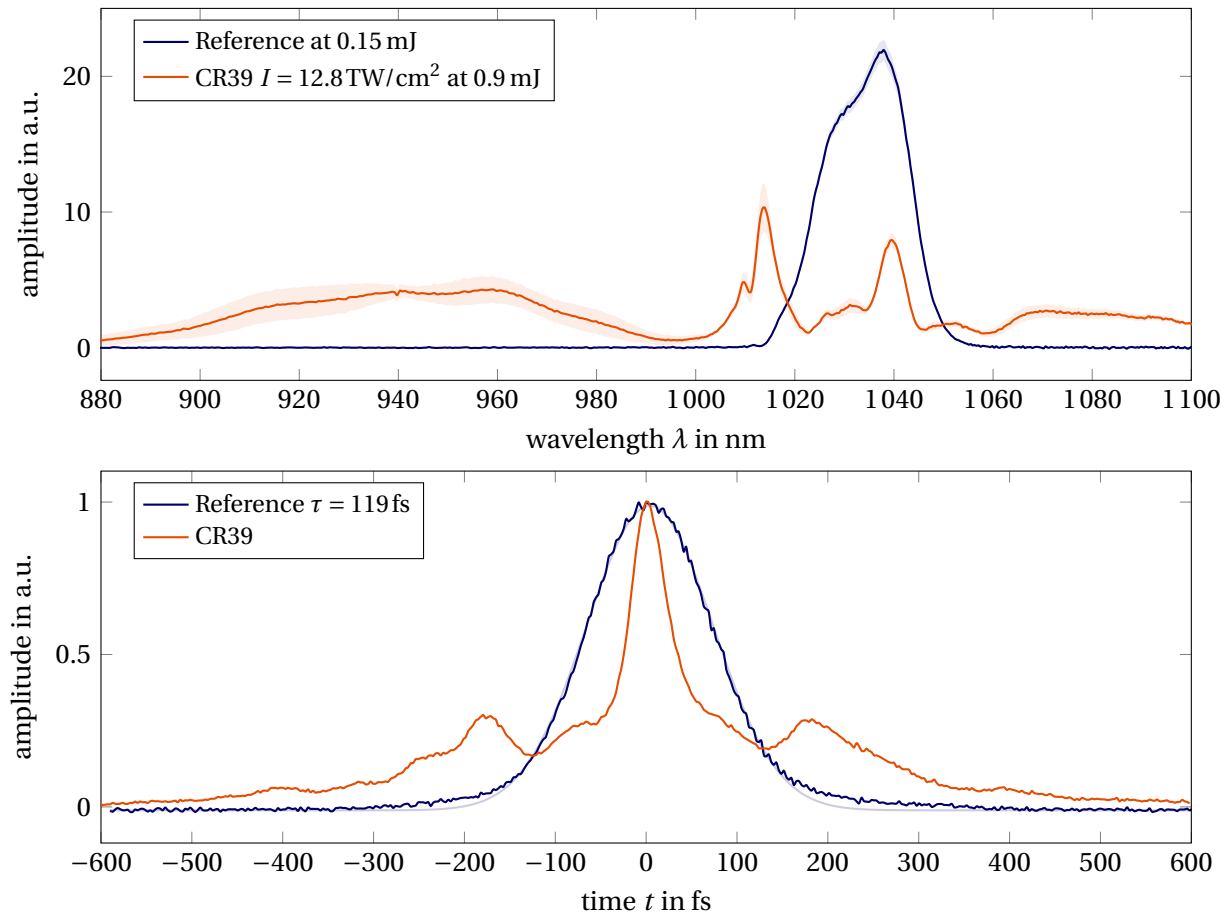


Fig. 4.7: Top: Spectra of a reference pulse (blue) and for pulses experiencing SPM in CR-39 (orange) recorded simultaneously with an autocorrelation measurement. The spectra are averaged over 30 shots with the standard deviation indicated with the shaded area. Bottom: Measured Autocorrelation functions for a reference pulse (blue) at 0.15 mJ. Here a pulse length of $\tau = 120 \text{ fs}$ (FWHM) was determined with a Gaussian fit. The second autocorrelation function (orange) corresponds to the measurement of SPM-induced broadened pulses in CR-39.

4.2. Multi-pass SPM-based laser pulses

The previous method of spectral broadening in a laser pulse utilized a nonlinear material in which SPM is induced in a single pass. However, the same nonlinear phase Φ_{NL} may be accumulated by passing through the medium several times at lower intensities. This has the advantage that less absorption takes place and optical breakdown does not occur.

The idea of the following setup is that the laser pulses are sent into an optical arrangement in which they propagate alternately through the nonlinear medium and a medium with weak nonlinearity (air) in order to prevent self-focusing effects. Thus the propagation through the medium (of thickness d) a number of times N is different from the single propagation through a nonlinear medium of same effective length $N \cdot d$.

A compact multi-pass configuration was already designed by Issa Tamer [19] with the aim to transform femtosecond laser pulses into few-cycle probes for laser-plasma interactions. The design involves a Herriott cell, which is depicted in figure 4.8. It consists of two curved mirrors of focal lengths $f = 100$ mm and two chirped mirrors built in a compact folded configuration. The nonlinear plastic can be inserted into the Herriott cell and in combination with the chirped mirrors used for spectral broadening and pulse compression. The incorporation

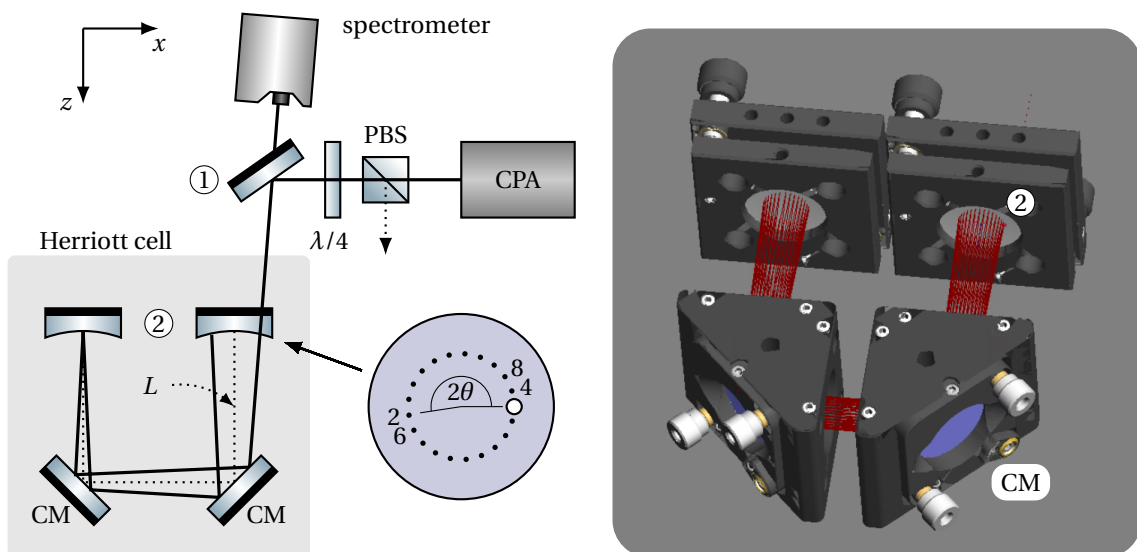


Fig. 4.8: Left: Setup using a nonlinear plastic in a multi-pass Herriott cell with two curved mirrors (2) and chirped mirrors (CM). The chirped mirrors in the beam path compensate for temporal pulse broadening due to the large GVD of the nonlinear sample for the broadened pulses and thus prevent the reduction of peak intensity. The experimental setup (left) consists of a polarizing beam splitter (PBS) and a quarter wave plate, which are used for the initial alignment of the setup. A D-cut mirror (1) is used for decoupling the exiting beam into a spectrometer. Right: The trace of a single light ray was simulated using FRED[®] by Photon Engineering. The raytracing model shows that the input pulse exits the device after a specific number of passes, which is determined by the ratio of the distance of the curved mirrors and their focal length. Furthermore, the diameter of 1" does not lead to clipping on the mirror edges. The beam path length between the curved mirrors was chosen to be $L = 21$ cm.

of chirped mirrors in the resonator has the advantage that the pulse is already compressed during the individual round trips, which ensures a high peak intensity.

The beam path in such a resonator-like setup was first described by Herriott et al. in 1964 [67]. Repeated reflections of the rays trace a path on a hyperboloid surface. On the mirrors, the points of reflections trace circles if the input angles to the xz - and yz -plane are the same (assuming the z -axis being the symmetry axis of the mirror). The angle difference θ between two consecutive reflections (c. f. figure 4.8) is given by [67]

$$\cos(\theta) = 1 - \frac{L}{2f}, \quad (4.4)$$

where L is the distance between both curved mirrors. In fact, the path will only be perfectly retraced when $\nu \cdot 2\theta = 2\pi$ for an integer value of ν . Here, ν is the number of return trips to the input mirror in the resonator. For a confocal setup $L = 2f$, the rays arrive at their entrance point after two return trips ($\nu = 2$). If, however, the resonator setup is slightly longer, the beam will not exactly retrace its path and the fourth reflection in the resonator setup will be above the entrance hole. This is shown in figure 4.8 for a mirror distance of $L = 210$ mm which is longer than the confocal setup with $L = 200$ mm. The input angle φ of the beam with respect to the z -axis for a desired circle of radius $R = 7$ mm (distance of the entrance hole to the mirror center) is given by [67]

$$\varphi = \frac{R}{\sqrt{f \cdot L}} \approx 0.048 = 2.77^\circ. \quad (4.5)$$

Then the angles of the beam to the xz - and yz -plane should be around 2° each, which was chosen for the FRED simulation in figure 4.8 (right).

The alignment of the folded cell is not trivial, since eight degrees of freedom arise due to the four mirrors installed in the setup. The initial alignment can be done with the aid of a quarter wave plate and a polarizing beam splitter (PBS) at the entrance of the setup, which is shown in 4.8 (left). If the initial angle to the xz -plane is zero and the cell is properly aligned, the output beam will retrace the input beam path perfectly and exit the setup after a single reflection on the entrance mirror. The initially horizontally polarized light will be rotated by 90° after a double pass through the quarter wave plate ($\lambda/4$), which then acts as a half wave plate (HWP). Then the beam will be detectable at the second output of the PBS (dotted arrow in figure 4.8). If then a tilt to the xz -plane is introduced via mirror (1), the output beam exits the setup (after 20 reflections on the entrance mirror) under another angle above the D-cut mirror into a spectrometer.

Another issue that generally needs to be considered is mode-matching to the resonator mode of the Herriott cell. Typically the input beam should have a matching beam radius and curvature to preserve the Gaussian beam q -parameter after one full pass [68]. Typically the mode matching is performed via a Gallilean telescope to ensure identical beam properties per pass [69]. The desired beam radius can be calculated using the geometry of the resonator

setup. Assuming that in a stable setup the radius of curvature (ROC) of the beam caustic (on the mirror surface) should match the ROC of the spherical mirrors R , the waist radius ($1/e$) of a symmetric resonator setup is given by [70, sec. 5.1.3]

$$w_0 = \sqrt{\frac{\lambda}{2\pi} \sqrt{L(2R - L)}}. \quad (4.6)$$

The waist radius for different setups of Herriott cells with integer fractions of $\nu = \pi/\theta$ is given in table 4.1. The table shows that for a higher number of return trips the radius of the beam waist shrinks and for a fixed input energy, the peak intensity increases. However, the fluence on the mirror surface exceeds the typical laser induced damage threshold (LIDT) of gold coated mirrors [71]. Therefore the method of a slight detuning of the mirror distance as previously described is more appropriate, since a high number of passes can be achieved without the risk of damaging the mirrors.

Table 4.1: Waist radius w_0 (4.6) and beam radius w on the spherical mirrors (calculated with (2.8) using $f = 100$ mm) for different possible types of Herriott cells. The peak intensity in the laser focus is given for $E = 1$ mJ (130 fs FWHM). The ratio f/L can be obtained by solving equation (4.4) for a value of $\theta = \pi/\nu$. The fluence F on the mirror surfaces is also given.

no. of return trips ν	2	3	4	6	12
f/L ratio	0.5	1	1.7	3.7	14.7
w_0 in μm	181	168	152	128	92
$w(L/2)$ in μm	256	195	165	132	93
I_0 in TW/cm^2	7.02	8.10	9.90	13.98	27.13
F in J/cm^2	0.49	0.84	1.17	1.80	3.69

4.2.1. Experimental setup

In the previously introduced setup of a folded Herriott cell (c.f. figure 4.8), it was not possible to extract more than 5% of the input energy. For a total of 41 reflections in the setup the absorption on the slightly tarnished curved mirrors was just too high. For this reason the setup was simplified by unfolding the Herriott cell and removing the chirped mirrors as shown in figure 4.9. Furthermore, the mirror distance was changed from $L = 21.5$ cm to $L = 10$ cm, which corresponds to three return trips. According to table 4.1 the beam radius on the mirror should be about $195 \mu\text{m}$. This was achieved using a 10:1 Galilean telescope placed in front of mirror (1). In order to increase the spectral broadening, two samples of CR-39 were placed in the middle of the cell with a distance of about 2 cm in order to avoid nonlinear self-focusing effects. Both samples were inserted under their Brewster angle φ_B ($n = 1.495$ [19]) in order to suppress reflection of the p-polarized light. It is given as

$$\varphi_B = \arctan\left(\frac{n}{n_{\text{air}}}\right) = 56.2^\circ. \quad (4.7)$$

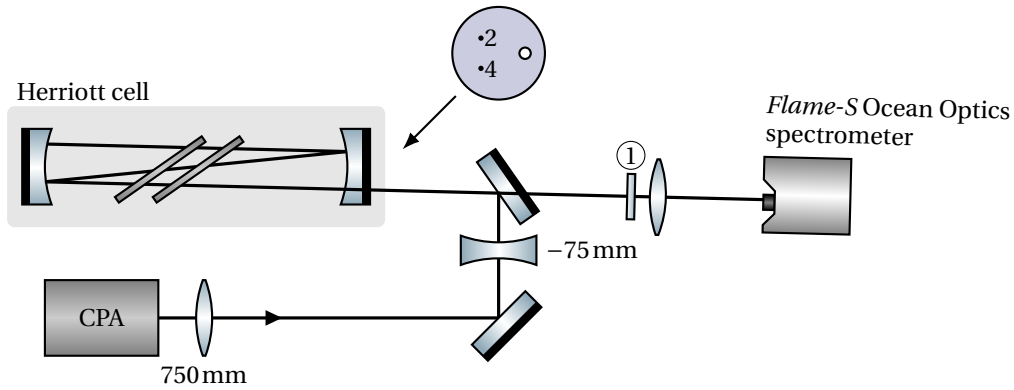


Fig. 4.9: Schematics of the simplified experimental setup. The two nonlinear samples of CR-39 are placed under the Brewster angle into the Herriott cell to mitigate reflection losses. This configuration with three return trips ($\nu = 3$) allows a total of twelve passes through the nonlinear medium. Furthermore, the mode of the Gaussian beam is matched via a 10:1 telescope. The spectrum is then measured once with and without a spectral short-pass filter (1) with cutoff wavelength 1010 nm.

4.2.2. Spectral characterization

The input energy from the CPA-system was varied and the resulting spectra were recorded as depicted in figure 4.10. It can be seen that considerable pulse broadening can be achieved. Although the number of passes through a sheet of CR-39 is much higher than before, this broadening is comparable to the measured spectra in the previous section. This is due to a reduced peak intensity caused by a larger radius of the unfocused beam and the temporal stretching (due to the lack of the chirped mirrors). However, the plotted standard deviation for a series of 30 shots reveals that the energy in the broadened signal varies. The two spectral contributions, which are found to be symmetrical 15 nm away from 1030 nm, show the

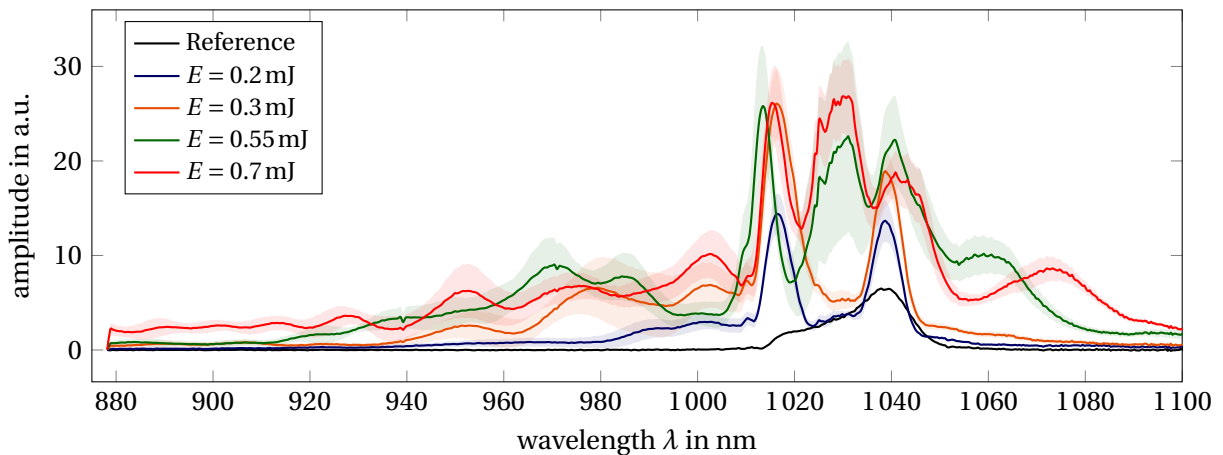


Fig. 4.10: Measured Spectra in two samples of 1.1 mm CR-39 placed in the Brewster angle into a multi-pass cell (MPC) of length $L = 10$ cm. The spectra were measured for different input energies. The reference was measured at low energy (0.1 mJ) without the nonlinear plastics.

typical behavior of SPM. A reference measurement was taken for a low input energy without the nonlinear materials. It also exhibits spectral broadening, which is presumably caused by SPM induced in air.

For a better investigation of the super-broadened spectrum far from 1030 nm, the same measurement was repeated using a short-pass filter as shown in figure 4.11. Here, a strong fluctuation of the energy can be seen. The periodic structure of the spectrum, which is also characteristic for SPM, is noticeable. The graph shows that a broad spectrum in the range of 900–1000 nm can be generated by this setup, which is suitable for optical probing. Even

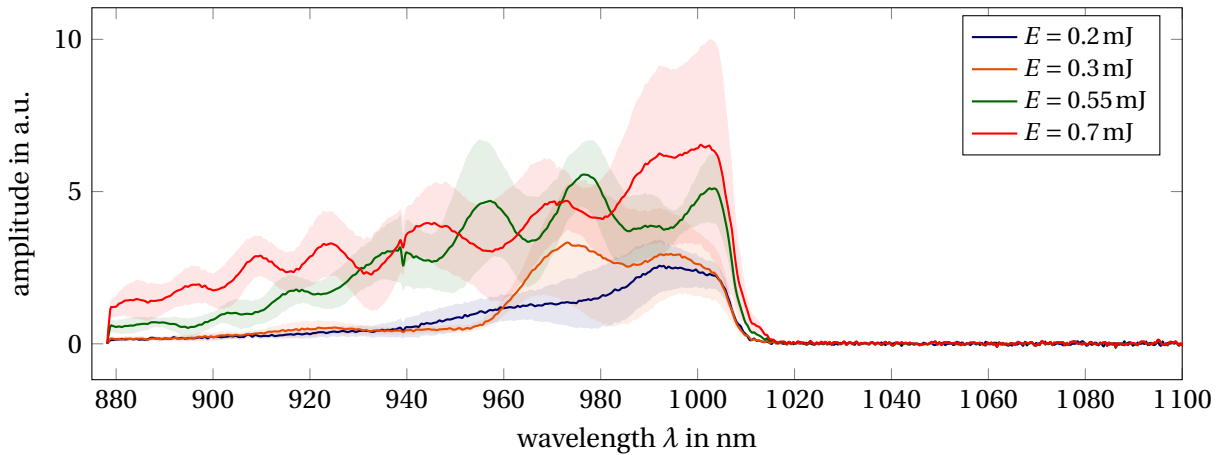


Fig. 4.11: Second measurement of spectra in two samples of 1.1 mm CR-39 placed in the Brewster angle into a MPC of length $L = 10$ cm. The spectra were measured for different input energies from the CPA system. In order to better characterize the spectral characteristics of the super-broadened spectrum, a short-pass filter was placed in front of the spectrometer.

though this setup is able to produce super-broadened spectra, there are a few problems that must be mentioned. The first issue is the geometry of the setup. As soon as the mirror distance L deviates from the confocal resonator setup ($L = 2f$), it becomes apparent that the focal position of the Gaussian beam in the resonator shifts. Firstly, the intensity of the beam is different each time it passes through the medium, which makes a numerical calculation of the spectrum more complex. Secondly, the focal position of the beam shifts towards the mirrors. If the laser beam is focused onto the mirror surface, the LIDT of the mirror is reached already at low pulse energies. For the gold coated curved input mirror, the supplier *Thorlabs* specifies a LIDT of 2 J/cm^2 for a wavelength of 1064 nm and sub-nanosecond pulses [71]. For a width of $200 \mu\text{m}$ of the collimated beam, a focal length 100 mm, the fluence in the focal spot at a pulse energy of 1 mJ is 1.1 J/cm^2 . Thus, in order to ensure that the mirror surface will not be damaged, the upper limit of the input energy into the Herriott cell is $E = 1.7$ mJ. However, the current setup is barely suitable for broadband probe pulse generation, since super-broadened pulses of about $20 \mu\text{J}$ are needed for probing experiments and a large fraction of the input energy is lost during spectral filtering. An energy measurement yielded pulse energies of less than $10 \mu\text{J}$. Despite the issues, this method is not depreciated from

further investigation. A possible solution to the problems might be the use of mirrors with larger diameter and focal lengths. This would allow resonator geometries with a larger beam waist diameter and thus higher energies to be used for amplification without destroying the mirrors. In addition, a higher pulse energy at the same intensity reduces undesirable nonlinear effects such as self-focusing (c. f. section 2.3). Larger setups are also advantageous since more than two samples of the nonlinear plastic can be placed between the mirrors, where they must be located at a distance from each other to ensure that sections with negligible SPM exist between them [41]. Furthermore, Herriott cells can also be implemented as gas filled multi-pass cell (MPC)s. If instead of a solid-state medium a gas is used, losses at optical interfaces can be reduced, which enables large overall efficiencies. Additionally, gases are not subject to laser induced damage, however, the nonlinear index is much lower compared to solid materials [69]. This ansatz is comparable to previous experiments of spectral broadening using gas-filled hollow core fibers (HCFs) [55]. However, for MPC the beam radius and hence the pulse energy is not as limited as in a HCF.

4.3. Impact of pulse steepening

The previous sections investigated the means of generating probe pulses with a broad bandwidth of 900–1000 nm up to energies of 50 μJ in this spectral domain. However, the simple theory of SPM introduced in section 2.3.2 is not able to qualitatively explain the observed spectra. That leads to the question, if the approximations made in the simple theory of SPM can be modified to explain the asymmetric broadening effect and the super-broadening phenomenon observed at high intensities above 3 TW/cm^2 (c.f. figures 4.2, 4.3 and 4.5) or if other nonlinear mechanisms come into play. The analysis of the origin of the super-broadening is important to optimize and reliably reproduce super-broadened spectra with the method investigated in section 4.1. As already discussed in section 2.3.3, for high intensity laser pulses, the Kerr-induced refractive index change $n(I) = n_0 + n_2 I$ leads to different group velocities of the peak and the rising and falling parts of the pulse, which causes a steepening of the pulse at the falling edge.

4.3.1. Numerical solution of pulse steepening

For a proper description of pulse steepening, the system of partial differential equations of pulse steepening (2.46) and (2.47) will be solved in the following. The equation for the field amplitude $|\mathcal{E}|$ (2.46) is a (nonlinear) homogeneous, first order partial differential equation, which can be solved implicitly via the method of characteristics [72, 73]. This yields an algebraic equation, which is solved numerically. A detailed mathematical derivation is given in appendix B.1. The calculation is performed for a thin foil of CR-39 as shown in figure 4.12.

As the numerical solver of the equation, *fsolve* of the Python package *scipy* was used, which is a root-finding algorithm to solve nonlinear equations [74]. For intensities smaller than

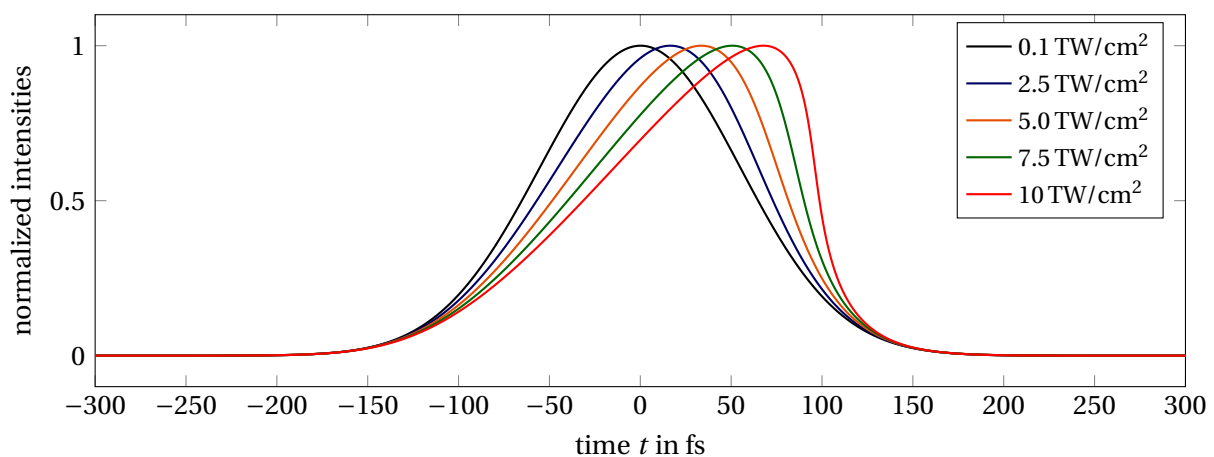


Fig. 4.12: Simulated temporal profiles of the pulse intensities for a 1.1 mm thick sheet of CR-39 with an initial pulse length of 130 fs (FWHM) for different intensities. For intensities larger than 1 TW/cm^2 a pulse steepening effect can be observed where the trailing edge ($t > 0$) is steepened due to the nonlinear index change for the peak of the pulse. Note that the magnitude of the curves was scaled to the maximum of the first curve at $I = 0.1 \text{ TW}/\text{cm}^2$ in order to emphasize the pulse steepening effect for larger intensities.

4.3 Impact of pulse steepening

12 TW/cm² the solver provides a distinct, smooth solution curve. For larger intensities, however, unphysical discontinuities occur at the steep trailing edge of the pulse. This is most likely due to multiple possible solutions of the algebraic equation, because the solution curve changes for different initial values. This effect can be reduced by first calculating the pulse shape for a lower intensity and using this as the initial guess value for the higher intensity curve. However, the solution method also fails here for intensities close to $I = 16 \text{ TW/cm}^2$.

Using the retrieved function for $|E|^2$, the nonlinear phase Φ_{NL} can now be calculated. Equation (2.47) must now be solved numerically, because $|E|^2$ is not an analytic function. Here, a Crank Nicolson scheme [75] is used as the integration algorithm, which is detailed in appendix B.2. The results of this computation for a 1.1 mm thick foil of CR-39 are shown in figure 4.13.

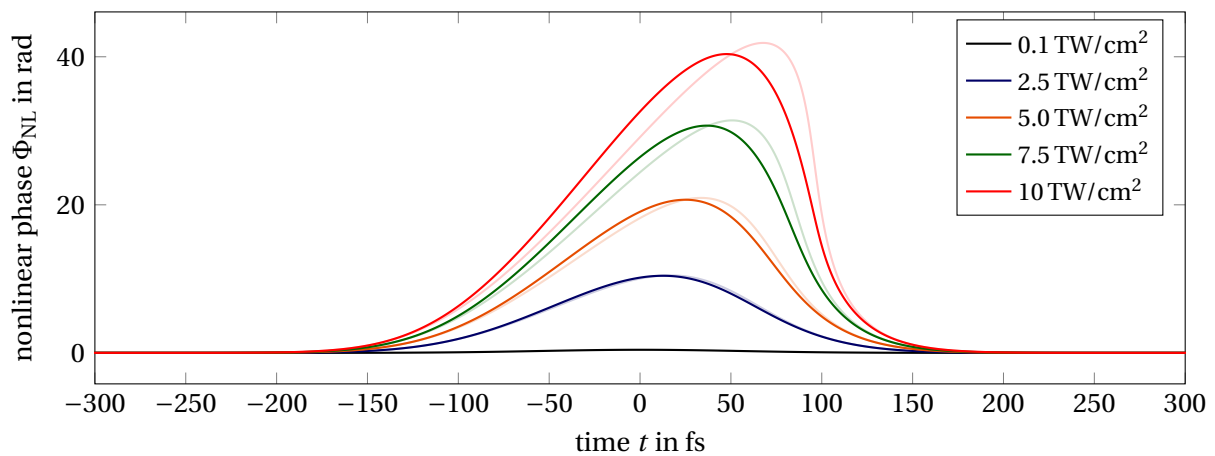


Fig. 4.13: Calculated nonlinear phase by numerically solving (2.47) with the temporal profiles of squared electric field amplitude calculated in figure 4.12. The desaturated curves show the simple calculation of the nonlinear phase according to equation (2.40).

The figure also shows the simple nonlinear phase calculation (desaturated curves) introduced in equation (2.40) as $\Phi_{\text{NL}}(t) = n_2 I(t) k_0 L$, where the intensities $I(t)$ calculated in figure 4.12 were used. It can be seen that, as expected, at low intensities the calculated nonlinear phase corresponds well to the simple model of calculating the nonlinear phase as being proportional to the pulse intensity. This also confirms the validity of the implemented algorithm. For pulses with a significant amount of pulse steepening a difference in the nonlinear phase appears and a numerical solution of equation (2.47) becomes necessary. Surprisingly, the proper calculation of the nonlinear phase $\Phi_{\text{NL}}(t)$ reduces the steepening compared to the assumption of $\Phi_{\text{NL}} \propto I$.

Finally, using the retrieved nonlinear phase of the pulse, the spectrum can be calculated straightforwardly with the squared magnitude of the FT of $E(t) \cdot \exp[-i(\omega_0 t + \Phi_{\text{NL}})]$ as previously described in equation (2.41). This was done for four different intensities in figure 4.14. When pulse steepening is considered, an asymmetric behaviour can be observed, which emphasizes the blue part (Anti-Stokes side) of the pulse. This additional spectral broadening

4.3 Impact of pulse steepening

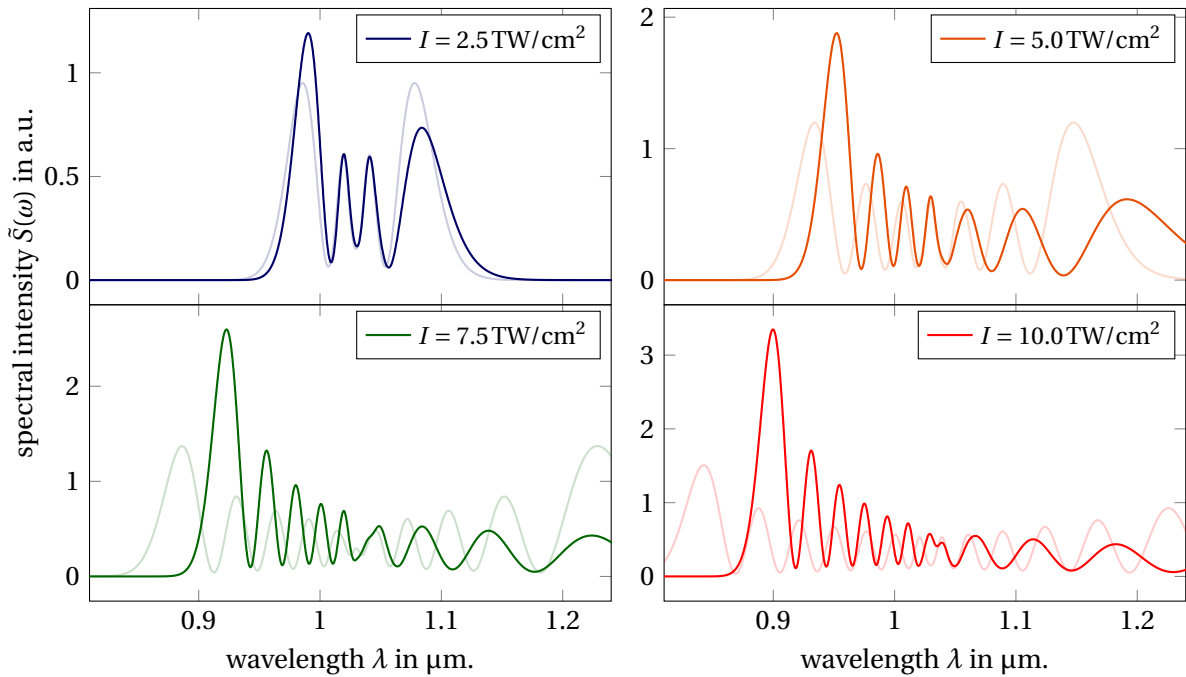


Fig. 4.14: Calculated spectra of an ultrashort pulse propagating through CR-39 at different intensities. The desaturated curves show the simple calculation of pulse broadening via SPM without pulse steepening effects taken into account.

is due to the steepening of the temporal profile of the nonlinear phase (c. f. figure 4.13). Since the temporal derivative of the phase corresponds to the instantaneous frequency, $\frac{\partial\Phi}{\partial t} = -\omega(t)$, a steeper trailing edge ($\frac{\partial\Phi}{\partial t} < 0$) generates additional spectral broadening at higher frequencies (c. f. section 2.3.2). In the above calculations, the dispersion of the medium n_0 , as a form of changing the pulse shape and likewise the dispersion of the nonlinear susceptibility $\chi^{(3)}$, was neglected. For short propagation lengths and nonlinearities far from resonances, this simplification is justified [38, p. 19]. The simulations show that the peaks on the Anti-Stokes side of the spectrum are enhanced, but the spectral shift is reduced and the peaks are narrower. These changes were also observed experimentally as seen in figure 4.2. On the Stokes side, however, the amplitude of the peaks is reduced.

4.3.2. Influence of the transverse intensity profile - focal averaging

The question now arises whether the calculated spectra describe the measured data from section 4.1 better. The asymmetry of the spectrum is successfully reproduced in the simulation, but it is noticeable that the observed super-broadening in the spectrum cannot be explained by pulse steepening. However, it must be noted that the laser beam in the experiment has an inhomogeneous, transverse intensity distribution. This means that the generated spectrum results as a superposition of many intensities with differently large proportions. Thus, it is not sufficient to calculate only the spectrum for the peak intensity on the

4.3 Impact of pulse steepening

beam axis. One possibility to include the transversal structure (sketched in in figure 4.15) in the calculations is a focal volume averaging.

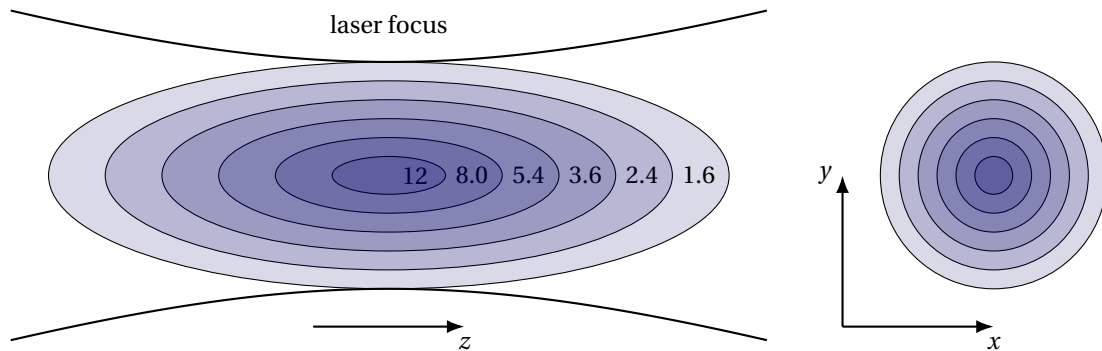


Fig. 4.15: Left: Intensity distribution in the laser focus of a Gaussian shaped laser beam. In a simplified model, the intensity distribution can be approximated as rings of constant thickness. The corresponding intensity drops according to the Gaussian distribution exponentially. Right: Intensity distribution in the focal plane. It can be seen that the focal volume of lower intensities is larger.

The idea of focal volume averaging is that different parts of the pulse will be broadened differently, because their intensity varies along the transverse direction. The transverse structure is approximated using N rings of different radius and intensity with a focal volume of $A_i \approx 2\pi r_i \Delta r$. Therefore, the parts of the pulse with lower intensity occupy a larger focal volume. The resulting spectrum is then a weighed sum of the individual spectra for each intensity

$$S(\lambda) = \frac{1}{r_N} \sum_{i=1}^N r_i \cdot S_i(\lambda). \quad (4.8)$$

This calculation is explicitly performed in figure 4.16 for a maximum peak intensity of $I_0 = 12 \text{ TW/cm}^2$ and different values of N . The resulting spectrum shows a converging behaviour for increasing size of N .

The simulated spectrum is comparable to the spectra measured in previous sections and predicts the super-broadening structure observed between 900–1000 nm. Especially, note the similarities between the linearly rising spectral amplitude in this spectral range in figure 4.16 compared to the measured spectra in figure 4.11. However, in most of the experiments a strong central peak or two symmetrically off-centered peaks due to *weaker* SPM effects are still observed. This is presumably due to the disregard of spatial effects caused by self-focusing and the disregard of parts of the pulse outside of the $(1/e^2)$ beam radius used in this model. A significant portion of the beam from the periphery self-focuses and accumulates little nonlinear phase [38, p. 22]. However, the presence of spatially different SPM and subsequent self-focusing badly alters the spatial and temporal intensity distributions of the laser pulse. It is suggested that actually self-focusing enhances the intensity in the medium

4.4 Summary and discussion

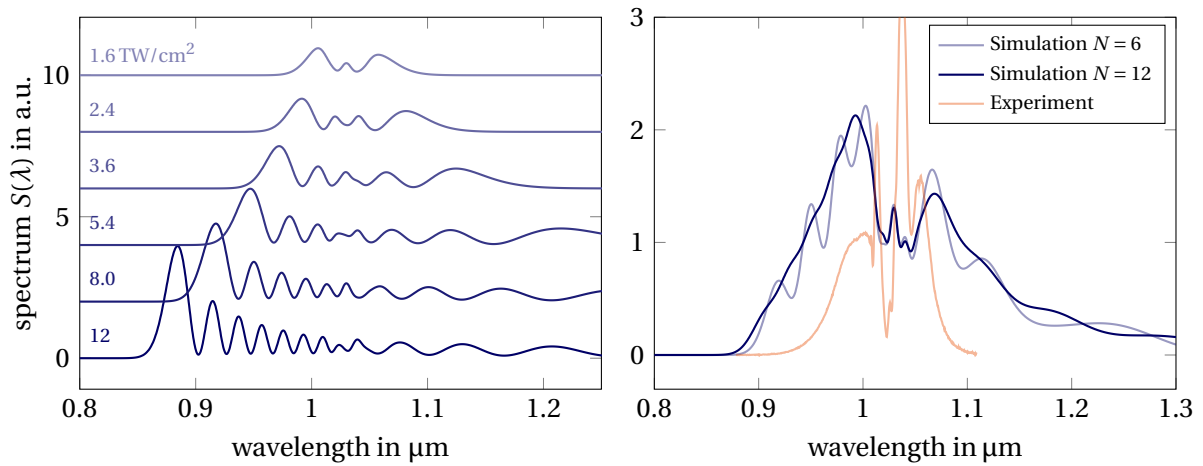


Fig. 4.16: Left: Calculated spectra including the effect of pulse steepening in CR-39 for different intensities of the laser pulse. The intensities correspond to rings of linearly increasing radius (c. f. 4.15). Right: Focal volume averaging for a transverse Gaussian distribution of intensities (blue). The spectra are summed up and weighed with the distance r to the optical axis since parts of lower intensity occupy a larger focal volume. The two symmetric peaks symmetric around 1030 nm are visible. Furthermore, the asymmetric spectral broadening for lower wavelengths is qualitatively reproduced. The orange curve show the experimental data from figure 4.5 at $I_0 = 11.3 \text{ TW/cm}^2$. The spectral broadening in this case is narrower than in the simulation, which is probably due to an overestimation of the peak intensity (c. f. equation (4.3) and the subsequent text).

and initiates strong temporal SPM [38, p. 29]. A complete theoretical description of SPM including self-focusing would require a time dependent solution of the nonlinear Schrödinger equation (NLS). With rapid spatial and temporal modifications of the laser pulse due to self-focusing, the solution of the wave equation is a daunting task [38, p. 30].

4.4. Summary and discussion

In this chapter we investigated the different means of SPM-based probe pulse generation using CPA amplified, mJ level, femtosecond pulses that are spectrally broadened in nonlinear materials. The currently employed method at the POLARIS laser system is the generation of a white-light continuum (WLC), which is amplified in a single pass non-collinear optical parametric amplifier (NOPA) by using the SH of the fundamental pulse as a pump. This system successfully provides 15–20 μJ ultrashort pulses in the sub-100 fs regime. However, this setup involves a total of three nonlinear optical processes, SHG, WLC and the NOPA. This leads to a high sensitivity to energy fluctuations at the output of the amplifier, influencing pulse energy, spatial shape and spectrum. Currently, the energy fluctuations of the system are about 30 %.

To circumvent these issues, we proposed a simple alternative method to generate the probe pulse. Here, the spectral broadening of the femtosecond pulse in nonlinear CR-39 is a promis-

ing method to generate pulses with spectral content in the range of 900–1000 nm and a pulse energy of up to 50 μJ . In the most straightforward approach, a single pass setup focuses the pulse onto the plastic realizing high intensities (up to 10 TW/cm^2). However, these high intensities in combination with a femtosecond pulse length may cause optical breakdown of the material or SPM effects in the surrounding air near the laser focus. Furthermore, nonlinear spatial effects such as self-focusing start to play a significant role for geometries with small foci, low pulse energy (c. f. table 2.1) and larger medium length. Moreover, slight modulations of the intensity profile of the beam become more pronounced due to the Kerr effect and may experience strong self-focusing, which causes the beam to collapse. This effect is called *filamentation*. Thus, for inhomogeneous beam profiles the self-focusing distance is smaller than expected and the B-integral is typically limited to values $B = \pi$ [41, p. 8].

The second proposal may bypass the problems of high intensities and small foci by propagating through the nonlinear medium several times in order to accumulate the required nonlinear phase for spectral broadening. The proposed method uses a multi-pass Herriott cell with two curved mirrors, which may be adjusted to realize more than 40 passes. However, due to low surface quality of the mirrors and adjustment issues, the geometry of the setup was reduced to a mirror distance of 10 cm, which corresponds to six passes in the Herriott cell. The results show that spectral broadening can be achieved by inserting multiple samples of the nonlinear medium in the beam path. Unfortunately the input pulse energy is limited by the LIDT of the mirrors. In order to work with higher input energies, a larger beam diameter in the focus of the mirror is required, however, the beam diameter is restricted by the geometry of the setup, since the mode of the input beam must be matched to the resonator mode for successful broadening [69]. The problems may be circumvented by using different resonator geometries with larger mirrors or gas-filled Herriott cells, which do not suffer from surface reflection losses.

Finally, a simulation based on the theory of self steepening was conducted for laser intensities up to $I = 12 \text{TW}/\text{cm}^2$. The resulting spectra were able to explain the experimentally observed asymmetric spectral broadening. A model was successfully developed to include transversal effects into the theory without solving the three dimensional nonlinear Schrödinger equation (NLS). Moreover, the model was able to qualitatively reproduce the shape of the spectral broadening.

5. Conclusion

With the help of today's laser technology, it is possible to realize high-energy interactions of radiation with matter on ultrashort time scales. This makes it possible to accelerate ions and electrons to ~ 100 MeV energies and potentially use them for medical applications such as cancer therapy [76], inertial confinement fusion [77] or for high energy particle colliders [78]. At the POLARIS laser system at the Friedrich Schiller University of Jena, laser pulses with peak powers of up to 200 TW are generated. These are focused on a target with peak intensities of more than 10^{20} W/cm². This generates a plasma, which is used to accelerate protons up to 20 MeV [10]. For a better understanding of the acceleration process initiated by laser-induced plasmas, an extended knowledge of the complex dynamics of the laser-plasma interaction is needed. For this purpose, an ultrafast optical probing setup is needed to study the complex details of the spatio-temporal evolution of the plasma density profile.

This work dealt with two major topics: In the first part, we used a pump-probe setup in a water micro-droplet experiment to study the temporal evolution of the plasma. The requirements for the probe pulse constitute a major challenge for the experimental generation of such pulses. A very broadband pulse far from the harmonics of the fundamental wavelength of the laser with sufficient energy and short pulse duration is required, otherwise scattering of the main laser pulse or strong plasma emission at the fundamental or the SH wavelength obscure the measurement. The requirements can be fulfilled by using different nonlinear optical effects. The basis of the probe pulse is provided by a Yb:FP15-based CPA system, seeded with pulses from the POLARIS oscillator, which amplifies the pulses to energies between 1–2 mJ at a pulse duration of 120 fs. For the probing experiment, we successfully operated and optimized the NOPA system developed at the institute. A broadband white-light continuum (WLC) was generated in a YAG crystal and amplified with a strong SH signal of the CPA amplified pulse. The output pulses contain up to 20 μ J of energy in a bandwidth of 200 nm (FWHM) centered around 800 nm. However, the setup requires three different nonlinear processes and is therefore very sensitive to energy fluctuations of the amplified CPA pulse. In the experiment we observed energy fluctuations of 30 %, which could be reduced by a careful alignment and proper thermalization of the CPA system. This probe pulse performance and stability were sufficient to conduct the pump-probe experiment. We used the pulses from the NOPA-system as an optical probe to study the micro-droplet experiment at the POLARIS laser. We illuminated the droplets with the off-harmonic probe pulse and took shadowgraphic images for different delays between probe and main pulse. We measured the evolution of the plasma expansion up to delays of 200 ps. In a range of 3–20 ps after the arrival of the main pulse, the plasma expansion was approximately linear with an expansion velocity of the plasma front $v_{\text{front}} = 1.3 \cdot 10^6$ m/s. It was noticeable that the plasma expansion behaves differently at the front and the rear side. Furthermore, we placed the glass plates for splitting the probe beam in the Brewster angle to mitigate p-polarized stray light from the main laser. Moreover, we successfully suppressed the plasma emission by a coronagraph setup, which was an opaque mask blocking the center of the droplet in an intermediate im-

age plane. This prevented an over-saturation of the cameras. In the future, the experimental setup can be extended by an interferometry setup in form of a Mach-Zehnder interferometer to analyze the plasma's density profile.

In the second part of the thesis, we searched for alternative means of probe pulse generation. A promising approach makes use of SPM-induced spectral broadening in highly-nonlinear media such as CR-39. At intensities larger than 1 TW/cm^2 , an asymmetric broadening of the spectrum in a 1 mm thick sheet of the nonlinear plastic was observed. In a single pass setup we were able to produce super-broadened pulses with pulse energies of up to $50 \mu\text{J}$ in a spectral width of 100 nm (FWHM) centered around 950 nm. The spectral range is mainly determined by the pulse intensity, however, large intensities impose an unwanted risk of damaging the material. In contrast to the NOPA setup, this scheme can be realized as a compact, low-cost method with lower requirements for adjustment precision. So far, the method has not yet been tested with the stabilized CPA system at the POLARIS laser system. The experimental conditions at the laser system used for the presented experiments are much different, with energy shot-to-shot fluctuations larger than at POLARIS. Therefore, we expect an improvement in stability of the generated spectra in future experiments.

Furthermore, we tested a second approach of SPM-based probe pulse generation using a multi-pass cell (MPC) built in a Herriott cell design with two nonlinear samples placed inside the resonator cavity. This offers the possibility to generate high nonlinear phases and broad spectra using lower peak intensities. However, this method has several restrictions. First, the input fluence is limited by the laser induced damage threshold (LIDT) of the mirrors. Second, the beam size is determined by the stable resonator mode of the mirror setup. The input beam has to be matched accordingly. Despite these restrictions a MPC setup is able to produce spectral broadening in the same spectral ranges as before. However, the alignment of the system is crucial and time consuming. The spectral broadening might be improved by using different resonator geometries with larger mirrors, which allow for higher intensities in the cavity. Furthermore, a gas-filled Herriott cell might reduce losses at interfaces, which then leads to higher efficiencies.

In conclusion, the generation of probe pulses using SPM in nonlinear plastics is a promising alternative method to the intricate, but flexible method of non-collinear optical parametric amplification. For higher peak intensities ($> 1 \text{ TW/cm}^2$), the effect of pulse steepening starts to play a significant role. Finally, we successfully simulated the resulting effect on the induced spectral broadening by numerically solving the system of partial differential equations of pulse steepening. In addition, we developed a simple model of focal volume averaging to include transverse effects, which was able to qualitatively describe the shape of the produced spectra. In the future it has to be tested if the method of SPM-based probe pulse generation is viable in an actual pump-probe experiment at POLARIS and can provide stable pump pulses over time scales of hours.

References

- [1] J. D. Cockcroft and E. T. Walton, “Experiments with high velocity positive ions. Further developments in the method of obtaining high velocity positive ions”, *Proceedings of the royal society of London. Series A, containing papers of a mathematical and physical character*, vol. 136, no. 830, pp. 619–630, 1932. DOI: 10.1098/rspa.1932.0107.
- [2] M. Pojer *et al.*, “LHC Operational Experience of the 6.5 TeV Proton Run with ATS Optics”, in *9th Int. Particle Accelerator Conf. (IPAC'18)*, 2018, pp. 216–219.
- [3] G. Amsel and G. Battistig, “The impact on materials science of ion beam analysis with electrostatic accelerators”, *Nuclear Instruments and Methods in Physics Research Section B: Beam Interactions with Materials and Atoms*, vol. 240, no. 1, pp. 1–12, 2005, Accelerators in Applied Research and Technology, ISSN: 0168-583X. DOI: 10.1016/j.nimb.2005.06.078.
- [4] A. J. Lennox, “Accelerators for cancer therapy”, *Radiation Physics and Chemistry*, vol. 61, no. 3, pp. 223–226, 2001, 8th International Symposium on Radiation Physics - ISRP8. DOI: 10.1016/S0969-806X(01)00244-4.
- [5] R. Bangerter, A. Faltens, and P. Seidl, “Accelerators for inertial fusion energy production”, in *Reviews of Accelerator Science and Technology*, World Scientific, 2014, pp. 85–116. DOI: 10.1142/9789814583251_0005.
- [6] V. Malka, “Laser plasma accelerators”, *Physics of Plasmas*, vol. 19, no. 5, p. 055501, 2012. DOI: 10.1063/1.3695389.
- [7] T. Tajima and J. M. Dawson, “Laser electron accelerator”, *Physical Review Letters*, vol. 43, no. 4, p. 267, 1979. DOI: 10.1103/PhysRevLett.43.267.
- [8] R. Bingham and R. Trines, “Introduction to Plasma Accelerators: the Basics”, en, *CERN Yellow Reports, Vol 1 (2016): Proceedings of the 2014 CAS–CERN Accelerator School: Plasma Wake Acceleration*, 2016. DOI: 10.5170/CERN-2016-001.67.
- [9] D. Strickland and G. Mourou, “Compression of amplified chirped optical pulses”, *Optics communications*, vol. 56, no. 3, pp. 219–221, 1985. DOI: 10.1016/0030-4018(85)90151-8.
- [10] J. Polz *et al.*, “Efficient laser-driven proton acceleration from a cryogenic solid hydrogen target”, *Scientific reports*, vol. 9, no. 1, pp. 1–8, 2019. DOI: 10.1038/s41598-019-52919-7.
- [11] J. Carstensen *et al.*, “Probing the Plasma Sheath by the Continuous Mass Loss of Microparticles”, *IEEE Transactions on Plasma Science*, vol. 41, no. 4, pp. 764–768, 2013. DOI: 10.1109/TPS.2012.2224330.
- [12] M. Urry, G. Gregori, O. Landen, A. Pak, and S. Glenzer, “X-ray probe development for collective scattering measurements in dense plasmas”, *Journal of Quantitative Spectroscopy and Radiative Transfer*, vol. 99, no. 1, pp. 636–648, 2006, Radiative Properties of Hot Dense Matter, ISSN: 0022-4073. DOI: 10.1016/j.jqsrt.2005.05.051.

- [13] A. Sävert *et al.*, “Direct observation of the injection dynamics of a laser wakefield accelerator using few-femtosecond shadowgraphy”, *Phys. Rev. Lett.*, vol. 115, p. 055 002, 5 Jul. 2015. DOI: 10.1103/PhysRevLett.115.055002.
- [14] A. Buck *et al.*, “Real-time observation of laser-driven electron acceleration”, *Nature Physics*, vol. 7, no. 7, pp. 543–548, 2011. DOI: 10.1038/nphys1942.
- [15] M. Mäusezahl, “Untersuchung lasergetriebener Protonenbeschleunigung bezüglich Vorplasmaerzeugung und räumlicher Protonendetektion”, Master’s Thesis, 2019.
- [16] Y. Azamoum *et al.*, “Single-Shot Measurements of Space-Time Resolved Laser-Induced Ionization Dynamics on Thin Foils”, *Annual Reports*, p. 1, 2020.
- [17] Y. Gao *et al.*, “An automated, 0.5 hz nano-foil target positioning system for intense laser plasma experiments”, *High Power Laser Science and Engineering*, vol. 5, e12, 2017. DOI: 10.1017/hpl.2017.10.
- [18] G. A. Becker *et al.*, “Characterization of laser-driven proton acceleration from water microdroplets”, *Scientific reports*, vol. 9, no. 1, pp. 1–8, 2019. DOI: 10.1038/s41598-019-53587-3.
- [19] I. Tamer, “Petawatt-class laser optimization and ultrashort probe pulse generation for relativistic laser-plasma interactions”, Ph.D. dissertation, 2020.
- [20] I. Tamer *et al.*, “Few-cycle fs-pumped nopa with passive ultrabroadband spectral shaping”, *Opt. Express*, vol. 28, no. 13, pp. 19 034–19 043, Jun. 2020. DOI: 10.1364/OE.388344.
- [21] T. Pertsch, *Lecture Notes: Grundkonzepte der Optik*. Friedrich-Schiller-Universität Jena, 2014.
- [22] F. Träger, *Springer handbook of lasers and optics*. Springer Science & Business Media, 2012.
- [23] W. Zinth and U. Aumüller, *Optik*. München: Oldenbourg Wissenschaftsverlag, 2013. DOI: 10.1524/9783486735819.
- [24] F. F. Chen, *Introduction to plasma physics and controlled fusion*. Springer Science & Business Media, 2018.
- [25] A. Einstein, “Zur Theorie der Lichterzeugung und Lichtabsorption”, *Annalen der Physik*, vol. 325, no. 6, pp. 199–206, 1906. DOI: 10.1002/andp.19063250613.
- [26] C. F. Perry, P. Zhang, F. B. Nunes, I. Jordan, A. von Conta, and H. J. Wörner, “Ionization energy of liquid water revisited”, *The Journal of Physical Chemistry Letters*, vol. 11, no. 5, pp. 1789–1794, 2020. DOI: 10.1021/acs.jpcllett.9b03391.
- [27] P. Gibbon, *Short pulse laser interactions with matter: an introduction*. World Scientific, 2005.
- [28] J. J. Sakurai and J. Napolitano, *Modern Quantum Mechanics*. Cambridge University Press, 2017.

References

- [29] J. A. Bittencourt, *Fundamentals of plasma physics*. Springer Science & Business Media, 2004.
- [30] W. Kruer, *The physics of laser plasma interactions*. CRC Press, 2018.
- [31] S. C. Wilks, W. L. Kruer, M. Tabak, and A. B. Langdon, “Absorption of ultra-intense laser pulses”, *Phys. Rev. Lett.*, vol. 69, pp. 1383–1386, 9 Aug. 1992. DOI: 10.1103/PhysRevLett.69.1383.
- [32] M. C. Kaluza, *Lecture Notes: High-Intensity Relativistic Optics*. Friedrich-Schiller-Universität Jena, 2020.
- [33] R. L. Sutherland, *Handbook of nonlinear optics*. CRC press, 2003.
- [34] R. W. Boyd, *Nonlinear optics*. Academic press, 2007.
- [35] A. Weiner, *Ultrafast optics*. John Wiley & Sons, 2009, vol. 72.
- [36] D. N. Schimpf, J. Rothhardt, J. Limpert, A. Tünnermann, and D. C. Hanna, “Theoretical analysis of the gain bandwidth for noncollinear parametric amplification of ultrafast pulses”, *J. Opt. Soc. Am. B*, vol. 24, no. 11, pp. 2837–2846, Nov. 2007. DOI: 10.1364/JOSAB.24.002837.
- [37] I. Tamer *et al.*, “Characterization and application of nonlinear plastic materials for post-CPA pulse compression”, *Opt. Lett.*, vol. 45, no. 24, pp. 6575–6578, Dec. 2020. DOI: 10.1364/OL.409637.
- [38] R. R. Alfano, *The supercontinuum laser source: the ultimate white light*. Springer, 2016.
- [39] P. L. Baldeck, P. Ho, and R. Alfano, “Effects of self, induced and cross phase modulations on the generation of picosecond and femtosecond white light supercontinua”, *revue de physique appliquée*, vol. 22, no. 12, pp. 1677–1694, 1987. DOI: 10.1051/rphysap:0198700220120167700.
- [40] G. Yang and Y. R. Shen, “Spectral broadening of ultrashort pulses in a nonlinear medium”, *Opt. Lett.*, vol. 9, no. 11, pp. 510–512, Nov. 1984. DOI: 10.1364/OL.9.000510.
- [41] P. Russbuedt, J. Weitenberg, A. Vernaleken, T. Sartorius, and J. Schulte, *Method and arrangement for spectral broadening of laser pulses for non-linear pulse compression*, US Patent 9,847,615, Dec. 2017.
- [42] C. Bernert *et al.*, “Off-harmonic optical probing of high intensity laser plasma expansion dynamics in solid density hydrogen jets”, *Scientific reports*, vol. 12, no. 1, pp. 1–11, 2022. DOI: 10.1038/s41598-022-10797-6.
- [43] D. Polli, D. Brida, S. Mukamel, G. Lanzani, and G. Cerullo, “Effective temporal resolution in pump-probe spectroscopy with strongly chirped pulses”, *Physical Review A*, vol. 82, no. 5, p. 053809, 2010. DOI: 10.1103/PhysRevA.82.053809.
- [44] M. Hornung *et al.*, “54J pulses with 18nm bandwidth from a diode-pumped chirped-pulse amplification laser system”, *Opt. Lett.*, vol. 41, no. 22, pp. 5413–5416, Nov. 2016. DOI: 10.1364/OL.41.005413.

- [45] H. Liebetrau *et al.*, “Intracavity stretcher for chirped-pulse amplification in high-power laser systems”, *Opt. Lett.*, vol. 42, no. 2, pp. 326–329, Jan. 2017. DOI: 10.1364/OL.42.000326.
- [46] G. Doumy *et al.*, “Complete characterization of a plasma mirror for the production of high-contrast ultraintense laser pulses”, *Physical Review E*, vol. 69, no. 2, 2004. DOI: 10.1103/PhysRevE.69.026402.
- [47] O. Stenzel *et al.*, *The physics of thin film optical spectra*. Springer, 2015.
- [48] I. H. Malitson, “Interspecimen comparison of the refractive index of fused silica”, *Josa*, vol. 55, no. 10, pp. 1205–1209, 1965. DOI: 10.1364/JOSA.55.001205.
- [49] U. Teubner and P. Gibbon, “High-order harmonics from laser-irradiated plasma surfaces”, *Rev. Mod. Phys.*, vol. 81, pp. 445–479, 2 Apr. 2009. DOI: 10.1103/RevModPhys.81.445.
- [50] J.-L. Bobin, “High intensity laser plasma interaction”, *Physics Reports*, vol. 122, no. 4, pp. 173–274, 1985. DOI: 10.1016/0370-1573(85)90077-8.
- [51] B. Lyot, “The study of the solar corona and prominences without eclipses (George Darwin Lecture, 1939)”, *Monthly Notices of the Royal Astronomical Society*, vol. 99, p. 580, 1939.
- [52] Takatsu-ku and Kawasaki-shi, *Microscope units and objectives*, English, Mitutoyo America Corporation, 40 pp.
- [53] S. Keppler, “Räumlich-zeitliche Optimierung der Laserimpulse Yb³⁺-basierter Hochleistungs-Lasersysteme”, Ph.D. dissertation, 2017.
- [54] G. Becker, Private communication, Nov. 2022.
- [55] M. Schwab *et al.*, “Few-cycle optical probe-pulse for investigation of relativistic laser-plasma interactions”, *Applied Physics Letters*, vol. 103, no. 19, p. 191118, 2013. DOI: 10.1063/1.4829489.
- [56] A. Kramida, Yu. Ralchenko, J. Reader, and NIST ASD Team, NIST Atomic Spectra Database (ver. 5.9), [Online]. Available: <https://physics.nist.gov/asd> [2022, September 27]. National Institute of Standards and Technology, Gaithersburg, MD. 2021.
- [57] M. Nolte, in preparation, Master’s Thesis, 2023.
- [58] G. Becker, “Characterization of laser-driven proton acceleration with contrast-enhanced laser pulses”, Ph.D. dissertation, 2021. DOI: 10.22032/dbt.49350.
- [59] F. Beg *et al.*, “A study of picosecond laser–solid interactions up to 10^{19} W/cm²”, *Physics of plasmas*, vol. 4, no. 2, pp. 447–457, 1997. DOI: 10.1063/1.872103.
- [60] H. Chen, S. C. Wilks, W. L. Kruer, P. Patel, and R. Shepherd, “Hot electron energy distributions from ultraintense laser solid interactions”, *Physics of plasmas*, vol. 16, no. 2, p. 020705, 2009. DOI: 10.1063/1.3080197.

References

- [61] T. Frieden, “Toxicological Profile for Ethylene Glycol”, *Agency for Toxic Substances and Disease Registry, Atlanta*, 2010. [Online]. Available: <https://www.atsdr.cdc.gov/ToxProfiles/tp96.pdf>.
- [62] T. Weickhart, “Configuration of a 1.03 μm diode pumped, CPA-system”, Bachelor’s Thesis, 2021.
- [63] E. Nibbering, G. Grillon, M. Franco, B. Prade, and A. Mysyrowicz, “Determination of the inertial contribution to the nonlinear refractive index of air, N₂, and O₂ by use of unfocused high-intensity femtosecond laser pulses”, *J. Opt. Soc. Am. B*, vol. 14, no. 3, pp. 650–660, Mar. 1997. DOI: 10.1364/JOSAB.14.000650.
- [64] R. L. Fork, C. V. Shank, C. Hirlimann, R. Yen, and W. J. Tomlinson, “Femtosecond white-light continuum pulses”, *Opt. Lett.*, vol. 8, no. 1, pp. 1–3, Jan. 1983. DOI: 10.1364/OL.8.000001.
- [65] R. Trebino, *Frequency-resolved optical gating: the measurement of ultrashort laser pulses*. Springer Science & Business Media, 2012.
- [66] E. Mével, O. Tcherbakoff, F. Salin, and E. Constant, “Extracavity compression technique for high-energy femtosecond pulses”, *JOSA B*, vol. 20, no. 1, pp. 105–108, 2003. DOI: 10.1364/JOSAB.20.000105.
- [67] D. Herriott, H. Kogelnik, and R. Kompfner, “Off-axis paths in spherical mirror interferometers”, *Applied Optics*, vol. 3, no. 4, pp. 523–526, 1964. DOI: 10.1364/AO.3.000523.
- [68] A. M. Kowalevich, A. Sennaroglu, A. T. Zare, and J. G. Fujimoto, “Design principles of q-preserving multipass-cavity femtosecond lasers”, *JOSA B*, vol. 23, no. 4, pp. 760–770, 2006. DOI: 10.1364/JOSAB.23.000760.
- [69] A.-L. Viotti *et al.*, “Multi-pass cells for post-compression of ultrashort laser pulses”, *Optica*, vol. 9, no. 2, pp. 197–216, Feb. 2022. DOI: 10.1364/OPTICA.449225.
- [70] W. Koechner, *Solid-state laser engineering*. Springer, 2006, vol. 1.
- [71] Thorlabs, *Protected Gold Mirrors*, https://www.thorlabs.com/newgrouppage9.cfm?objectgroup_id=744, [Online; accessed 8-September-2022], 2022.
- [72] H. J. Wilson, *Lecture Notes: Analytical Methods - First order PDEs*. London’s Gloabal University, 2014. [Online]. Available: <https://www.ucl.ac.uk/~ucahhwi/LTCC/>.
- [73] H. Weinberger, *A First Course in Partial Differential Equations: With Complex Variables and Transform Methods*. Dover Publications, 1995.
- [74] *Scipy fsolve*, <https://docs.scipy.org/doc/scipy/reference/generated/scipy.optimize.fsolve.html>, [Online; accessed 25-September-2022].
- [75] T. Pertsch, *Lecture Notes: Computational Photonics*. Friedrich-Schiller-Universität Jena, 2022.
- [76] C.-M. Ma *et al.*, “Development of a laser-driven proton accelerator for cancer therapy”, *Laser Physics*, vol. 16, no. 4, pp. 639–646, 2006. DOI: 10.1134/S1054660X06040165.

References

- [77] R. Betti and O. Hurricane, “Inertial-confinement fusion with lasers”, *Nature Physics*, vol. 12, no. 5, pp. 435–448, 2016. DOI: 10.1038/nphys3736.
- [78] C. B. Schroeder, E. Esarey, C. G. R. Geddes, C. Benedetti, and W. P. Leemans, “Physics considerations for laser-plasma linear colliders”, *Phys. Rev. ST Accel. Beams*, vol. 13, p. 101301, 10 Oct. 2010. DOI: 10.1103/PhysRevSTAB.13.101301.
- [79] J. Crank and P. Nicolson, “A practical method for numerical evaluation of solutions of partial differential equations of the heat-conduction type”, in *Mathematical proceedings of the Cambridge philosophical society*, Cambridge University Press, vol. 43, 1947, pp. 50–67.
- [80] Light Conversion, UAB, *Factory test certificate of FLINT femtosecond oscillator*, Model: FL1-04, 2019.
- [81] *Laserstrahl-Stabilisierung Compact*, German, version 13, MRC Systems GmbH, 2021, 36 pp.
- [82] M. Beyer, “Characterization of optical components of a laser amplifier via spectral interferometry”, Bachelor’s Thesis, 2020.
- [83] R. Glauber and F. Haake, “The initiation of superfluorescence”, *Physics Letters A*, vol. 68, no. 1, pp. 29–32, 1978, ISSN: 0375-9601. DOI: 10.1016/0375-9601(78)90747-8.
- [84] N. Stuart *et al.*, “Direct fluorescence characterisation of a picosecond seeded optical parametric amplifier”, *Optics Communications*, vol. 336, Feb. 2015. DOI: 10.1016/j.optcom.2014.09.032.
- [85] *Sony ILX511B*, <https://spectrecology.com/wp-content/uploads/2021/03/SONY-ILX511B.pdf>, Datasheet, [Online; accessed 16-September-2022], Sony.

List of abbreviations

BBO	β -barium borate
CPA	chirped pulse amplification
CR-39	poly allyl diglycol carbonate
CCD	charge-coupled device
DFG	difference frequency generation
FROG	frequency resolved optical gating
FT	Fourier transform
FT	Fourier transform-limited
FWHM	full width at half maximum
GDD	group delay dispersion
GVD	group velocity dispersion
HCF	hollow core fiber
HWP	half wave plate
JETI	Jenaer Titan:Saphir
KDP	potassium dideuterium phosphate
LIDT	laser induced damage threshold
MPC	multi-pass cell
MPI	multi-photon ionization
NLS	nonlinear Schrödinger equation
NOPA	non-collinear optical parametric amplifier
OAP	off-axis parabola
OPA	optical parametric amplifier
OR	optical rectification
OTBI	over the barrier ionization
PBS	polarizing beam splitter
ROI	region of interest
ROC	radius of curvature
POLARIS	Petawatt Optical Laser Amplifier for Radiation Intensive Experiments

List of abbreviations

SFG	sum frequency generation
SH	second harmonic
SHG	second harmonic generation
SPM	self phase modulation
SVEA	slowly varying envelope approximation
TI	tunnel ionization
WLC	white-light continuum
YAG	Yttrium aluminium garnet
Yb:FP15	Ytterbium doped fluoride phosphate

Appendix

A. Derivation of the nonlinear wave equation and phase

This sections deals with the derivation of the wave equation of propagating plane waves in a nonlinear, isotropic medium. The derived formulas are formulated in the SI-system and form the basis for the discussion of the temporal description of SPM in section 2.3.2 and self steepening in section 4.3. Using Maxwells equations without external sources ($\rho = 0, \mathbf{J} = 0$)

$$\nabla \times \mathbf{E}(\mathbf{r}, t) = -\frac{\partial}{\partial t} \mathbf{B}(\mathbf{r}, t) \quad \nabla \cdot \mathbf{D}(\mathbf{r}, t) = 0 \quad (\text{A.1a})$$

$$\nabla \times \mathbf{H}(\mathbf{r}, t) = \frac{\partial}{\partial t} \mathbf{D}(\mathbf{r}, t) \quad \nabla \cdot \mathbf{B}(\mathbf{r}, t) = 0, \quad (\text{A.1b})$$

the wave equation can be derived by applying curl to Faraday's law. For non-magnetic materials $\mathbf{B} = \mu_0 \mathbf{H}$ this leads to

$$\begin{aligned} \nabla \times (\nabla \times \mathbf{E}) &= \underbrace{\nabla (\nabla \cdot \mathbf{E})}_{=0} - \Delta \mathbf{E} = -\mu_0 \frac{\partial}{\partial t} \underbrace{(\nabla \times \mathbf{H})}_{=\frac{\partial}{\partial t} \mathbf{D}} \\ \Rightarrow \Delta \mathbf{E}(\mathbf{r}, t) &= \mu_0 \frac{\partial^2}{\partial t^2} \mathbf{D}(\mathbf{r}, t). \end{aligned} \quad (\text{A.2})$$

The assumption of $\nabla \cdot \mathbf{E} = 0$ is valid for isotropic materials, since ρ is homogenous in space.

A.1. Case without dispersion

For a third order nonlinear material the $\mathbf{D}(\mathbf{r}, t)$ field of a dispersionless medium $n_0 \neq n_0(\omega)$ can be written as

$$\begin{aligned} \mathbf{D}(\mathbf{r}, t) &= \varepsilon_0 \mathbf{E}(\mathbf{r}, t) + \mathbf{P}^{(1)}(\mathbf{r}, t) + \mathbf{P}^{(3)}(\mathbf{r}, t) \\ &= \varepsilon_0 n_0^2 \mathbf{E}(\mathbf{r}, t) + \mathbf{P}^{(3)}(\mathbf{r}, t) \quad \text{with} \quad n_0^2 = 1 + \chi^{(1)}. \end{aligned} \quad (\text{A.3})$$

Furthermore, using a plane wave ansatz with propagation in z -direction

$$\mathbf{E}(z, t) = \mathcal{E}(z, t) e^{i(kz - \omega_0 t)}, \quad (\text{A.4})$$

equation (A.2) can be written as

$$\left(\frac{\partial^2}{\partial z^2} - \frac{n_0^2}{c^2} \frac{\partial^2}{\partial t^2} \right) \mathbf{E} = \frac{1}{c^2 \varepsilon_0} \frac{\partial^2}{\partial t^2} \mathbf{P}^{(3)} \quad \text{with} \quad \mathbf{P}^{(3)} = \frac{3}{4} \varepsilon_0 \chi^{(3)} |\mathbf{E}|^2 \mathbf{E}. \quad (\text{A.5})$$

This result is a typical form of a inhomogeneous wave equation, where the third order polarization $\mathbf{P}^{(3)}$ acts as a source term generating new fields. The slowly varying envelope ap-

proximation (SVEA) now neglects the second order derivatives $\frac{\partial^2 \mathcal{E}}{\partial t^2}$ and $\frac{\partial^2 \mathcal{E}}{\partial z^2}$. This is justified because the pulse envelope \mathcal{E} changes slowly compared to the field oscillations with a periodicity of one optical cycle. Note that this is only true for *long* pulses with durations of more than ten optical cycles. The wave equation can now be simplified to

$$\frac{\partial^2}{\partial z^2} E = \frac{\partial}{\partial z} \left[\left(\frac{\partial}{\partial z} \mathcal{E} + ik \mathcal{E} \right) e^{i(kz - \omega_0 t)} \right] = \left(\frac{\partial^2}{\partial z^2} + 2ik \frac{\partial \mathcal{E}}{\partial z} - k^2 \right) e^{i(kz - \omega_0 t)} \quad (\text{A.6a})$$

$$\frac{\partial^2}{\partial t^2} E = \frac{\partial}{\partial t} \left[\left(\frac{\partial}{\partial t} \mathcal{E} - i\omega_0 \mathcal{E} \right) e^{i(kz - \omega_0 t)} \right] = \left(\frac{\partial^2}{\partial t^2} - 2i\omega_0 \frac{\partial \mathcal{E}}{\partial t} - \omega_0^2 \right) e^{i(kz - \omega_0 t)}. \quad (\text{A.6b})$$

These results can be inserted into equation (A.5). Then the expressions k^2 and ω_0^2 in equations (A.6a) and (A.6b) will cancel, which leads to

$$2ik \left(\frac{\partial \mathcal{E}}{\partial z} + \frac{n_0^2 \omega_0}{c^2} \frac{\partial \mathcal{E}}{\partial t} \right) e^{i(kz - \omega_0 t)} = \frac{1}{c^2 \epsilon_0} \frac{\partial^2}{\partial t^2} \mathbf{P}^{(3)}. \quad (\text{A.7})$$

In the evaluation of $\frac{\partial^2}{\partial t^2} \mathbf{P}^{(3)}$ the time derivatives of the envelope are neglected

$$\begin{aligned} \frac{\partial^2}{\partial t^2} \mathbf{P}^{(3)} &= \frac{3\epsilon_0}{4} \chi^{(3)} \left(\frac{\partial^2 |\mathcal{E}|^2 \mathcal{E}}{\partial t^2} - 2i\omega \frac{\partial |\mathcal{E}|^2 \mathcal{E}}{\partial t} - \omega_0^2 |\mathcal{E}|^2 \mathcal{E} \right) e^{i(kz - \omega_0 t)} \\ &\approx -\frac{3}{4} \omega_0^2 \epsilon_0 \chi^{(3)} |\mathcal{E}|^2 \mathcal{E} e^{i(kz - \omega_0 t)}. \end{aligned} \quad (\text{A.8})$$

Inserting this approximation into (A.7), canceling the exponentials on both sides and using $k = k_0 n_0$ leads to

$$\left(\frac{\partial}{\partial z} + \frac{n_0}{c} \frac{\partial}{\partial t} \right) \mathcal{E} = -\frac{3}{4} \frac{k_0}{2in_0} \chi^{(3)} |\mathcal{E}|^2 \mathcal{E}, \quad (\text{A.9})$$

which is used as the simplified wave equation formula in equation (2.37). Now the (complex) field envelope \mathcal{E} is split up into phase and amplitude $\mathcal{E} = |\mathcal{E}| e^{i\Phi}$. A variable transformation $z' = z + \frac{c}{n_0} t$ simplifies the equation to

$$\frac{\partial \mathcal{E}}{\partial z'} = \left(\frac{1}{|\mathcal{E}|} \frac{\partial |\mathcal{E}|}{\partial z} + i \frac{\partial \Phi}{\partial z} \right) \mathcal{E} = -\frac{3}{4} \frac{k_0}{2in_0} \chi^{(3)} |\mathcal{E}|^2 \mathcal{E}. \quad (\text{A.10})$$

Sorting both sides for real and imaginary part yields two equations for $|\mathcal{E}|$ and Φ

$$\frac{\partial |\mathcal{E}|}{\partial z} = 0 \quad \text{and} \quad \frac{\partial \Phi}{\partial z} = \frac{3}{4} \frac{k_0}{2n_0} \chi^{(3)} |\mathcal{E}|^2. \quad (\text{A.11})$$

The solution of the phase can be written as

$$\Phi(z, t) = \Phi_0 + n_2 I k_0 z \quad \text{with} \quad n_2 = \frac{3\chi^{(3)}}{4\epsilon_0 n_0^2 c} \quad \text{and} \quad I = \frac{n_0 c \epsilon_0}{2} |\mathcal{E}|^2. \quad (\text{A.12})$$

A.2. Case with dispersion

In the following it is assumed that the refractive index is frequency dependent, whereas the third order nonlinear susceptibility is still constant $\chi^{(3)} \neq \chi^{(3)}(\omega)$. Then the dielectric displacement $\mathbf{D}(z, t)$ can be written as

$$\mathbf{D}(z, t) = \mathbf{D}_L(z, t) + \varepsilon_0 \mathbf{P}^{(3)}(z, t) \Rightarrow \Delta \mathbf{E}(z, t) - \mu_0 \frac{\partial^2}{\partial t^2} \mathbf{D}_L = \frac{1}{c^2 \varepsilon_0} \frac{\partial^2}{\partial t^2} \mathbf{P}^{(3)}. \quad (\text{A.13})$$

The displacement field is now written using the frequency components $\tilde{\mathbf{E}}(z, \omega)$ as a Fourier transform [38, p.94 ff.]

$$\begin{aligned} \mathbf{D}_L(z, t) &= \frac{\varepsilon_0}{\sqrt{2\pi}} \int_{-\infty}^{\infty} n^2(\omega) \tilde{\mathbf{E}}(z, \omega) e^{-i\omega t} d\omega \\ -\frac{\partial^2}{\partial t^2} \mathbf{D}_L(z, t) &= -\frac{\varepsilon_0}{\sqrt{2\pi}} \int_{-\infty}^{\infty} \underbrace{(-\omega)^2 n^2(\omega)}_{-k^2(\omega)} \tilde{\mathbf{E}}(z, \omega) e^{-i\omega t} d\omega. \end{aligned} \quad (\text{A.14})$$

$$\left| \frac{1}{\sqrt{2\pi}} \int_{-\infty}^{\infty} \mathbf{E}(z, t') e^{i\omega t'} dt' \right.$$

Now the the plane wave ansatz (A.4) $\mathbf{E}(z, t') = \mathcal{E} \exp[i(k(\omega_0)z - \omega_0 t')]$ can be used again for the electric field. Furthermore, the wave vector k^2 is expanded into a Taylor series at $\omega = \omega_0$

$$\begin{aligned} &\left| \begin{aligned} \text{Taylor series: } k^2(\omega) &= k^2 + 2kk'(\omega - \omega_0) + kk''(\omega - \omega_0)^2 + \dots \quad (\text{A.15}) \\ &= \frac{\varepsilon_0}{2\pi} \iint_{-\infty}^{\infty} [k^2 + 2kk'(\omega - \omega_0) + kk''(\omega - \omega_0)^2] \mathcal{E} e^{i(\omega - \omega_0)(t' - t)} e^{i(k(\omega_0)z - \omega_0 t)} d\omega dt' \\ \text{Dirac delta function: } &\frac{1}{2\pi} \int_{-\infty}^{\infty} (\omega - \omega_0)^n e^{i(\omega - \omega_0)(t' - t)} d\omega = i^n \delta^{(n)}(t' - t), \quad n \in \mathbb{N} \\ &= \frac{\varepsilon_0}{2\pi} \int_{-\infty}^{\infty} [k^2 \delta(t' - t) + 2ikk' \delta^{(1)}(t' - t) - kk'' \delta^{(2)}(t' - t)] \mathcal{E}(z, t') e^{i(k(\omega_0)z - \omega_0 t)} dt' \\ &= \varepsilon_0 \left[k^2 + 2ikk' \frac{\partial \mathcal{E}}{\partial t} - kk'' \frac{\partial^2 \mathcal{E}}{\partial t^2} \right] e^{i(k(\omega_0)z - \omega_0 t)}. \end{aligned} \right. \quad (\text{A.16}) \end{aligned}$$

Together with the previous results (A.6a) and (A.8), (A.16) can be substituted into (A.13). The derivatives of k are recognized as group velocity $v_g = k'^{-1}(\omega_0)$ and group velocity dispersion $\text{GVD} = k''(\omega_0)$. Then the wave equation takes the following form:

$$i \left(\frac{\partial}{\partial z} + \frac{1}{v_g} \frac{\partial}{\partial t} \right) \mathcal{E} - \frac{\text{GVD}}{2} \frac{\partial^2}{\partial t^2} \mathcal{E} = -\frac{3}{4} \frac{k_0}{2in_0} \chi^{(3)} |\mathcal{E}|^2 \mathcal{E}. \quad (\text{A.17})$$

This equation is commonly called nonlinear Schrödinger equation (NLS). Neglecting the GVD term, the dispersionless equation (A.9) can be obtained.

B. Theoretical description and numerical methods of pulse steepening

This section deals with the derivation of the solution of equation (2.44), which takes the form

$$\underbrace{\left(\frac{\partial}{\partial z} + \frac{n_0}{c} \frac{\partial}{\partial t}\right)}_{D_+} \mathcal{E} + \frac{1}{2ik} \underbrace{\left(\frac{\partial^2}{\partial z^2} - \frac{n_0^2}{c^2} \frac{\partial^2}{\partial t^2}\right)}_{D_- D_+} \mathcal{E} = \frac{1}{2ik} \underbrace{\frac{3\omega_0^2}{4c^2} \left(\frac{1}{\omega_0^2} \frac{\partial^2}{\partial t^2} - \frac{2i}{\omega_0} \frac{\partial}{\partial t} - 1\right)}_{\xi} \chi^{(3)} |\mathcal{E}|^2 \mathcal{E}. \quad (\text{B.18})$$

The steepening of the temporal profile makes the assumption of a slowly varying envelope obsolete. The derivation follows Yang and Shen [40] in SI-units. Using the abbreviations introduced in equation (B.18), the differential equation can be written as

$$D_+ \mathcal{E} + \frac{1}{2ik} D_- D_+ \mathcal{E} = \frac{1}{2ik} \xi \Rightarrow D_+ \mathcal{E} = \frac{1}{2ik} \left[\frac{1}{1 + \frac{D_-}{2ik}} \right] \xi. \quad (\text{B.19})$$

The last equation is the limit of a geometric series, namely

$$D_+ \mathcal{E} = \frac{1}{2ik} \sum_{m=0}^{\infty} \left(-\frac{D_-}{2ik} \right)^m \xi. \quad (\text{B.20})$$

Using that $D_- = -\frac{2n_0}{c} \frac{\partial}{\partial t} + D_+$, equation (B.20) can be written in terms of D_+ only. In the following the third order nonlinearity is assumed to act as a small perturbation of the homogeneous wave equation $\chi^{(3)} |\mathcal{E}|^2 \ll 1$, which in case of CR-39 is valid for intensities $I < 400 \text{ TW/cm}^2$. For all conducted experiments of section 4.1 and 4.2 the peak intensity in the interaction plane was less than 20 TW/cm^2 . Now (B.20) can be simplified by neglecting all higher order terms of $D_+^m (\chi^{(3)} |\mathcal{E}|^2 \mathcal{E})$ with $m \geq 1$ and by eliminating the time derivatives in ξ . Then only the first two terms of the geometric sum remain, which yields (using $k = k_0 n_0$)

$$D_+ \mathcal{E} = \frac{1}{2ik} \sum_{m=0}^{\infty} \left[\left(\frac{1}{i\omega_0} \frac{\partial}{\partial t} \right)^m \xi \right] \approx \left(1 + \frac{i}{\omega_0} \frac{\partial}{\partial t} \right) \left[-\frac{3}{4} \frac{k_0}{2in_0} \chi^{(3)} |\mathcal{E}|^2 \mathcal{E} \right]. \quad (\text{B.21})$$

Substituting the definition of D_+ and rearranging the equation, the final differential equation (2.45) appears, which is written down again here:

$$\frac{\partial \mathcal{E}}{\partial z} + \frac{1}{c} \frac{\partial}{\partial t} (n_0 + \tilde{n}_2 |\mathcal{E}|^2) \mathcal{E} = i \frac{\tilde{n}_2 \omega_0}{c} |\mathcal{E}|^2 \mathcal{E} \quad \text{with} \quad \tilde{n}_2 \stackrel{(2.39)}{=} \frac{\epsilon_0 n_0 c}{2} n_2. \quad (\text{B.22})$$

As already described on page 19, the electric field can be written as $\mathcal{E} = |\mathcal{E}| e^{i\Phi}$. Then the differential equation can be split into real and imaginary part that results in the system of coupled differential equations (2.46) and (2.47). The numerical methods of solving these equations will be presented in the next sections.

B.1. Method of Characteristics

In this section we discuss the solution of the first differential equation (2.46), which results from a separation of equation (B.22) into amplitude $|\mathcal{E}|$ and phase Φ :

$$\left[\frac{\partial}{\partial z} + \frac{n_0}{c} \left(1 + \frac{3\tilde{n}_2}{n_0} |\mathcal{E}|^2 \right) \frac{\partial}{\partial t} \right] |\mathcal{E}| = 0, \quad (\text{B.23})$$

The equation (B.23) is a (nonlinear) homogeneous, first order partial differential equation. Such equations are commonly solved via the method of characteristics [72, 73] with a characteristic function $|\mathcal{E}|^2 = F(t_0)$. The characteristic curve is given as

$$\frac{dt}{dz} = \frac{n_0}{c} \left(1 + \frac{3\tilde{n}_2}{n_0} F(t_0) \right). \quad (\text{B.24})$$

For the initial condition $z_0 = 0$, the characteristic solution can be derived as

$$\begin{aligned} t_0 &= t - \frac{n_0}{c} \left(1 + 3 \frac{\tilde{n}_2}{n_0} F(t_0) \right) z \\ \Rightarrow |\mathcal{E}|^2 &= F(t_0) = F \left[t - \frac{n_0}{c} \left(1 + 3 \frac{\tilde{n}_2}{n_0} F(t_0) \right) z \right]. \end{aligned} \quad (\text{B.25})$$

Since the pulse shape at the entrance of the medium ($z = 0$) has a Gaussian shape (initial value problem), the characteristic function at $z = 0$ is also assumed to be Gaussian

$$|\mathcal{E}|^2(z = 0, t) = \mathcal{E}_0^2 \exp \left[- \left(\frac{t}{\tau} \right)^2 \right] \quad \text{with} \quad \tau = \frac{\tau_{\text{FWHM}}}{2\sqrt{\ln 2}}. \quad (\text{B.26})$$

Inserting the argument of the characteristic function into this ansatz leads to the following algebraic equation for the field amplitude

$$|\mathcal{E}|^2 = \mathcal{E}_0^2 \exp \left[- \left(x - Q \frac{\mathcal{E}^2}{\mathcal{E}_0^2} \right)^2 \right] \quad \text{with} \quad x = \frac{t - \frac{n_0}{c} z}{\tau} \quad \text{and} \quad Q = \frac{3\tilde{n}_2 z}{c\tau} \mathcal{E}_0^2 \quad \text{with} \quad \tilde{n}_2 = \frac{\varepsilon_0 n_0 c}{2} n_2, \quad (\text{B.27})$$

where the time t was substituted with a *retarded time* x , which describes the pulse propagation in a moving frame of reference where the pulse is stationary. Equation (B.27) can now be solved numerically for a given value of $z = L = 1.1$ cm for all times x .

B.2. Crank-Nicolson scheme

With a solution of the electric field amplitude $|\mathcal{E}|$ we can solve the second part of the coupled differential equations (equation (2.47)), which is given as

$$\left[\frac{\partial}{\partial z} + \frac{n_0}{c} \left(1 + \frac{\tilde{n}_2}{n_0} |\mathcal{E}|^2 \right) \frac{\partial}{\partial t} \right] \Phi = \frac{\tilde{n}_2 \omega_0}{c} |\mathcal{E}|^2. \quad (\text{B.28})$$

For the numerical solution of (B.28) it is convenient to perform a coordinate transformation into the propagation direction z and retarded time x

$$\frac{\partial}{\partial t} \rightarrow \frac{\partial}{\partial x} \quad \text{and} \quad \frac{\partial}{\partial z} \rightarrow \frac{\partial}{\partial z} + \frac{\partial}{\partial x} \frac{\partial x}{\partial z} = \frac{\partial}{\partial z} - \frac{n_0}{c\tau} \frac{\partial}{\partial x}. \quad (\text{B.29})$$

Then the transformed equation reads

$$\frac{\partial \Phi}{\partial z} = \underbrace{-\frac{\tilde{n}_2 |\mathcal{E}|^2}{\tau c} \frac{\partial}{\partial x}}_{L(x,z)} \Phi + \underbrace{\frac{\tilde{n}_2 \omega_0}{c} |\mathcal{E}|^2}_{F(x,z)}. \quad (\text{B.30})$$

Now a discretization of time with $x = x_i$ and space $z = z_j$ is introduced. Then the time derivative $\frac{\partial}{\partial x}$ can be expressed as a central difference operator in a first order approximation, which allows $L(x, z)$ to be written in matrix form like

$$\frac{\partial \Phi_{i,j}}{\partial x} = \frac{\Phi_{i+1,j} - \Phi_{i-1,j}}{2\Delta x} \quad \text{and} \quad \hat{L} = -\frac{\tilde{n}_2 |\mathcal{E}|^2}{\tau c} \frac{1}{2\Delta x} \begin{pmatrix} 0 & 1 & 0 & \dots & 0 \\ -1 & 0 & 1 & 0 & 0 \\ 0 & -1 & 0 & \ddots & 0 \\ \vdots & 0 & \ddots & \ddots & 1 \\ 0 & 0 & 0 & -1 & 0 \end{pmatrix}. \quad (\text{B.31})$$

The spatial derivative can now discretized using the Crank-Nicolson (CN) scheme, which is a finite difference, numerically stable method developed by Crank and Nicolson in 1947 [79]

$$\left. \frac{\partial \Phi_i}{\partial z} \right|_{z_{j+\frac{1}{2}}} \approx \frac{\Phi_{i,j+1} - \Phi_{i,j}}{\Delta z} \stackrel{\text{CN}}{\approx} \frac{1}{2} \sum_l (L_{l,j+1} \Phi_{l,j+1} + L_{l,j} \Phi_{l,j} + F_{l,j+1} + F_{l,j}). \quad (\text{B.32})$$

The equation can be vectorized for all times x_i and rearranged in the following way

$$\begin{aligned} \Phi_{j+1} &= \Phi_j + \frac{\Delta z}{2} (\hat{L} \Phi_{j+1} + \hat{L} \Phi_j + F_{j+1} + F_j) \\ \left(\mathbb{1} - \frac{\Delta z}{2} \hat{L} \right) \Phi_{j+1} &= \left(\mathbb{1} + \frac{\Delta z}{2} \hat{L} \right) \Phi_j + \frac{\Delta z}{2} (F_{j+1} + F_j). \end{aligned} \quad (\text{B.33})$$

Then the phase at the next z -value Φ_{j+1} can be determined by solving (B.33) via a matrix solver because F is already known for all times j .

C. Characterization of the CPA system

In the following section we discuss the setup of the chirped pulse amplification (CPA) system, which is used for generation of the probe pulses at POLARIS. CPA is a technique used in high power laser systems to amplify high power laser pulses. First, the pulse is temporally stretched, then amplified and finally compressed again. It was developed by Strickland and Mourou in 1985 [9] and earned them the Nobel Prize in physics in 2018.

C.1. CPA setup

First, a single pulse ($\tau < 90$ fs) is picked out of the 76 MHz pulse train from the Ytterbium-based POLARIS main oscillator (Flint FL1-04) [80] with a Pockels cell at a repetition rate of 1 Hz and sent to the stretcher, which is located in the target area of POLARIS. The Offner type stretcher setup is able to stretch the pulses from 130 fs to 20 ps and is described in figure C.1.

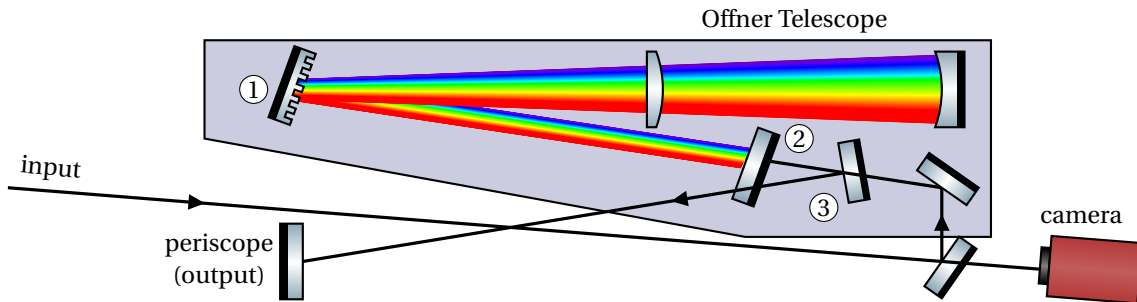


Fig. C.1: Setup of the Offner Type stretcher used to stretch the POLARIS seed from 130 fs to 20 ps, which then propagates to the CPA setup depicted in figure C.2. The input seed is brought into the stretcher, the grating (1) (1200 lines/mm) separates the wavelengths spatially and the Offner telescope introduces a temporal delay between different wavelengths. Then the beam is vertically displaced upwards (1 cm) by a roof mirror (2), enters the setup again and exits at a slightly lower position such that a D-cut mirror (3) redirects the beam out of the setup. Leakage light from a dielectric mirror is used with a camera to verify the position of the input beam, which is crucial for aligning the setup. For a high level of mobility the stretcher setup was built onto a movable breadboard.

Since the beam line between the oscillator and stretcher is several tens of meters long, a motorized beam-steering system with two mirrors and (4 quadrant diode) detectors [81] was installed in the beam line. The first steering mirror was placed near the pulse picking Pockels cell, therefore the stretcher is located behind the first steering mirror, which improves the stability of the seed. For an accurate positioning of the beam the first detector (D1) should be placed right behind the second steering mirror [81, p.17].

Then the stretched pulse enters the amplifier setup, which is depicted in figure C.2. The seed position is fixed using apertures and the *seed cam*. The input seed energy can be controlled

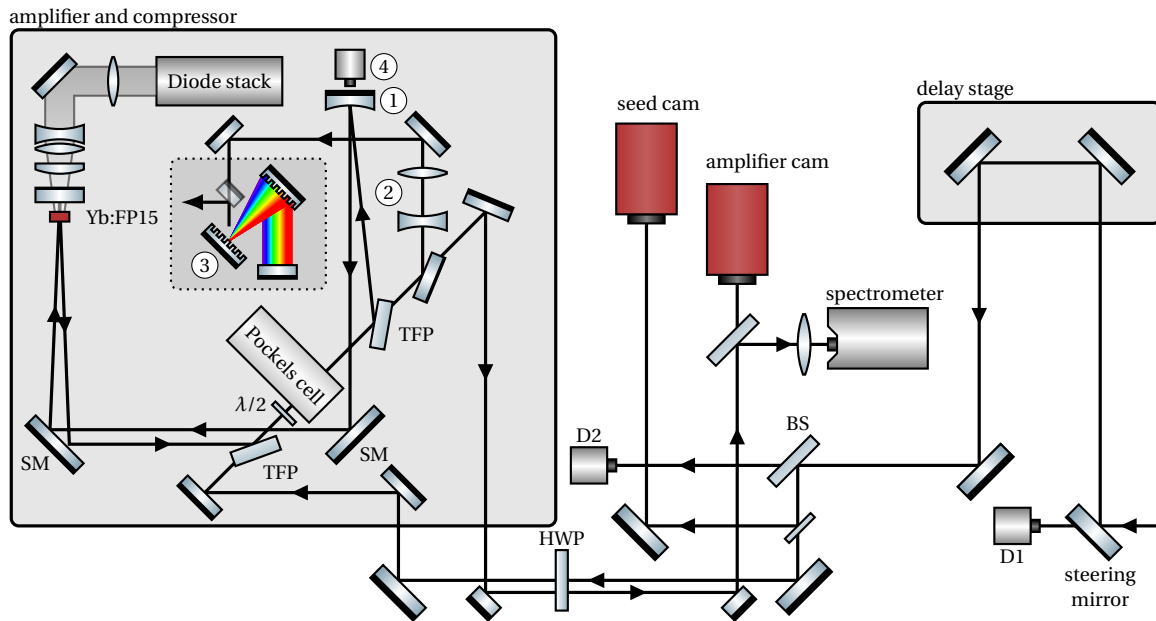


Fig. C.2: The seed pulse is stabilized via a steering system consisting of 2 diodes (D1 and D2) and steering mirrors. The seed energy can be adjusted using a rotatable HWP in front of the cavity. The seed enters then a CPA system consisting of a regenerative amplifier with an optical cavity (end mirror (1) with radius of curvature $R = 5$ m) and a diode pumped Yb:FP15 crystal as the active material. The gain profile is homogenized via spectral shaping mirrors (SM). The amplified pulse is magnified via a 1:4 Galilean telescope (2) and the pulse is compressed to 120 fs by a parallel grating compressor (3) with a roof mirror and sent upwards to the NOPA setup depicted in figure 3.1. The amplification of the pulse for each round trip and pulse energy can be estimated using the leakage light of the end mirror detected by a photo diode (4).

by a motorized half wave plate (HWP) placed before the entrance of the amplifier and compressor box. The seed is then amplified with a regenerative amplifier. Some leakage light of a dielectric mirror is sent to the *amplifier cam* and a high resolution (HR2000+) Ocean Optics spectrometer to analyze the amplifier parameters during the experiment. The amplified pulse is then compressed back to 120 fs and sent to the NOPA setup via a periscope.

C.2. Amplifier characterization

For successful operation of the NOPA, a stable CPA-amplified pulse must first be provided. For this, the coupling of the seed into the amplifier is chosen to provide a pulse energy of 1.3–1.5 mJ. Then the spectrum and the transverse profile of the beam must be checked. A measurement of this is shown in Figure C.3.

Since the SHG crystal is phase matched for a center wavelength of 1030 nm, the center of the pulse should not be far off. The amplifier is optimized for a diode pump current of 125 A. By rebuilding the front end with a new, more powerful oscillator at the end of 2021, a reduction of the pump current would have been possible, since a much higher seed energy is available. However, reducing the pump current shifts the spectral profile of the amplifier

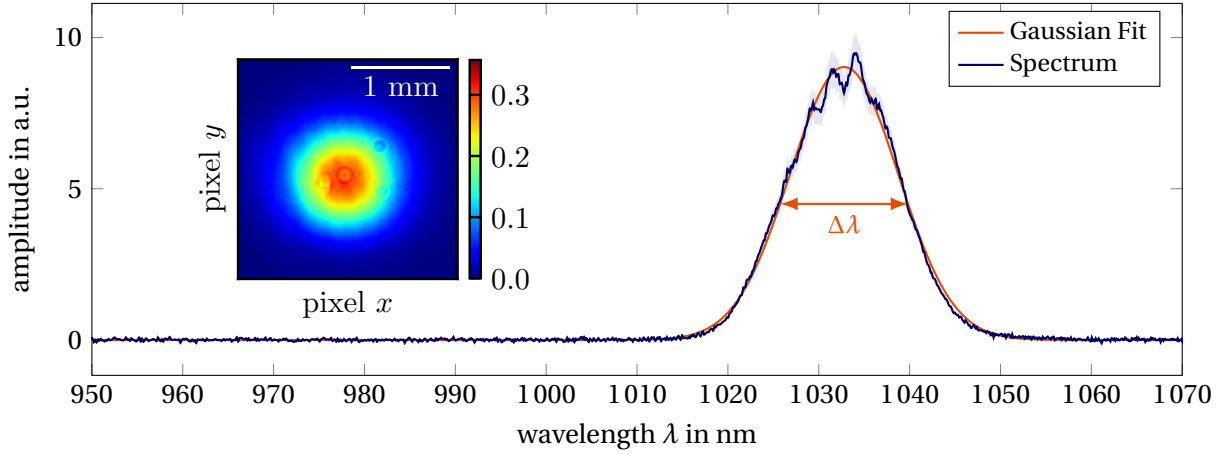


Fig. C.3: Measured spectrum of the Amplifier recorded by the spectrometer depicted in figure C.2. The graph shows the averaged spectrum for 80 consecutive shots. The standard deviation is indicated with the shaded area. The central wavelength $\lambda_0 = 1032.8$ nm, and width $\Delta\lambda = 14.1$ nm (FWHM) were determined using a Gaussian fit indicated in orange. The inset figure shows the spatial profile of the amplified pulse recorded by the *amplifier cam* (c. f. figure C.2). The beam radius was determined to be $w = (0.77 \pm 0.02)$ mm ($1/e^2$) using a Gaussian fit of a horizontal lineout.

to longer wavelengths. For a pump current of 110 A, a central wavelength of 1038 nm is observed for the amplified pulse. This effect is explained by a change in gain in the resonator, which would require an adjustment of the resonator internal compensation by the two spectral mirrors [53]. Therefore, instead of reducing the diode current, the number of round trips in the cavity was reduced accordingly.

For the operation of the NOPA an amplifier output energy of 1.5 mJ is sufficient. However, for different schemes of probe pulse generation, the CPA system might also be used to generate the necessary pulses for the nonlinear interaction (c. f. section 4.1). Here, as already shown in table 2.1, a higher output energy of the CPA system is desirable. Therefore a maximum of pulse energy is estimated. The most sensible component of the setup is the grating compressor. In fact, the fluence F on the gold gratings (1200 lines/mm [19, p. 80]) should not exceed 0.15 J/cm². For the measured beam radius of the amplified pulse (before the 1:4 magnifying telescope, c. f. figure C.2) and assuming the pulse has expanded due to natural diffraction along the beam line to the diagnostics by a factor of $\sqrt{2}$ ($z_R \approx 1.8$ m), the maximum output energy of the CPA system is

$$E \stackrel{(2.12)}{=} \frac{\pi \tilde{w}^2}{2} F = 11.0 \text{ mJ} \quad \text{with} \quad \tilde{w} = \frac{4w}{\sqrt{2}}. \quad (\text{C.34})$$

This energy output is sufficient for other means of probe pulse generation such as SPM (see section 4.1).

For successful compression of the beam in the compressor, the bandwidth should be in the

range of 13–15 nm. With a time-bandwidth product of a Gaussian beam $\tau\Delta\nu = 0.44$ the theoretical bandwidth-limited pulse length according to equation (2.5) is $\tau = 111$ fs. During an initial operation of the NOPA after relocation of the stretcher to the target area, a low efficiency of the NOPA was noticeable. This was due to a changed number of round trips in the cavity. As the pulse travels through the cavity of the amplifier, it gains GDD in the order of about 1000 fs^2 , which is mainly due to the high-frequency-pass pump mirror, the Pockels cell and the Yb:FP gain medium [82]. Therefore the stretcher alignment is not anymore fitting to the new total GDD of the amplifier and the resulting pulse duration was too long. A measurement was performed with a TOPAC ASF-15 single shot autocorrelator and the results are shown in figure C.4.

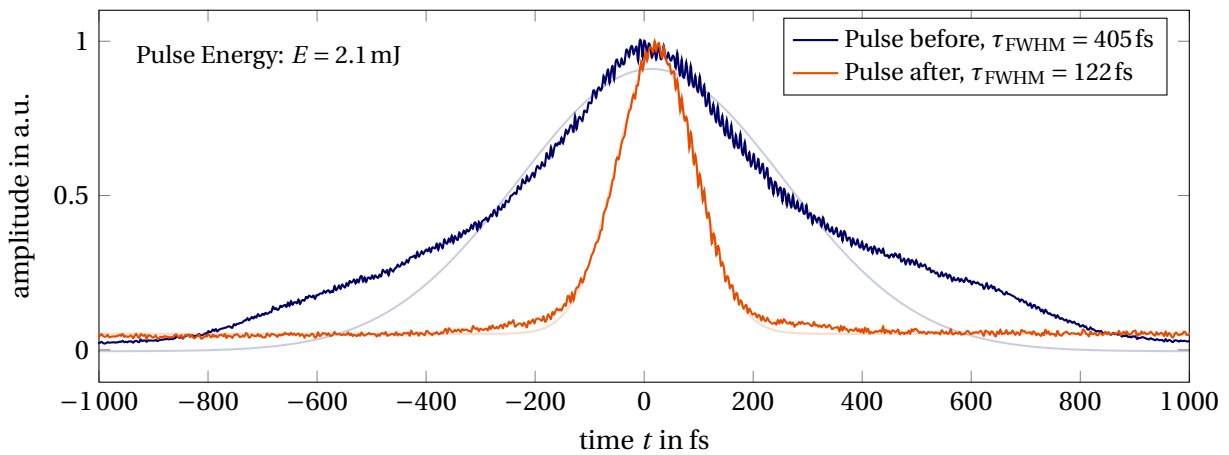


Fig. C.4: Measured pulse length at the compressor output before (blue) and after (orange) the realignment of the stretcher. The autocorrelation function was measured by TOPAG ASF-15 single shot autocorrelator. The desaturated curves show a Gaussian fit to the measured data used to determine the pulse length.

By adjusting the mirror position of the convex mirror in the stretcher (c. f. figure C.1), a minimum pulse duration of $\tau = 122$ fs (FWHM) could be achieved, which is close to the theoretical limit mentioned above.

D. Alignment of the NOPA setup

The most important step to generate a stable, broadband NOPA probe pulse, is the precise spatio-temporal alignment of the SH pump beam and the white-light generated signal beam with the cross angle $\alpha = 2.6^\circ$ into the BBO crystal for parametric amplification. For successful alignment, the position and angle of both beams should be precisely controlled, which can be done using two references and four mirrors. The setup is displayed in figure D.1.

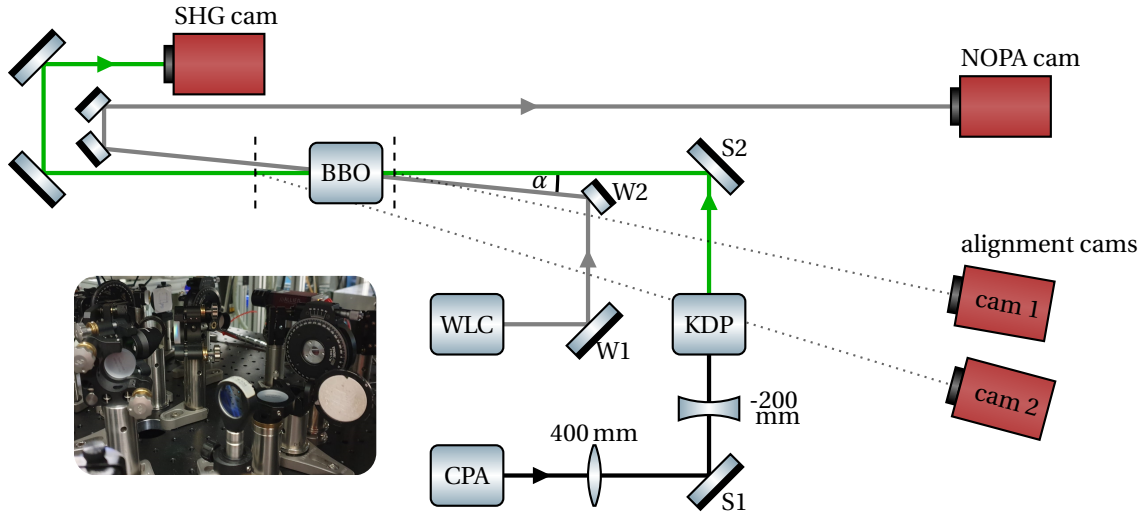


Fig. D.1: Simplified scheme of the NOPA generation in the BBO crystal (c.f. the full scheme in figure 3.1). The alignment onto the first reference is performed using the mirrors S1 and W1 for SH and WLC, respectively. Then the alignment onto the second reference is done with S2 and W2. In an iterative process the precise alignment onto both references can be achieved.

The alignment procedure can now be performed as a four-step process where the first two steps have to be repeated iteratively until both references are aligned:

- 1 Alignment onto the first reference: Make sure the SH is positioned in the middle of the region of interest (ROI) on *cam 1* (white circle in figure D.2) and a neutral density (ND) 4.0 filter is placed on the camera. Then the WLC position can be viewed by blocking the SH and removing the ND filter. Since both beams should overlap inside the BBO crystal, it must be positioned slightly off centered to the left on the first reference as indicated in figure D.2.
- 2 Alignment onto the second reference: This alignment can be done without ND filter placement. The central position of the SH should correspond to the left circle of the reference line (c.f. figure D.3). If the SH signal is strong enough, a bright parametric fluorescence ring is emitted from the NOPA crystal in propagation direction. The parametric fluorescence is a quantum-mechanical effect triggered by zero point fluctuations of the vacuum [83]. The produced fluorescence occurs in directions of the phase-matched wavelengths relative to the SH pump pulse [84]. This forms a cone of phase-matched directions, which can be seen as a ring on the paper. Therefore the

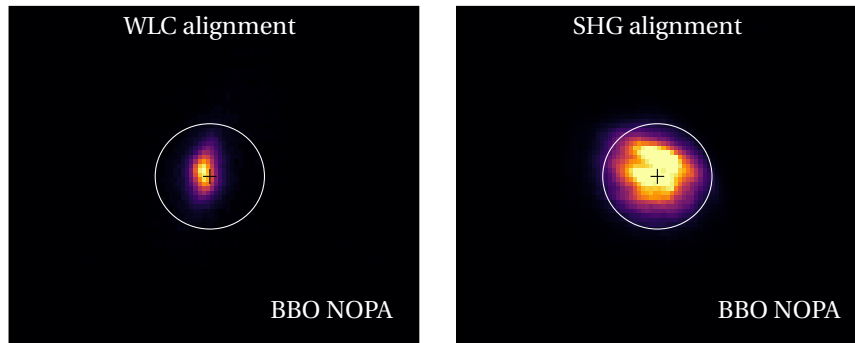


Fig. D.2: Alignment of the WLC (left) and SH (right) on the first reference using *cam 1*. The SH should be aligned to the center of the circular region of interest (ROI), which is centered on the crystal.

parametric fluorescence can be used as an optical guide for the spatio-temporal alignment of the WLC signal and SH pump.

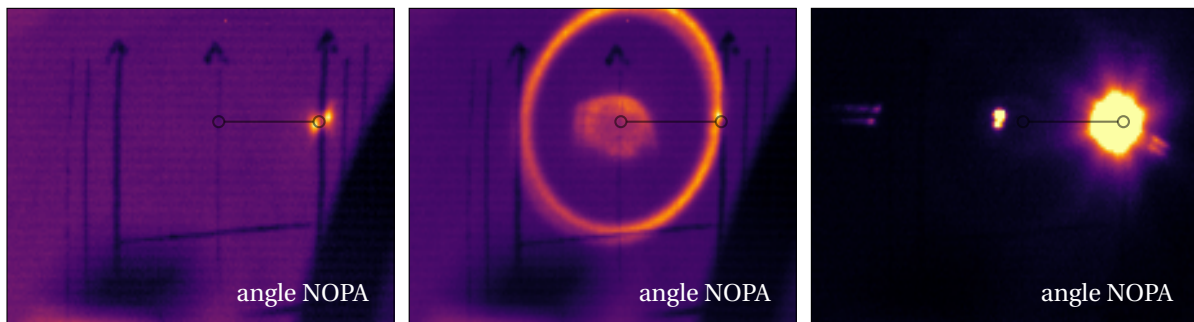


Fig. D.3: Alignment of the WLC (left) and SH (middle) on the second reference using *cam 2*. Both pictures were obtained as a sum of 100 averaged shots in order to enhance the contrast of the pictures. The white-light profile appears to be made of two spots, however, the dark reference line on the paper does not reflect the light very well. The spatial profile of the WLC can be validated using the NOPA cam instead. The right picture shows the amplified white light signal (right), the remaining SH (middle) and the new generated idler (left).

- 3 Verify whether the white light profile beam profile is homogeneous and stable. This can be checked by removing a ND 4.0 filter in front of the *NOPA cam* while the SH is blocked. The shape of the white light can be controlled via adjusting the iris (AI) and the variable neutral density filter (VND) (c. f. figure 3.1).
- 4 Check the temporal overlap of white light and SH. This can be controlled via a motorized delay stage. A single step corresponds to a movement of $10\ \mu\text{m}$ i. e. 33 fs. Then the amplified spectrum can be tuned by varying the SH and white light delay.

E. Spectral sensitivity of the spectrometer

When using a spectrometer to detect light in a large wavelength range, the spectral sensitivity of the detecting charge-coupled device (CCD) array needs to be accounted for. In this thesis, three different spectrometers were used to record the spectra in different wavelength ranges. They are listed in table E.1.

Table E.1: Different spectrometers used in the experiments. They all contain the same chip *Sony ILX511B*.

spectrometer	wavelength	application
Flame-S Ocean Optics	900–1100 nm	SPM spectral broadening
Flame-S Ocean Optics	650–950 nm	NOPA spectrum
USB 2000+ Ocean Optics	900–1100 nm	amplifier spectrum

All spectrometers contain the same 2048-pixel CCD linear sensor *Sony ILX511B* with a pixel size of $14\mu\text{m} \times 200\mu\text{m}$ [85]. In the data sheet provided by the manufacturer, the spectral sensitivity is given in a wavelength range of 400–1000 nm as shown in figure E.1 (left). The spectral calibration function can then be obtained via an exponential fit to the inverse of the spectral sensitivity. The measured spectrum is then corrected by multiplying the exponential curve fit with the experimental data.

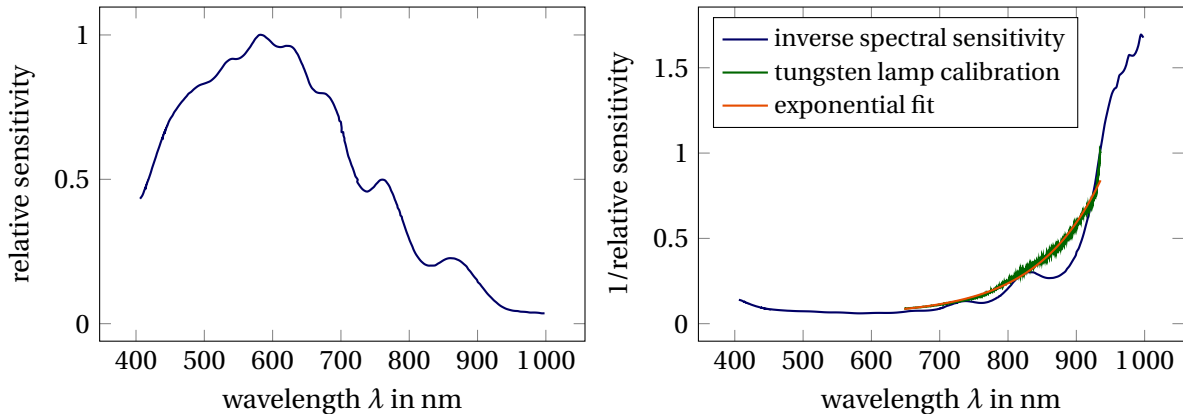


Fig. E.1: Left: Spectral sensitivity of the Sony ILX511B chip measured at $T = 25^\circ\text{C}$ [85]. Bottom: The inverse of the spectral sensitivity (blue) in comparison to a spectral calibration measurement using a Tungsten lamp (green). The measured spectrum was exponentially fitted and subsequently used for correcting the measured spectra.

Since the spectral sensitivity of the chip was only given up to a wavelength of 1000 nm, a separate spectral calibration measurement was conducted in the infrared using a well characterized *M-63350* Quartz Tungsten Halogen lamp manufactured by Newport. As shown in figure E.2, the spectrum follows a Planck curve, which is flat in the spectral region of

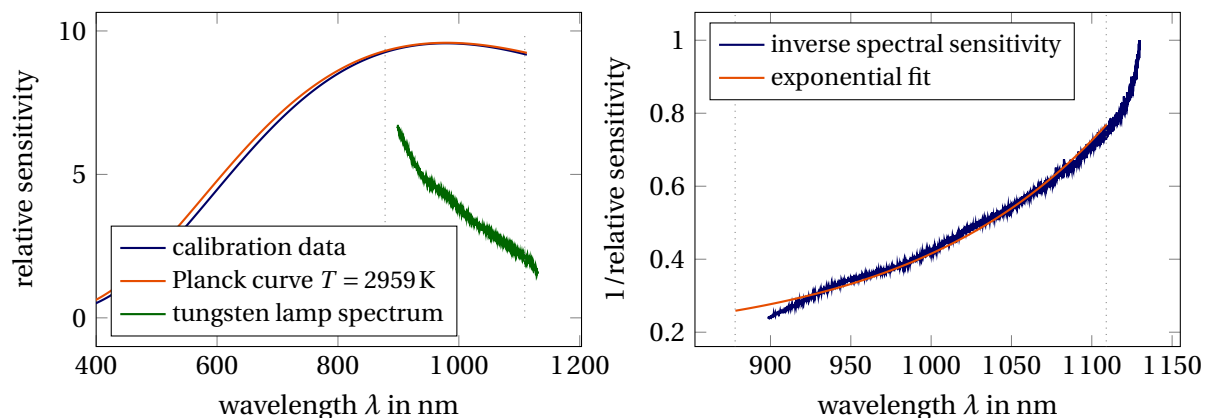


Fig. E.2: Left: Calibration data provided by the manufacturer of the Tungsten lamp. The data corresponds well to a Planck curve for $T = 2959\text{K}$. The wavelength range of the used spectrometer is indicated via gray lines. It can be seen that the emitted spectrum of the lamp is flat in the spectral region of interest. However, the Tungsten lamp spectrum decreases for larger wavelengths.

Bottom: Spectral calibration (blue) obtained via dividing the calibration data by the measured spectrum. The resulting curve was exponentially fitted to obtain a smooth calibration curve.

900–1100 nm. The spectral calibration function can then be obtained by dividing the emission curve of the lamp by the measured spectrum. For a smooth calibration curve, the result was exponentially fitted.

F. Additional experimental data

For the study of the laser-matter interaction of the POLARIS laser with water droplet targets, a shadowgraphy measurement setup, which has been described in figures 3.5 and 3.6, was used to temporally probe the interaction.

A first pump-probe delay measurement was performed on August 26th, 2022 and is shown in figure E.1. Here, *probe 2* cam was used without a coronagraph in place to probe the plasma expansion as a function of delay τ between pump and probe. In this measurement the temporal evolution of the plasma is similar to the measurements on August 30th, 2022. For $\tau > 200$ ps the droplet center starts to become transparent due to the plasma expansion and reduction of electron density.

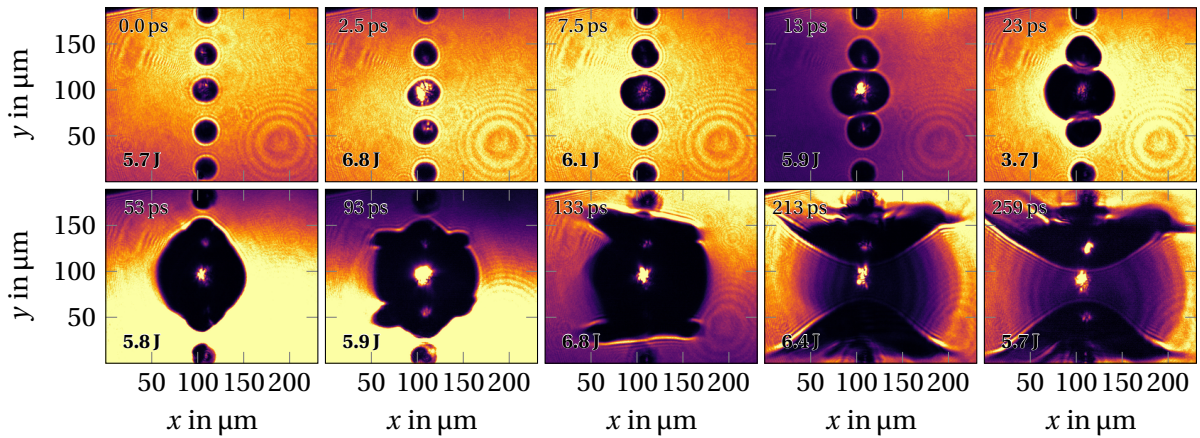


Fig. E.1: Images of the water droplets recorded with camera *probe 2* for different delays between pump and probe pulse. Note that the contrast of the images with shots of lower probe energy was enhanced for better comparison. The pulse energy is indicated in the bottom left corner. The measurements were recorded on August 26th, 2022.

In section 3.4 the delay scan measurements captured by the *probe 2* camera have been already shown in figure 3.11, where the functionality of the coronagraph as a tool of suppressing the plasma emission was successfully tested. As a reference the images were recorded without the coronagraph inserted with *probe 1* camera (a detailed setup description can be found in figure 3.6). For comparison reasons, these images are displayed here in figure E.2. It can be seen that the plasma emission caused pixel errors on the camera for the measurement at $\tau = 2.0$ ps (as already discussed in section 3.4) and at $\tau = 85$ ps. In all other measurements the plasma emission was not strong enough to cause problems in the images. This is mostly due to the moderate energies ranging between 3.2–8 J with a mean value of $E = (6.1 \pm 0.9)$ J (standard variation).

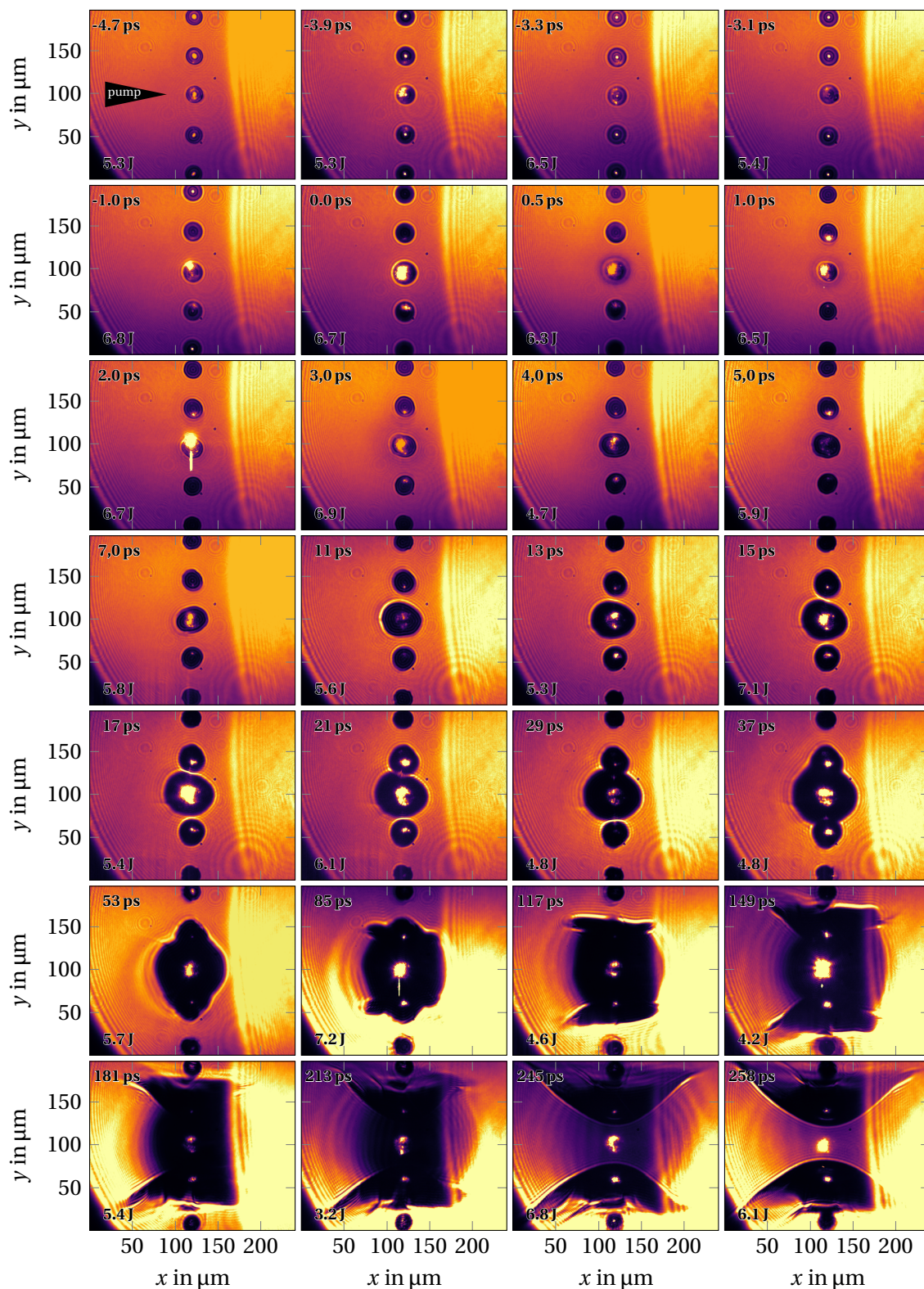


Fig. F2: Images of the water droplets recorded with camera *probe 1* as a reference to the measurements in figure 3.11 for different delays between pump and probe pulse. Note that the contrast of the images with shots of lower probe energy was enhanced for better comparison. The pulse energy is indicated in the bottom left corner. The measurements were recorded on August 30th, 2022.

Selbstständigkeitserklärung und Veröffentlichung

Ich erkläre, die vorliegende Masterarbeit selbstständig verfasst, und keine anderen als die angegebenen Quellen und Hilfsmittel verwendet zu haben. Die Masterarbeit ist bisher weder im In- noch im Ausland in gleicher oder ähnlicher Form als Prüfungsleistung verwendet worden oder als Veröffentlichung erschienen.

Von Seiten des Verfassers bestehen keinerlei Einwände, diese Masterarbeit der Thüringer Universitäts- und Landesbibliothek zur öffentlichen Nutzung zur Verfügung zu stellen.

Jena, Dezember 2022

Martin Beyer